Simulation and Optimization of a Position Sensitive Scintillation Detector with Wavelength Shifting Fibers for Thermal Neutrons

Matthias Herzkamp

Berichte des Forschungszentrums Jülich; 4397
ISSN 0944-2952
Zentralinstitut für Engineering, Elektronik und Analytik (ZEA)
Systeme der Elektronik (ZEA-2)
Jül-4397

D 82 (Diss. RWTH Aachen University, 2016)

Vollständig frei verfügbar über das Publikationsportal des Forschungszentrums Jülich (JuSER)
unter www.fz-juelich.de/zb/openaccess

Forschungszentrum Jülich GmbH
Zentralbibliothek, Verlag
52425 Jülich
Tel.: +49 2461 61-5220
Fax: +49 2461 61-6103
E-Mail: zb-publikation@fz-juelich.de
www.fz-juelich.de/zb

Abstract

Due to the worldwide shortage of ^{3}He and the price development caused by this, alternative concepts of neutron detection are in demand. One possible alternative is a ZnS/LiF scintillation detector with readout via wavelength shifting fibers. The presented dissertation describes the development of a model of the physical frontend, which enables computer-aided simulations with different configurations and conditions.

The model regards the microscopic structure of the scintillator during the tracking of alpha and triton particles created by the conversion of a neutron at a ^{6}Li, as well as the propagation of photons through the scintillator plate. In the first case, the structure is simulated via randomly placed spherical grains, through which the charged secondary particles are tracked. In the second case, the photons are subject to a random walk with parameters dependend on the composition of the scintillator.

The model is validated in several steps, during which single aspects of the model are verified. There is a good agreement between measurements and simulations of neutron absorption and pulse height spectra of different scintillator samples.

A comparison with optical transmission measurements shows, that the simulated effective optical absorption coefficent is of the same order of magnitude as the measured value of samples of one manufacturer, but is smaller by a factor of 6 than the value of samples of another manufacturer.

For the validation of the entire model, measurements of a prototype are compared to simulations. In order to compare the data event-wise, a detection algorithm based on cluster finding is developed. Measurements and simulations are in good agreement, so the model can be regarded as validated.

To optimize multiple parameters at the same time, a generalization of the Golden Section Search can be used. This algorithm optimizes parameters with respect to an optimization function, e.g. detection efficiency, which is calculated dependend on simulation data. This way it is possible to optimize detector parameters for new developments.

Zusammenfassung

Aufgrund des weltweiten Mangels an ^{3}He und der damit verbundenen Preisentwicklung sind alternative Konzepte zur Neutronendetektion sehr gefragt. Eine mögliche Alternative ist ein ZnS/LiF Szintillationsdetektor mit Auslese durch wellenlängenschiebende Fibern. Die vorliegende Dissertation beschreibt die Entwicklung eines Modells des physikalischen Frontends, mithilfe dessen computergestützte Simulationen mit unterschiedlichen Konfigurationen und Bedingungen durchgeführt werden können.

Das Modell berücksichtigt die mikroskopische Struktur des Szintillators sowohl bei der Propagation der Alpha- und Tritonteilchen, die durch die Konversion eines Neutrons an einem ^{6}Li entstehen, als auch bei der Fortbewegung von Photonen innerhalb der Szintillatorplatte. Im ersten Fall erfolgt die Simulation durch zufällig platzierte kugelförmige Körner, durch die sich die geladenen Sekundärteilchen bewegen. Im zweiten Fall sind die Photonen Subjekt eines Random–Walks mit Parametern, die von der Zusammensetzung des Szintillators abhängen.

Die Validierung des Modells erfolgt in mehreren Schritten, in denen jeweils ein Aspekt des Modells überprüft wird. So zeigt sich eine gute Übereinstimmung zwischen Messungen und Simulationen von Neutronenabsorptionsverhalten und Pulshöhenspektren verschiedener Szintillatorproben.

Ein Vergleich mit Transmissionsmessungen optischen Lichts zeigt, dass der simulierte effektive optische Absorptionskoeffizient in derselben Größenordnung wie der gemessene Wert bei Proben eines Herstellers liegt, jedoch um einen Faktor 6 kleiner ist als der Wert von Proben eines anderen Herstellers.

Für die Gesamtvalidierung des Detektormodells werden Messungen eines Prototypen mit Simulationen verglichen. Um einen eventbasierten Vergleich durchführen zu können, wird ein Detektionsalgorithmus basierend auf Clustererkennung entwickelt. Messungen und Simulationen sind in guter Übereinstimmung, weshalb das Modell als validiert angesehen werden kann.

Zur Optimierung von mehreren Parametern kann eine mehrdimensionale Verallgemeinerung des Golden Section Search verwendet werden. Dieser Algorithmus optimiert Parameter in Bezug auf eine Optimierungsfunktion, wie z.B. die Nachweiseffizienz, welche in Abhängigkeit von Simulationsdaten berechnet wird. So ist es möglich mithilfe des Modells Detektorparameter für Neuentwicklungen zu optimieren.

Contents

Chapter 1

Introduction

A huge field in modern day physics is the analysis and characterization of new materials. It is important to determine their structure and modes of excitation in order to explore their potential in certain applications. Current interesting examples are multiferroic materials for efficient and persistent RAM, the magneto-caloric effect for solid-state cooling devices, and the self assembly of nano-particles.

A very common method to gain information about microscopic structures and processes is scattering, where a probe is shot on the sample and the scattering pattern is recorded. Physicists have access to a multitude of probes like x-rays, electrons and neutrons to name the most common ones.

Since neutrons carry no charge, they can interact with surrounding matter only via strong, weak and magnetic interaction. Therefore, they can interact with the magnetic structure of a material and provide information about it. Further, they scatter at nuclei directly and interact with the electrons of the material only due to their magnetic moments. This is an advantage over x-rays and electrons, which are subject to compton scattering and Coulomb interaction. So the latter two probes scatter stronger at atoms with more electrons, and it is very difficult to resolve positions of atoms with low atomic number, like hydrogen.

However, because they have no charge, the detection of neutrons scattered in a sample requires very specific methods. In general, the optimal detection method depends on the neutrons' kinetic energy, as described in Chapter 2.

The kind of detector modelled and simulated in this work is aimed at the detection of thermal neutrons with a kinetic energy of about $0.025\,\mathrm{eV}$. At this energy, neutrons have a de-Broglie wavelength in the order of a few Å and are well suited to resolve lattice distances in scattering experiments.

To detect thermal neutrons, usually ^{3}He gaseous detectors have been employed in the past, because ^{3}He has a large cross section and can be used as neutron converter and counting gas at the same time. Due to its low atomic number it is almost insensitive to gamma radiation, which is a desired property for neutron detection.

However, because demand heavily outweighted supply since about 2005, ^{3}He has become very expensive. The world's main supplier for ^{3}He is the Department of Energy (DOE) of the USA, which obtains it mainly as byproduct of the nuclear weapons production and maintenance. For maximum efficiency, nuclear weapons require a certain amount of tritium, which decays to ^{3}He with a half life of about 12 years and thus must be replaced regularly. So the ^{3}He production capacity of the DOE is determined mainly by the size of the American nuclear weapons arsenal, and not by the demand for ^{3}He.

As of 2010 the annual production capacity of ^{3}He was approximately 8000 L [1], facing a demand of about 65 000 L per year [2], to which the main contribution is the demand for ^{3}He in neutron portal monitors at US borders. Such security sensitive applications are preferred by the DOE, so the amount of ^{3}He on the free market is scarce. This is extremely problematic for detectors which require large amounts of ^{3}He, like for example at the Japan Proton Accelerator Research Complex, where 100 000 L of ^{3}He are needed for planned neutron detectors. Therefore, several alternative developments have been started with the aim to build more cost effective, ^{3}He free neutron detectors. Some of these efforts are described in Chapter 2.

This work aims at the numerical simulation of a ZnS/LiF scintillation neutron detector with Wavelength Shifting Fibers (WLSF), one of the alternatives to ^{3}He detectors. Four detector banks of this type are being installed at the Six Anvil Press for High pressure Radiography and diffraction (SAPHiR) instrument at the Forschungsneutronenquelle Heinz Maier-Leibnitz (FRM-II).

The motivation behind this work is threefold. Beside the solely scientific interest in understanding the interactions inside the scintillator plate, a working, validated model of the detector can be a tool to estimate detection efficiency and spatial resolution for different parameters or even new detector designs, without the need to build a new prototype. Also, using such a model in combination with an optimization algorithm, one can find optimal parameters for the detector depending on different applications. Finally, a working detector system can be supported in the analysis by correcting the counting rate for neutrons of different energies dependening on simulation results. Also, systematical errors may be estimated and the readout analysis can be optimized.

There have been several attempts to simulate ZnS/LiF detectors. However, most of them restricted themselves to the microscopic structure of the scintillator material and only examined how much energy gets deposited in the ZnS grains [3, 4, 5] and not the amount of photons created or detected. One study tries to simulate such a detector system including the WLSFs [6]. However, the model used there ignores the microscopic structure of the scintillator and fiber cladding. This oversight greatly diminishes the usefulness of the results obtained with that model. The existing models are discussed in more detail in Chapter 4.

In this work a full detector model will be developed, which takes into account the microscopic structure and the optical properties of the scintillator and WLSFs. In order to validate the model it will be closely examined and checked by comparison to experimental results.

Chapter 2 gives an overview over different detection methods for thermal neutrons and describes WLSF detectors in detail. The software toolkit Geant [7], which is used to simulate the detector, is introduced in Chapter 3. Chapter 4 outlines the model of the detector and important implementation details of the simulation. The validation of the model is discussed in Chapter 5, where different measurements are compared to simulations. Chapter 6 introduces an optimization algorithm for the parameters of the simulation and shows its application to an example function. Chapter 7 presents important simulation results obtained by different simulations of the model. Finally, a short conclusion and outlook is given in Chapter 8.

Chapter 2

The Detector

Neutrons with more than several hundred keV of kinetic energy can be detected by observing recoil nuclei from collisions between neutron and nucleus. This way it is possible to gain information about direction and energy of the neutron. Since a neutron can impart up to $\frac{4A}{(A+1)^2}$ of its energy, where A is the atomic number of the collision partner, light nuclei like hydrogen or deuterium are best suited for this [8]. If information about the energy is not required, it is often simpler to moderate the neutrons by collisions in a thermal bath in order to lower their kinetic energy. At thermal equilibrium with a 300 K bath, the kinetic energy of neutrons follows a Maxwell distribution with an average of $k_B \cdot 300\,\mathrm{K} = 25\,\mathrm{meV}$.

Such neutrons are called thermal neutrons and they are frequently used in neutron scattering experiments, because their de-Broglie wavelength of the order of 1 Å is well suited to resolve lattice distances in solids. Due to their low kinetic energy, recoil nuclei from elastic scattering processes are hardly detectable. However, there are several isotopes, which are able to capture these slow neutrons and subsequently decay under release of higher energy.

Converter	Reaction product	Released energy	Cross section at 25 meV [b]
^{3}He	^{3}H + ^{1}H	0.764 MeV	5330
^{6}Li	^{4}He + ^{3}H	4.78 MeV	940
^{10}B	^{7}Li + ^{4}He (ground state, 6 %) ^{7}Li* + ^{4}He (excited state, 94 %)	2.792 MeV 2.310 MeV	3840
^{157}Gd	^{158}Gd + (γ or e^{-})	$\sim$ 72 keV	255 000

Table 2.1: Isotopes of helium, lithium, boron and gadolinium as neutron converters, according to [9]

Important examples of capturing isotopes are given in Table 2.1. These examples are interesting for detection purposes, because reaction products include charged nuclei which are imparted with all or part of the reaction's excess energy. Therefore, they are easier to detect by conventional methods like proportional counters or scintillators. In essence, the neutron, which is difficult to detect, is converted into easier detectable particles, which is why these isotopes are called converters.

There is a trade off between the energy released and the cross section of a particular reaction, so a suitable converter must be chosen depending on the application. ^{3}He has been used because of its large cross section of 5330 b for thermal neutrons. The relatively low amount of released energy can still easily be detected in a proportional counter, which contains the ^{3}He.

The neutron capture of ^{157}Gd with a huge cross section of 255 000 b for thermal neutrons does not result in the emission of fast nuclei. Rather, the excited state of ^{158}Gd deexcites via emission of a gamma photon or via internal conversion, where the excess energy is transferred to an electron of an inner shell, which is then emitted from the atom. The low excess energy of 72 keV makes it difficult to detect such a reaction in the presence of background. Further, ^{157}Gd is not very abundant and not easily enrichable due to the small relative mass difference to other gadolinium isotopes. For these reasons gadolinium is not very well suited as a converter in most applications.

The boron reaction shows a smaller cross section than ^{3}He, but it releases much more energy. If the boron is enriched in ^{10}B, BF_3 can be used as counting gas with integrated converter, like the more popular ^{3}He [10]. However, it cannot be operated at pressures as high as ^{3}He, and since the cross section of ^{10}B is lower than that of ^{3}He, BF_3 detectors are always inferiour. Further, the gas is toxic, which makes it dangerous to handle, especially when large quantities are needed.

A safer application is the coating of counting tube cathodes with a boron compound such that either the lithium nucleus or the alpha particle of the boron neutron capture reaction enters the tube and can be detected [11]. However, the coating must be thin so that secondary particles reach the counting gas, which leads to a restricted efficiency. Such detectors are well suited for monitoring purposes. For scientific applications, which require a good efficiency, special stacked arrangements are necessary. It is also possible to use enriched boron in combination with a scintillator, like mixtures of boron oxide and zinc sulfide or boron-loaded plastic or liquid scintillators [9].

Finally, ^{6}Li is the converter which releases the most energy after neutron capture. Since there is no gamma emitted as reaction product, all the excess energy is imparted on the recoil nuclei. This makes it interesting for scintillation detector systems in which very bright scintillation flashes are needed.

A good material for neutron detection is europium doped lithium iodide (LiI:Eu) with the lithium enriched in ^{6}Li. It can be grown as single crystal and has an excellent neutron response. However, it is also sensitive to gamma radiation, such that it is not suited for environments with high background rate. It is further hygroscopic which requires sealed containment in order to prevent the scintillator from dissolving due to moisture. Because of these difficulties, LiI:Eu is not widely used.

Cerium doped ^{6}Li-glass is a widely used scintillator which directly incorporates the neutron converter. It has a very fast response, so it is well suited for applications with high counting rates [12]. However, the light yield is smaller than that of other scintillators and an indistinguishable response to gamma radiation may appear.

The use of lithium fluoride enriched in ^{6}Li as converter in combination with silver doped zinc sulfide as scintillator is the basis for the detector modelled in this work. The constituents are ground to microscopic size and bound in a matrix in order to ensure close proximity. Due to the large amount of energy from the lithium neutron capture and the zinc sulfide's excellent scintillation response to alpha particles, the light yield is very high. For this reason such compounds can be used in combination with cost-effective light detection methods (like WLSF) on large sensitive areas. The long decay time of the scintillator limits the counting rate, but also allows for an efficient gamma discrimination. Due to the opaqueness of the mixture, the thickness of a single scintillator plate is limited to about 500 µm.

2.1 Scintillation

Scintillation is the emission of light which follows ionization by radiation in certain materials. During its passage, an ionizing particle may collide with atoms, molecules or electrons of the material and transfer part of its kinetic energy to them, thus exciting the collision partner. These excitations will deexcite eventually and lose their excess energy in some way. This so-called relaxation process might happen via emission of a photon or by interactions with phonons, i.e. causing lattice vibrations and thus producing heat.

In order to exhibit observable scintillation, a material needs to be transparent to light emitted in this way. Self absorption can be avoided, if the relaxation happens via intermediate steps with low excitation cross sections. One possible intermediate step in a crystal is an exciton, a state in which a conduction electron and a valence hole form a hydrogen-like quasi-particle. Due to their mutual attraction, the energy of a combined state is lower than that of a free electron and a photon created due to recombination of an exciton does not have enough energy to lift an electron from the valence band to the conduction band.

For inorganic crystals intermediate states can be introduced by doping the material with appropriate impurity atoms. ZnS for example has a band width of 3.9 eV [13] and is doped with silver for the use in ZnS/LiF scintillators. The Ag^+ ions replace Zn^{2+} ions and thus have an additional local negative charge. Therefore they are electron donors and can fill vacancies in the valence band of ZnS. With the resulting net positive charge, electrons of the conduction band can be trapped and transferred to an excited state of the silver ion. The subsequent decay into the ground state happens under emission of a 2.7 eV photon, which has too little energy to excite an electron in the valence band. It could be reabsorbed at another silver site, but since they are sparsely distributed throughout the crystal, the probability for that is low.

Conduction electrons and valence holes can reach such recombination centers if they form excitons. In that state they can travel the crystal freely until they are trapped at an impurity and eventually recombine.

2.2 Photon Detection Methods

In the case of scintillation techniques, it is further necessary to convert the optical signals which are emitted by the scintillator into electronic signals for digital processing. This can be done using Photo-Multiplier Tubes (PMT) or Silicon Photo-Multipliers.

Usual photo sensors used in cameras, like CMOS or CCD chips, are very cheap, since they are massively produced. However, these devices collect light in an integrating manner and are read out periodically, meaning that timing information is lost. The information of exactly when an event occurs is essential for some applications like Time of Flight (TOF). Further, it is possible to distinguish between neutron and gamma events depending on the pulse shape if the scintillator has a different response to gammas. Without timing information this is impossible, so camera sensors are unsuitable for many applications in neutron detection.

A PMT operated in pulse mode can give very precise timing information and can even resolve single photons. The sensitivity to single photons is necessary if one uses a WLSF readout. There exist two distinct detector designs for a position sensitive detector using PMTs and a scintillation screen.

The first is the Anger-camera, which is an array of PMTs mounted a certain distance behind the screen. The light flashes of neutron events spread out on their way to the anger camera and are detected in several PMTs at the same time. This allows for reconstruction of the position by taking the mean position of the illuminated PMTs weighted by their signal strengths. This way one can achieve a precision higher than the diameter of each single PMT.

The other design makes use of WLSFs for position reconstruction (see Section 2.3). Only the ends of the fibers have to be monitored, which means that the required PMT surface is proportional to the plate's edge length. In relation to Anger-cameras, which need a PMT surface proportional to the scintillator's surface, this is a cost-effective advantage in case of large scale detectors. However, the use of WLSFs requires a very bright scintillator, because only a small fraction of the scintillation light is carried along the fiber and reaches the PMTs.

2.3 WLSF Detector Type

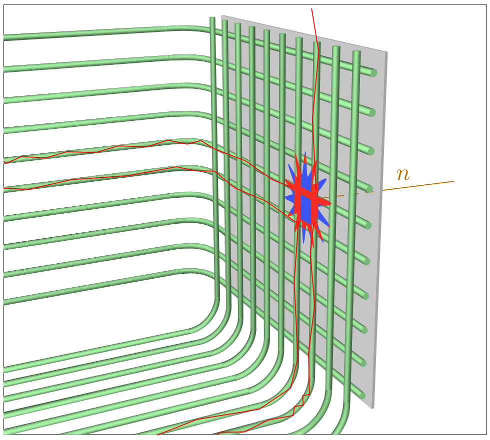

Fig. 2.1: A neutron causes the scintillator plate to emit a bright flash, the photons of which are shifted in wavelength by the WLSFs and carried along to the PMTs, where they are detected.

The detector of interest to this work is a position sensitive ZnS/LiF scintillation detector for thermal neutrons with position reconstruction via WLSFs.

The reaction products of the neutron capture are detected via ZnS, a scintillating material with very high light yield. The light is captured by the WLSFs, which guide a small fraction to PMTs, where they are detected and converted into electrical signals for subsequent digital processing.

The scintillator plate contains LiF and ZnS grains. The LiF is enriched in ^{6}Li, which has a high cross section for capturing thermal neutrons, as mentioned in Table 2.1. If the highly energetic alpha and triton particles created in such an event pass through ZnS, the ionization causes scintillation.

Since the scintillator plate is not homogeneous and the refraction indices of its constituents highly differ (at 450 nm they are 1.4 for LiF [14] and 2.47 for ZnS [15]), the light is scattered heavily before exiting on either side. This limits the practical thickness of the plate, because it gets opaque to its own light.

As depicted in Figure 2.1, there are two orthogonal layers of WLSFs. They absorb light emitted by the scintillator and reemit photons with longer wavelengths isotropically. By total reflection some photons are carried along the fiber to the PMTs.

One can discriminate against thermal noise in the PMTs by performing a coincidence measurement between the two layers. The position of the neutron event can be reconstructed by averaging over all horizontal and vertical fibers separately, and thus obtaining the horizontal and vertical positions respectively (see Section 5.4.1).

2.4 The Scintillator Plate

If a neutron is captured by a ^{6}Li nucleus in one of the LiF grains, the nuclear reaction results in the creation of a triton (^{3}H nucleus) and an alpha (^{4}He nucleus) particle with total kinetic energy of 4.78 MeV. Since there are no other reaction products, no energy is lost to other recoil particles.

As the kinetic energy of the incident neutron (25 meV for thermal neutrons) is insignificant compared to the released energy, the energy imparted on each particle is always the same due to conservation of momentum (i.e. $\vec{p}_\alpha = -\vec{p}_t$)

$$\frac{E_\alpha}{E_t} = \frac{m_t p_\alpha^2}{m_\alpha p_t^2} = \frac{m_t}{m_\alpha} \tag{2.4.1}$$

With the sum being $E_\alpha + E_t = 4.78\,\mathrm{MeV}$ and the mass ratio between the particles being 4:3, the energy divides as

$$\begin{aligned} E_\alpha &= 2.05\,\mathrm{MeV} \\ E_t &= 2.73\,\mathrm{MeV} \end{aligned} \tag{2.4.2}$$

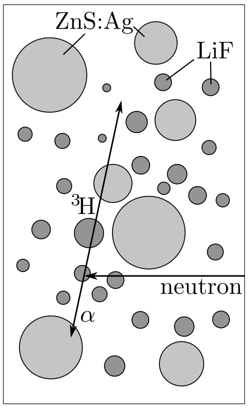

Fig. 2.2: Schematics of a neutron hitting a LiF grain in the scintillator and causing the emission of a triton and an alpha particle.

As charged particles, the triton and alpha lose their kinetic energy mostly due to ionization of the surrounding material, which causes the scintillator ZnS:Ag to scintillate. In order to increase the brightness of the scintillation flashes, a large amount of ZnS in the scintillator is advantageous. However, this leads to a smaller amount of ^{6}Li nuclei, and thus to a lower neutron conversion efficiency. A compromise must be found depending on the actual application.

With energies as in (2.4.2), the triton has a range of about 30 µm in ZnS and LiF, and the alpha has a range of about 5 µm [16]. This means, that in order for the particles to be able to leave their origin LiF grain and enter a ZnS grain to create scintillation light, the grain sizes of LiF grains must be sufficiently small.

The scintillation light is emitted isotropically in all directions. Since the plate does not consist of a homogeneous material, but rather a matrix of microscopic grains with highly different refraction indices ($n_{\text{LiF}} = 1.4$ at 450 nm [14] and $n_{\text{ZnS}} = 2.47$ at 450 nm [15]), light is heavily scattered inside it, which gives rise to the scintillator's opaqueness. Furthermore, ZnS is not transparent to its own scintillation light, and thus may reabsorb some scintillation photons traversing ZnS grains. These effects limit the possible maximum thickness of the plate to about 500 µm.

2.5 Wavelength Shifting Fibers

Using a WLSF readout enables the construction of large area detectors at affordable costs. A large area is needed for neutron diffraction measurements of samples with sizes of several cm, because then the detector must be positioned at a certain distance to minimize parallactical effects. In order to cover a large solid angle at such distances, several m^2 of sensitive detection area are required.

A WLSF is a conventional optical fiber containing flourescent dye. The dye particles absorb photons with short wavelengths and reemit photons with longer wavelengths isotropically. A certain fraction of reemitted light is guided along the fiber via total reflection at the boundary.

If such a fiber is placed along the scintillator, it will carry a light pulse whenever a neutron event happens near it anywhere along its length. The brightness of this pulse will be proportional to the amount of scintillation light passing through the fiber. This amount in turn depends on the distance between fiber and the event's position and of the event's brightness itself. Also, obstruction of adjacent fibers can attenuate the light flash. Overall, the fibers closest to the event are likely to carry the most photons, such that the position of the event can be deduced from the distribution of photons over the fibers.

2.5.1 Internal Reflection and Fiber Cladding

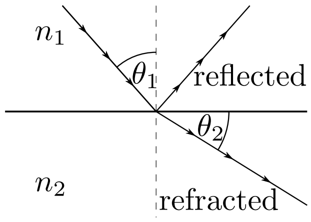

Fig. 2.3: A light ray is reflected/refracted at a medium boundary

The angle of total reflection at the boundary of the fiber depends on the refractive indices of the bordering materials and is determined by Snell's law $n_1 \sin(\theta_1) = n_2 \sin(\theta_2)$ (see Figure 2.3). If the sine of θ_1 exceeds n_2/n_1, there is no valid value for θ_2 and refraction is forbidden. This means, that all light is reflected internally. So we have

$$\theta_{\text{total}} = \arcsin\left(\frac{n_2}{n_1}\right) \tag{2.5.1}$$

for the minimum inbound angle in order to get total reflection. So, a photon, which is emitted from the center of a cylinder, must have an angle of less than $90° - \theta_{\text{total}}$ with the cylinder's center axis to be reflected totally and thus be guided along the cylinder (see Figure 2.4). The integral of all angles which lead to total reflection is then

$$\Omega = \int_0^{2\pi} d\phi \int_0^{\frac{\pi}{2}-\theta_{\text{total}}} d\vartheta \, \sin(\vartheta) = 2\pi \left(1 - \cos\left(\frac{\pi}{2} - \theta_{\text{total}}\right)\right) = 2\pi \left(1 - \frac{n_2}{n_1}\right) \tag{2.5.2}$$

This is the solid angle for light guided in only one direction. If we take into account the opposite direction as well, the fraction of the whole solid angle becomes $\left(1 - \frac{n_2}{n_1}\right)$. This is the approximate value for the fraction of light trapped within the fiber in the wavelength shifting process. The actual value is higher, because if a photon is emitted from an excentric position, there are additional directions, which give rise to helical movement through the fiber. Calculating the exact fraction is cumbersome and does not yield an analytical result. Since it is not of great importance, it is not discussed here.

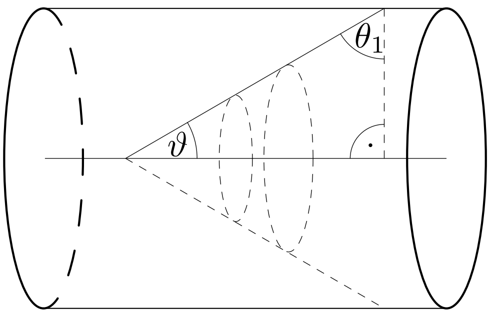

Fig. 2.4: Opening angle of the light cone, which is guided along the fiber

In our case, the fiber is made out of Polystyrene (PS), with a refractive index of $n_1 = 1.59$. At a boundary with air ($n_2 \approx 1$), this would yield a total reflection angle of 42° and a trapping fraction of about 33 %. However, the boundary with air almost certainly does not exist all the way to the PMT, where the photons need to arrive. The fiber will be mounted somehow and therefore needs to be in contact with a mechanical structure. At these contact points, much light previously trapped in the fiber might be absorbed, refracted or otherwise scattered. Another source of light loss can be impairments of the surface polish, may they be of permanent nature like fissures or scratches, or only temporary like smudges of oil or dust.

Due to these unknown losses the fiber would not be well defined, which would make a comparison between the light gain from different fibers impossible, and thus lower the spatial resolution. To counter this, one usually uses so-called cladded fibers. These are fibers with a PS core and an additional outer layer with a lower refractive index. The inner optical boundary is protected by the cladding and its existence is ensured along the whole length of the fiber.

The manufacturer Kuraray offers two types of cladding: single cladding and multi cladding [17]. A single cladded fiber consists of a PS core and a cladding out of Polymethylmethacrylate (PMMA). The multi cladding also consists of these two layers, with an additional cladding out of Fluorinated polymer (FP), as shown in Figure 2.5. The thickness of each cladding layer constitutes 3 % of the total fiber thickness.

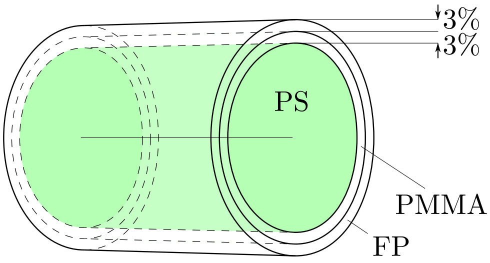

Fig. 2.5: Sketch of the fiber multi-cladding geometry. Only the innermost PS-layer contains dye particles. A fiber with single cladding simply lacks the outermost layer.

From the optical point of view it is unecessary to insert the PMMA layer between PS and FP, because this intermediate layer does not influence the angle of total reflection. To see this, let's call the refractive indices of PS $n_1 = 1.59$, of PMMA $n_2 = 1.49$ and of FP $n_3 = 1.42$. The total reflection angle between PMMA and FP is $\theta_{2\to3} = \arcsin\left(\frac{n_3}{n_2}\right)$. In order to hit at this angle, a beam of light must be refracted at the PS/PMMA boundary according to Snell's Law: $n_1 \sin(\theta_{1\to2}) = n_2 \sin(\theta_{2\to3}) = n_3$. This gives

$$\theta_{1\to2} = \arcsin\left(\frac{n_3}{n_1}\right), \tag{2.5.3}$$

which is independent of n_2. So, the reason to include the intermediate layer may be ease of manufacture, adhesion problems or even bending properties.

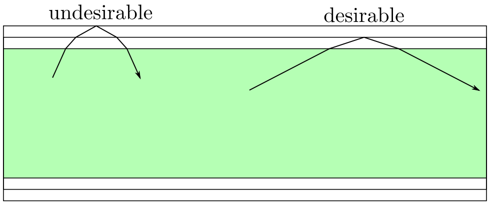

Fig. 2.6: Photons which are reflected at the boundary between outermost cladding and air are subject to uncontrollable imperfections at that boundary. They are not guaranteed to reach the PMT and are thus undesirable.

Equation (2.5.3) reveals another problem: if the cladded fiber is placed in air, the angle of total reflection is determined at the unprotected boundary between air and outermost cladding, as shown in Figure 2.6. To eliminate photons, which are trapped at the air boundary, one can add an absorbing agent in the outermost cladding layer [18]. The absorbance of the outermost layer should not be very large, because it would otherwise absorb too much of the incident scintillation light. On the other hand, the attenuation must be strong enough to absorb most of the undesired photons before they reach the PMT. For a more detailed consideration, see Section A.1. This way the fiber is guaranteed to be well defined under any circumstances.

2.6 Development for SAPHiR

SAPHiR is an instrument under construction at the FRM-II. With the six independently adjustable anvils it will be able to create environments of up to 15 GPa pressure for samples of up to 20 mm^3 volume. The instrument can be operated in radiography mode, where the neutron beam is continuous, or in TOF diffraction mode, where a chopper divides the beam into short packages, which disperve according to differing neutron velocities. In TOF mode the neutron wavelength ranges from 1 Å to 2.4 Å.

The anvils compressing the sample volume cover much of the solid angle and absorb neutrons scattered towards them. Thus, only neutrons scattered forward, backward or perpendicular to the neutron beam can be observed, as indicated in Figure 2.7. The forward and perpendicular directions will be occupied by ^{3}He proportional counters.

Backscattered neutrons will be detected by four WLSF detector banks developed at the Zentralinstitut für Engineering, Elektronik und Analytik (ZEA-2) in Jülich. The detector requirements are $2.5 \times 2.5\,\mathrm{mm}^2$ spatial resolution, better than 1 µs time resolution and counting rates of a few 10 kHz. The detection efficiency is required to be larger than 50 % for 1 Å neutrons.

To meet the requirement of efficiency, the detector consists of two 500 µm scintillation screens from the manufacturer ELJEN Technology (ELJ) with a 2:1:1 ZnS:Ag/LiF/Binder mass ratio. The two WLSF layers run between the scintillator plates and both ends are bent towards the back, where they are read out by 8 × 8 Hamamatsu Multi Anode Photo Multiplier Tubes (MaPMT). "Multi Anode" means that there is one square shaped photo

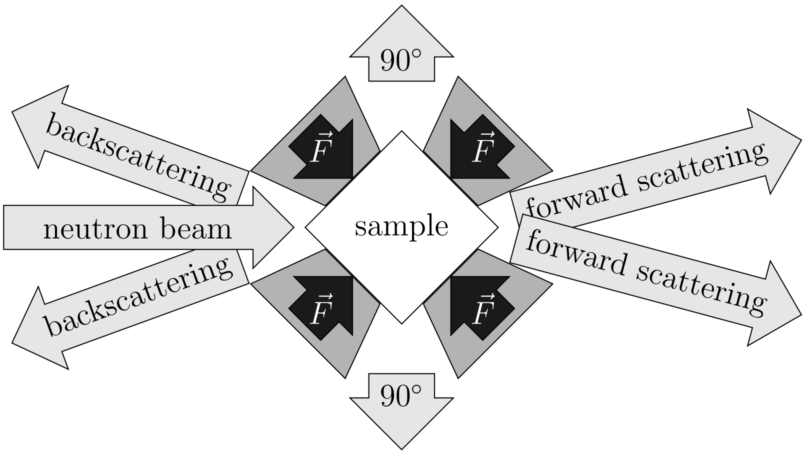

Figure 2.7: Schematic of possible detection directions at the SAPHiR instrument with the sample in the center, four anvils on each side and the neutron beam incoming from the left. The top and bottom anvils are not shown. The anvils exerting pressure on the sample cover much of the solid angle. Thus, only neutrons scattered forward, backward or perpendicular can be examined.

cathode for multiple anodes and their respective dynode chains positioned in an 8×8 grid behind it.

The fibers have a thickness of 1 mm and are placed with 1 mm gaps in between them. In one direction there are 128 fibers read out by two MaPMTs, in the other direction there are 192 fibers for three MaPMTs, which determines the sensitive detector area of one detector bank to be $256 \times 384\,\mathrm{mm}^2$. As shown in Figure 2.8, both ends of each fiber are read out by the same MaPMT pixel in order to increase the light output per neutron event and thus the detection efficiency.

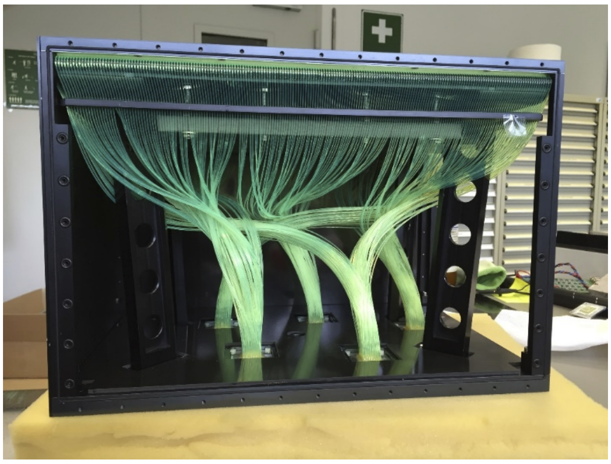

Fig. 2.8: Fiber guidance in the detector. On the top there is the orthogonal WLSF array sandwiched by scintillator screens (not visible). The fibers are bent backwards and merged into five bundles, and a MaPMT is mounted behind each bundle. Note that opposite ends of each fiber are fed into the same MaPMT pixel.

Each MaPMT is controlled and read out by its own board, which contains a Multi-Anode ReadOut Chip (MAROC) for adjusting amplifier gains for different channels independently and for discriminating the resulting signals. The individual adjustment of gains is necessary because of non-uniformities across pixels of the MaPMT. The trigger data of the MAROC is collected on a concentrator board, which is connected to all five modules and checks the data for coincidence between layers. The concentrator board is also responsible for the synchronization between the modules, which add a time stamp of 2 ns resolution to each photon event.

The four detector banks have already been delivered to the University of Bayreuth and are ready for installation at SAPHiR. The ZEA-2 is now working on improving the event reconstruction algorithm as well as an automatic system for adjusting the channel gains of the MaPMTs.

When the detector banks will be in use, the concentrator board will perform the analysis of photon events and send information about position and time of any neutron events to the lab computer. In contrast to this, all photon data including channel number and timestamp was stored for offline analysis during the measurement described in Section 5.4.

Chapter 3

Simulation Toolkit Geant4

Geant is an acronym for "Geometry and Tracking" and names a software library for the simulation of particles in matter, developed and maintained by CERN [7]. It is able to simulate a wide variety of particles, including leptons, hadrons, neutrinos, photons and atomic nuclei. In a Geant simulation such particles are tracked in their surrounding matter in discrete steps, during which physical processes influence the state of the particles.

Particles which are tracked by Geant do not interact with each other, but only with the surrounding material. This means that two particle tracks are independent of each other and can be calculated in arbitrary order. Therefore, Geant cannot fully simulate whole experiments, but it is perfectly capable to simulate detectors.

In the simplest case, the user defines the geometry and material properties of the setup, specifies which physical processes are to be taken into account in the simulation, and chooses the initial particles. The initial particles are then tracked by the program until they decay or lose enough kinetic energy to fall below a threshold. At every step it is possible for processes to create secondary particles. However, these secondaries will only be tracked, if their kinetic energy is above the threshold.

It is possible to declare some parts of the detector to be sensitive detectors in order to obtain results from the simulation. They will be informed of any changes a particle undergoes inside them, and are thus able to e.g. count the amount of energy deposited in them.

3.1 Geant API

The version of Geant used in this thesis (Geant4) is written in C++, making use of modern object oriented programming design. To run a Geant simulation, it is necessary to implement derivatives of the purely virtual interface classes `G4VUserDetectorConstruction`, `G4VUserPhysicsList` and `G4VUserPrimaryGeneratorAction`, in which the detector definition, the set of applicable physical processes, and the initial particles must be defined respectively.

While implementing these three classes is mandatory, there are many purely virtual classes, which offer rich interfaces to the simulation. Implementing and deploying these enables access to and manipulation of nearly any aspect of the simulation, which makes Geant a very flexible and versatile tool.

3.2 Stepping and Processes

A Geant4 program is a finite-state machine, which tracks the trajectories of particles in discrete steps and applies physical processes to them depending on the particle's type, charge and energy, as well as the surrounding material's properties.

The central part of the tracking process is the `G4SteppingManager`, which processes each discrete step of each trajectory. At the beginning of each step, it queries all active physical processes, which are applicable to the particle, to propose a step distance. The `G4SteppingManager` will then choose the shortest step distance proposed and in turn inform the processes about it.

A default implementation of the stepping distance calculation, which is used by a multitude of predefined physical processes in Geant, can be found in the `G4VDiscreteProcess` class. It begins with drawing a positive, real exponentially distributed random number ξ with expectation value one. ξ is stored in the `currentInteractionLength` field of the super class `G4VProcess`.

During every step taken by a particle, to which a process is applicable, the process will propose a step distance which is the product of its `currentInteractionLength` and its mean free pathlength obtained by a call to the function `GetMeanFreePath()`. After each step the quotient of actual step length and current mean free path is subtracted from the `currentInteractionLength`. This number is used in the next iteration, instead of drawing a new random number. This approach omits many costly drawings of random numbers, and still handles a non-constant mean free path length correctly. This means, that user processes only have to implement the `GetMeanFreePath()` method and the actual effect of the process, if they extend this class.

There are three distinct process callbacks for three different situations and purposes. `AtRestDoIt()` is called at the beginning of stepping if the kinetic energy of the particle is below a threshold. The particle is then numerically treated as stopped and processes like radioactive decay may delay the particle's termination. `AlongStepDoIt()` is used to apply a "continuous" effect on the particle. For example, the influence of an electromagnetic field on a charged particle is such a continuous process and needs to be applied all along the trajectory. The `PostStepDoIt()` method is to be used for event-like effects. At each step only the `PostStepDoIt()` method of the process, which proposed the smallest step length, is called. Thus, the `PostStepDoIt()` method is called for every process once the `currentInteractionLength` of that process reaches zero.

The communication between stepping manager and different processes is conducted via a `protected` field `aParticleChange` defined in the interface `G4VProcess`. During the `*DoIt()` methods, processes may store any changes to the particle in this object. There is the possibility to change position, momentum, polarization etc. Processes may also initialize the creation of new daughter particles, so called secondaries, via this method.

3.3 Scintillation Process

Scintillation is already part of the Geant4 toolkit, and is implemented in `G4Scintillation`, a subclass of `G4VRestDiscreteProcess`. This means that it implements the methods `AtRestDoIt()` and `PostStepDoIt()` and respectively `GetMeanLifeTime()` and `GetMeanFreePath()`. Both methods are implemented equally: they check whether the surrounding material is an active scintillator and, if that is the case, check how much energy has been deposited in the material during the current step. Then a number of photons proportional to the deposited energy is created, with random directions and polarizations. The wavelength of a scintillation photon is also determined randomly, according to a distribution defined in the material properties of the surrounding material. The proportionality constant between deposited energy and number of photons has to be specified by the user and is not subject to any checks of conservation of energy. That means the user is responsible for checking the values for sanity.

In order to be a scintillator, an object's material must have several properties set. It is possible to define two scintillation components with different decay times and energy spectra. The decay times of the components are defined by the material properties `FASTTIMECONSTANT` and `SLOWTIMECONSTANT`. The fraction of how many photons are created in the fast or slow mode is given in `YIELDRATIO`. `FASTCOMPONENT` and `SLOWCOMPONENT` are lists of energy-value pairs and describe the emission spectrum of the scintillation light. The use of two different components enables the simulation of different pulse shapes for different ionizing particles. This is of main interest in the case of pulse shape discrimination when discriminating against e.g. gamma particles.

`SCINTILLATIONYIELD` is the amount of photons created per energy. After each step a number of photons is created equal to the product of this number and the amount of energy deposited in the material. There is also the possibility to set a multiplicative factor for the scintillation yield via `SetScintillationYieldFactor()`, a method of `G4Scintillation`. The created photons have random direction and random polarization, and an energy distributed according to `FASTCOMPONENT` or `SLOWCOMPONENT`, depending on the mode in which the photon was created.

3.4 Wavelength Shifting Process

Geant4 includes a process for wavelength shifting in the class `G4OpWLS`. It is a subclass of `G4VDiscreteProcess` which implements the functions `GetMeanFreePath()` and `PostStepDoIt()`. Since only optical photons should be absorbed by WLS materials, this process only applies to particle objects of the `G4OpticalPhoton` class.

The mean free path depends on the photon's energy and must be defined for every wavelength shifting material in the material property `WLSABSLENGTH`. This property must be defined as a list of energy-value pairs, where the values in this case are the absorption lengths of photons of the given energy.

`PostStepDoIt()` stops and kills the optical photon for which it gets activated and creates a secondary optical photon at the last position. The wavelength of the new photon is determined randomly according to the distribution provided in the material property `WLSCOMPONENT`. Direction and polarization are completely random. The new photon starts at a random time after its absorbtion, distributed exponentially with mean defined in the material property `WLSTIMECONSTANT`.

If the material property `WLSMEANNUMBERPHOTONS` is defined, the WLS-process creates not one emitted photon per absorbed photon, but a random poisson-distributed amount. Without this parameter exactly one shifted photon will be created, which is needed in our case. It is noteworthy that like the scintillation process, this process does not check conservation of energy, i.e. it is possible for the created photons to have more energy than the original absorbed one.

Chapter 4

Description of the Model

The first computer aided simulation of a ZnS/LiF detector was reported in 1975 [3]. The model used in this simulation consists of a slab geometry, with 10 µm ZnS:Ag slabs alternating with LiF slabs of a thickness dependend on the mass ratio. A neutron event is simulated as triton and alpha particles starting in a random position inside a LiF slab in a random opposite directions. The amount of energy deposited in ZnS:Ag is approximated by the inersection of the particle's paths with ZnS:Ag slabs. The range of the particles needs to be determined experimentally and is used as path length.

This crude aproximation ignores the influence of the binder material as well as the LiF grain size. Further, the deposition of energy along a charged particle's path through matter is not constant. Since the cross section of such a particle increases with decreasing velocity, most of its energy is deposited at the path's end. The simplicity of the approach can probably be ascribed to the available computer hardware at that time.

There have been two further attempts to improve this model in recent years. Stephan *et al.* used randomly placed spheres of ZnS:Ag inside a ^{6}Li loaded glass binder as a model for the scintillator material [4]. Parameters in their simulations include the radius of the spheres and the volume fraction of ZnS:Ag. It is unclear whether overlap between different spheres is allowed in their model. An alpha/triton pair is allowed to start anywhere in the surrounding ^{6}Li-loaded material and is tracked using a modification of the heavy charged particle transport code SRIM.

Sadly, the data given in [4] is contradictory. In the sub-micrometer limit of grain sizes, the average energy deposited in the ZnS grains should be proportional to the volume fraction of ZnS. For several volume fractions an average deposited energy twice as large as the correct value was reported. This limits the comparability with their data.

Yehuda's approach was to simulate the propagation of alpha and triton within ZnS:Ag spheres ordered in a regular fcc lattice [5]. Ordering the grains in a fixed pattern is a computationally inexpensive method of placing the grains. However, it is a contrast to the random distribution in real scintillator materials. This leads to an incorrect distribution of empty space between the grains and can distort the results.

Both approaches track the energy deposited in ZnS:Ag through ionization processes, which is a good improvement with respect to the path intersection model. However, some questions still cannot be answered. Both models do not regard the size of LiF grains, in which alpha and triton particles are created. Due to the finite length, a certain amount of energy is always deposited in the LiF, an effect which should not be disregarded since typical LiF grain sizes are of the order of the alpha particle's range in the scintillator. Further, both models use spheres of identical sizes. Thus, the influence of different variances of radii distributions cannot be examined.

An attempt at simulating a ZnS/LiF detector with WLSF readout has been reported in [6]. There the scintillator is modelled as a homogeneous structure, where the entire energy of the neutron capture process gets deposited. No attempt at simulating the microscopic structure is made. The model uses a light yield of 160 000 photons per neutron given in [19], which is the value for an optimized configuration and not readily generalizable to any ZnS/LiF scintillator.

The WLSFs are modelled as simple cylinders without cladding. Therefore, the trapping efficiency depends on the refractive index of the surrounding material. This is generally an undesired behaviour as discussed in Section 2.5.1. These oversights diminish the usefulness of the results.

In this work, the physical front end of the detector described in Chapter 2 is modelled including the microscopic structure for alpha and triton propagation, the creation and propagation of photons inside scintillator plate and WLSFs, and photon detection in PMTs. As such, it is currently the most complete model of a ZnS/LiF scintillation detector with WLSFs to the author's best knowledge.

The model was implemented using Geant4 (see Chapter 3). To be able to easily adapt the model to future needs each component is defined in its own module. The different modules are a grain box, the scintillator plate, the WLSF layers, and a photon counter. Each module can be activated or deactivated during runtime and will then be added to or removed from the simulation.

Many parameters of the simulation are freely adjustable. Names and default values of these adjustable parameters used by the different modules are shown in tables 4.1, 4.2, 4.3 and 4.5. In every simulation described in this work the default values have been kept, if not otherwise stated. Figure 4.1 shows the simulation of one neutron event in the final model. Visible in this image are the scintillator plate, WLSF array and paths of scintillation (blue) and wavelength shifted (green-brown) photons.

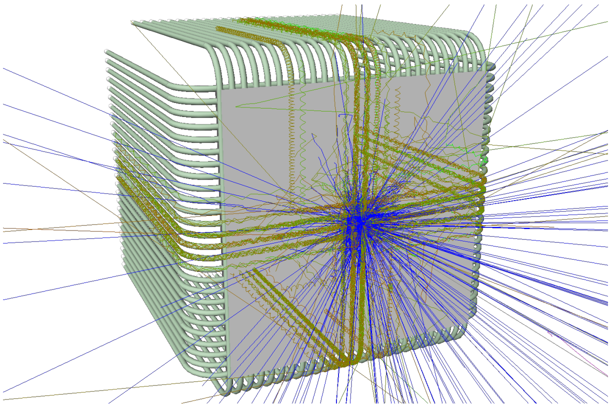

Fig. 4.1: One event simulated in Geant with our model. The blue lines correspond to scintillation photons, the green-brown lines are wavelength shifted photons guided by the WLSFs. In order for the picture to show something discernible, the scintillation yield factor has been set to 0.05

The modelling of the microscopic structure of the scintillator plate constitutes a central part of this thesis. Since the plate consists of two types of grains bound together in a matrix, with grain sizes being in the order of 10 µm, and the scintillator plate having a volume in the order of 10 cm^3, a full description of the scintillator plate with grains is impractical. It would require about 10^9 geometric entities with randomized parameters and positions, which exceeds the computational power of a standard desktop machine.

Fortunately the microscopic structure does not influence all aspects of the simulation. Since neutron capture is a singular event, structure correlations on the microscopic scale are unimportant for this process. Thus, the scintillator can be treated as a homogeneous material with a certain ^{6}Li density for the purpose of neutron propagation.

However, the question of how much energy is deposited in the scintillating material ZnS:Ag cannot be answered accurately without taking the microscopic structure into account, because alpha and triton particle deposit energy during many collisions in the surrounding matter. The alpha particle's range in the scintillator is about 5 µm [16], which is of the same order of magnitude as the grain sizes. Therefore, in order to study the energy deposition in ZnS:Ag, the propagation of alpha and triton through the grain structure is simulated by the grain box module described in Section 4.1.

As described in 2.4, the propagation of photons in the scintillator is also influenced by the microscopic structure. The light is heavily scattered while propagating through the material and the amount of scattering depends on microscopic parameters. Section 4.2 describes two different models for propagation of photons inside the scintillator plate.

variable name	symbol	default value	description
`/var/global/partLiF`	ϕ_{LiF}	1	Mass fraction of LiF
`/var/global/partZnS`	ϕ_{ZnS}	2	Mass fraction of ZnS:Ag
`/var/global/partBinder`	ϕ_{binder}	1	Mass fraction of binder material
`/var/global/grainSizeLiF`	s_{LiF}	2.5 µm	Grain size of LiF grain at origin
`/var/global/grainSizeZnS`	s_{ZnS}	7.5 µm	Grain size of ZnS grains
`/var/global/sizeDeviationLiF`	σ^*_{LiF}	0.4	Relative deviation of LiF grain size
`/var/global/sizeDeviationZnS`	σ^*_{ZnS}	0.4	Relative deviation of ZnS grain size
`/var/global/binderDensity`	ρ_{binder}	$1\,\mathrm{g\,cm^{-3}}$	Density of the binder material
`/var/grainbox/grainBoxLength`	l_{box}	100 µm	Length of the module volume
`/var/grainbox/grainBoxWidth`	w_{box}	40 µm	Width of the module volume

Table 4.1: Parameters used by the grain module with their respective default values.

4.1 Grain Box for Alpha and Triton Particle

The grain box module simulates the propagation of alpha and triton particle within the microscopic structure of the scintillator in order to determine the amount of energy deposited in ZnS grains. At the beginning of each event the grainbox is populated randomly with microscopic grains as shown in Figure 4.2. Also, an alpha and a triton particle with opposite directions of momenta and kinetic energies as in (2.4.2) are created at the center of the box. In order not to influence any other part of the simulation, the grain box is placed outside of the scintillator plate and influences the rest of the simulation only by adjusting the scintillation yield of `G4Scintillation`. Alpha and triton particles are created during every event, regardless of whether the neutron is captured or not. In fact, they are always tracked before the neutron, so that the scintillation yield is already determined when the neutron is captured. This means that the module can be used as a stand-alone model for examining the energy deposition in ZnS grains.

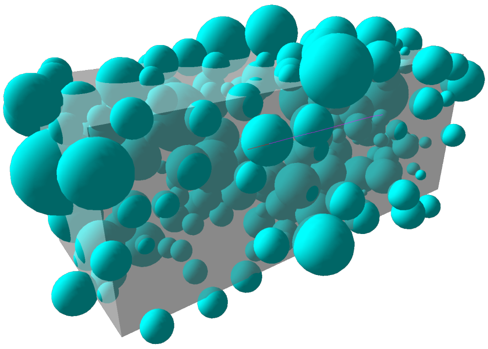

Fig. 4.2: Exemplified placement of ZnS spheres in the grain box module. The radii and placements of spheres are random, but without overlap. The dimensions of this box are $40 \times 40 \times 100\,\mu\mathrm{m}^3$.

The grains are modelled as spheres of varying radii, scattered throughout the box. Although real grains are unlikely to be exactly spherical, they usually attain shapes similar to convex polyhedra during the grinding process, as electron microscopic images show. So, spheres are a good first order approximation.

Initial tests revealed that including placement of LiF grains explicitly in the simulation is very costly with respect to memory requirements and simulation time. This is due to their much smaller grain size (commonly about 2 µm to 3 µm) so that there are an order of magnitude more LiF grains than ZnS grains. Since the distinction between energy deposited in LiF grains and energy deposited in the binder material is unimportant to the simulation, it is possible to incorporate lithium and fluor in the binder. However, care must be taken that the alpha and triton particles do not start inside a ZnS grain. To ensure this, there is a region placed such that it contains the origin, with a radius corresponding to the LiF grain size, and in which no ZnS grain can be placed.

In each event in which the grain box module is enabled, the alpha and the triton particles are tracked first. This way the energy deposited in ZnS grains can be determined before the neutron is captured and deposits 4.78 MeV in the scintillator plate. The yield factor of `G4Scintillation` is changed via `SetScintillationYieldFactor()` to the amount of deposited energy divided by 4.78 MeV. There are no photons created directly in the ZnS grains of this module, because the grain box is placed outside the scintillator plate.

The volume needs to be long enough for the triton particle not to escape. The large number of collisions on the triton's path lead to a very small fluctuation in the path length. So, fortunately almost all tritons have a range very close to 30 µm. Further, the volume's lateral dimensions should be large enough to contain even the largest grains. With a default ZnS grain size of 7.5 µm, a box with dimensions 100 µm × 40 µm × 40 µm is sufficient for this. In case of simulations with smaller or larger grain sizes, it is possible to adjust the parameters via variables `/var/grainbox/grainBoxWidth` and `/var/grainbox/grainBoxLength`.

4.1.1 Radii of the Grains

The influence of grain size and volume ratio of ZnS has been examined in [4]. Unlike in their model, where the radii of all spheres are equal, our model allows for a certain variability in grain sizes, in order to examine the influence of the variance of radii on energy deposition. To determine radii for the single grains, it is necessary to choose a probability density function $p_r(r)$ with mean $\langle r \rangle$ and variance $\Delta r^2 := \langle r^2 \rangle - \langle r \rangle^2$ according to grain size s_{ZnS} and relative deviation σ^*_{ZnS}:

$$\langle r \rangle = \frac{s_{\mathrm{ZnS}}}{2}, \qquad \Delta r = \frac{\sigma^*_{\mathrm{ZnS}} \cdot s_{\mathrm{ZnS}}}{2}. \tag{4.1.1}$$

An obvious choice might be a normal distribution

$$p_r^n(r)dr = \frac{1}{\sigma\sqrt{2\pi}} \cdot e^{-\frac{(x-\mu)^2}{2\sigma^2}} \tag{4.1.2}$$

with $\mu = s_{\mathrm{ZnS}}/2$ and $\sigma = \sigma^*_{\mathrm{ZnS}} \cdot s_{\mathrm{ZnS}}/2$. However, for large relative deviations σ^*_{ZnS}, the probability for generating negative radii from this distribution cannot be neglected. The distribution would have to be cut off at $r = 0$, which would change the mean and the variance to analytically unobtainable values. Therefore it would be difficult to find parameters μ and σ such that mean and variance match the target.

Instead of cutting the probability density off, it is possible to replace it with the probability density function of a gamma distribution. This function is zero for $r < 0$ and thus negative radii are avoided, and for $\langle r\rangle \gg \Delta r$, the gamma distribution is close to the normal distribution [20].

Due to a limitation in Geant, which prohibits the creation of spheres with radii smaller than 10 nm, the gamma distribution must be shifted by $r_0 = 10\,\mathrm{nm}$:

$$\begin{aligned} p_r(r)dr &= \Theta(r - r_0)\frac{(r - r_0)^{k-1}}{\Gamma(k)\vartheta^k} \cdot e^{-\frac{r-r_0}{\vartheta}}dr \\ \text{with } \Theta(r) &= \begin{cases} 1, & r > 0 \\ 0, & \text{else} \end{cases} \\ \text{and } \Gamma(k) &= \int_0^\infty dt\ t^{k-1}e^{-t} \end{aligned} \tag{4.1.3}$$

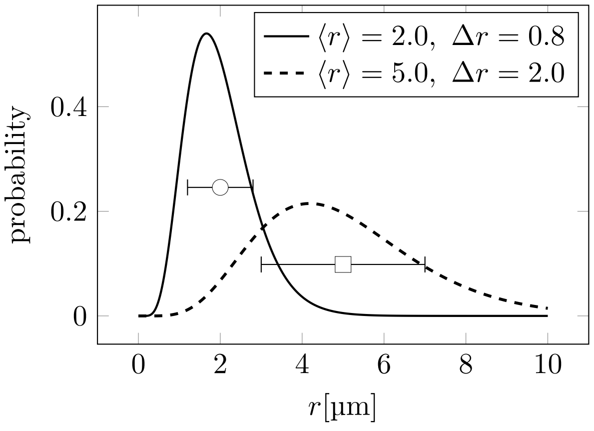

Fig. 4.3: Shifted gamma distribution for two sets of parameters. For this plot a shift of 0.1 mm was used.

The form of $p_r(r)$ is shown in Figure 4.3 for different parameters. The values of k and ϑ must be chosen such that (4.1.1) is fulfilled. To achieve this, it is necessary to calculate the first two momenta of our shifted distribution:

$$\begin{aligned} \langle r^n\rangle &= \int_{r_0}^\infty dr\ p_r(r)\ r^n = \int_0^\infty dt\ \vartheta\frac{(t\vartheta)^{k-1}e^{-t}}{\Gamma(k)\vartheta^k}(t\vartheta + r_0)^n \\ &= \sum_{m=0}^n \binom{n}{m}\frac{\vartheta^m r_0^{n-m}}{\Gamma(k)} \underbrace{\int_0^\infty dt\ t^{m+k-1}e^{-t}}_{\Gamma(m+k)} = \sum_{m=0}^n \binom{n}{m}\vartheta^m r_0^{n-m}\prod_{l=0}^{m-1}(k + l) \end{aligned} \tag{4.1.4}$$

In the last step we made use of the fact, that $\Gamma(k+1) = k\Gamma(k)$. With this general formula we obtain expressions for $\langle r \rangle$ and Δr:

$$\begin{aligned} \langle r \rangle &= r_0 + \vartheta k \\ \Delta r &= \sqrt{\langle r^2 \rangle - \langle r \rangle^2} = \sqrt{k} \cdot \vartheta \end{aligned} \tag{4.1.5}$$

Inverting this system of equations yields the necessary values for k and ϑ:

$$\begin{aligned} k &= \left(\frac{\langle r \rangle - r_0}{\Delta r} \right)^2 = \left(\frac{s_{\mathrm{ZnS}} - 2r_0}{\sigma^*_{\mathrm{ZnS}} \cdot s_{\mathrm{ZnS}}} \right)^2 \\ \vartheta &= \frac{\Delta r^2}{\langle r \rangle - r_0} = \frac{(\sigma^*_{\mathrm{ZnS}} \cdot s_{\mathrm{ZnS}})^2}{2(s_{\mathrm{ZnS}} - 2r_0)} \end{aligned} \tag{4.1.6}$$

With these parameters (4.1.3) is completely determined. How gamma distributed random numbers are generated is extensively discussed in [20]. In our simulation we use the `RandGamma` class of the `CLHEP` library, which is part of Geant. The shift is realized by addition of r_0 to every generated random number.

The number of spheres depends on the overall volume of ZnS:Ag divided by the spheres' mean volume. The volume of ZnS:Ag depends on mass ratios ϕ_X and material densities ρ_X and can be calculated from (A.2.3). The expectation value of a spherical volume with random radius distributed as in (4.1.3) can be calculated using (4.1.4)

$$\begin{aligned} \langle V_{\mathrm{sphere}} \rangle &= \frac{4}{3}\pi \langle r^3 \rangle = \frac{4}{3}\pi \left(r_0^3 + 3k\vartheta r_0^2 + 3k(k+1)\vartheta^2 r_0 + k(k+1)(k+2)\vartheta^3 \right) \\ &= \frac{4}{3}\pi \left(\frac{s_{\mathrm{ZnS}}}{2} \right)^2 \left(1 + 3{\sigma^*_{\mathrm{ZnS}}}^2 + \frac{2{\sigma^*_{\mathrm{ZnS}}}^4}{1 - \frac{2r_0}{s_{\mathrm{ZnS}}}} \right). \end{aligned} \tag{4.1.7}$$

4.1.2 Placement of the Grains

After determining the number of spheres and their radii, it is necessary to place them in the grain box volume without overlap. Prohibiting overlaps in the placement of grains is important in order to maintain the volume fraction. An overlap between two ZnS spheres would reduce the total volume of ZnS:Ag in the material, and in turn could distort the amount of energy deposited in it. The process of manufacturing scintillator screens involves mixing the grains very thoroughly in prolonged motion before adding the binder material and hardening it. Therefore it stands to reason that the grain placement is close to the distribution of fluid particles in thermal equilibrium.

One possibility to find positions for the grains would be to add them sequentially and randomly place each sphere at a possible position, such that it does not overlap with any other already placed sphere. However, according to [21] the distribution of distances between neighbouring spheres resulting from this method fundamentally differs from the one present in a fluid of spheres in thermal equilibrium.

In order to better approximate such a kind of placement, another method is employed as outlined in Algorithm 1. All spheres are placed completely randomly in the volume without regard for overlaps in line 4. After that, spheres which overlap are moved apart. This may result in new overlaps, so this step of removing overlap has to be repeated iteratively in the loop in line 6 until a configuration without overlap is reached. In order to prevent infinite loops one needs to define a maximum number of iterations, after which the algorithm terminates. In this case a warning is printed to inform the user of possible inaccuracies in the simulation.

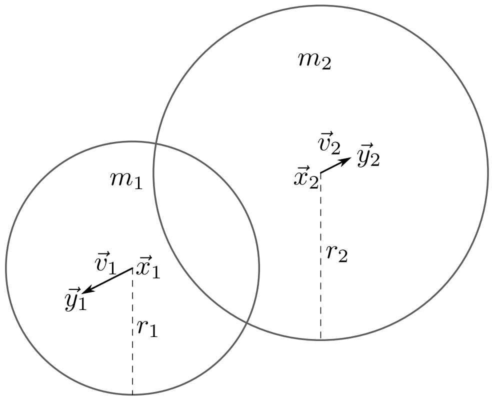

Fig. 4.4: Schematic of how far apart two spheres need to be moved in order to remove an overlap

Figure 4.4 shows two overlapping spheres at positions $\vec{x}_1$ and $\vec{x}_2$ which have to be moved apart to remove the overlap. If the new positions are $\vec{y}_{1/2}$, the displacement vectors are $\vec{v}_{1/2} = \vec{y}_{1/2} - \vec{x}_{1/2}$. After displacement, the distance of the spheres should be greater than the sum of their radii. So the minimal requirement is

$$|\vec{y}_2 - \vec{y}_1| \geq r_1 + r_2 \coloneqq R. \tag{4.1.8}$$

We attribute a mass $m_{1/2}$ to each of the spheres and require that the center of mass does not change due to the displacement:

$$\begin{aligned} m_1\vec{y}_1 + m_2\vec{y}_2 &= m_1\vec{x}_1 + m_2\vec{x}_2 \\ \Rightarrow \qquad m_1\vec{v}_1 &= -m_2\vec{v}_2 \end{aligned} \tag{4.1.9}$$

This way it is possible to have large spheres move less than small spheres, which minimizes the risk of creating new overlaps due to the displacement. A suitable mass value is proportional to a sphere's volume, with one exception. The LiF-sphere at the origin should stay in place, so it gets an arbitrarily huge mass of $m_0 = 1 \times 10^{127}$. From (4.1.9) follows, that the displacement vector must be proportional to the mass of the other sphere. Due to the symmetry of the problem, we choose the displacement vectors to be

Algorithm 1 Placement of spheres

```
Require: $k_{\max}$: maximum number of iterations
Require: $\vec{b} = (b_x, b_y, b_z)^T$: size of the grain box
Require: $N, r_1, \dots, r_N$: number of spheres and radius of each one
Require: $m_0, r_0$: mass and radius of void region
$\vec{x}_0 \leftarrow \frac{1}{2}\vec{b} +$ random vector with length smaller than $r_0$
for all $i$ in $\{1, \dots, N\}$ do
    $m_i \leftarrow r_i^3$
    $\vec{x}_i \leftarrow$ random position in grain box
$k \leftarrow 0$
repeat
    $k \leftarrow k + 1$
    $n_{ov} \leftarrow 0$                                              ▷ number of overlaps
    for all $i$ in $\{0, \dots\ N\}$ do
        $\vec{v}_i \leftarrow \vec{0}$
    for all pairs $i < j$ in $\{0, \dots, N\} \times \{0, \dots, N\}$ do
        $\vec{x}_m \leftarrow$ CLOSEST MIRROR($\vec{x}_i, \vec{x}_j, \vec{b}$)    ▷ algorithm 2
        $d \leftarrow |\vec{x}_i - \vec{x}_m|$
        $R \leftarrow r_i + r_j$
        if $d < R$ then
            $n_{ov} \leftarrow n_{ov} + 1$
            $\vec{v}_i \leftarrow \vec{v}_i + \frac{R-d}{d} \frac{m_j}{m_i + m_j} (\vec{x}_i - \vec{x}_m)$    ▷ see (4.1.11)
            $\vec{v}_j \leftarrow \vec{v}_j + \frac{R-d}{d} \frac{m_i}{m_i + m_j} (\vec{x}_m - \vec{x}_i)$    ▷ see (4.1.11)
    for all $i$ in $\{0, \cdots, N\}$ do
        $\xi \leftarrow$ random number between 1.1 and 1.3
        $\vec{x}_i \leftarrow$ MODULUS($\vec{x}_i + \xi \vec{v}_i, \vec{b}$)    ▷ algorithm 3
until $n_{ov} = 0$ or $k > k_{\max}$
if $n_{ov} > 0$ then
    print a warning!
```

parallel to the connection vector $\vec{v}_{1/2} = \lambda \cdot m_{2/1}(\vec{x}_{1/2} - \vec{x}_{2/1})$. Plugging this into (4.1.8) we obtain the proportionality factor λ:

$$\begin{aligned} R &\leq |\vec{x}_2 + \vec{v}_2 - \vec{x}_1 - \vec{v}_1| = |\vec{x}_2 - \vec{x}_1 + \lambda(m_1 + m_2)(\vec{x}_2 - \vec{x}_1)| \\ &= |1 + \lambda(m_1 + m_2)| \cdot \underbrace{|\vec{x}_2 - \vec{x}_1|}_{-:d} \\ \Rightarrow \qquad \lambda &\geq \frac{R-d}{d(m_1+m_2)} \qquad \vee \qquad \lambda \leq -\frac{R+d}{d(m_1+m_2)} \end{aligned} \tag{4.1.10}$$

We obtain two solutions for λ and choose the one which does not move the spheres through each other, so that the minimal displacement vectors used in lines 17 and 18 are

$$\vec{v}_{1/2} = \frac{R-d}{d}\,\frac{m_{2/1}}{m_1+m_2}(\vec{x}_{1/2}-\vec{x}_{2/1}) \tag{4.1.11}$$

This is the displacement necessary for the spheres to exactly touch each other after the displacement. Due to numerical inaccuracies, such a displacement could result in a state, where the numerical distance d is smaller than the required distance R, but the resulting displacement vectors are too small for the floating point precision to change the position vectors at all. This is why each displacement vector is multiplied with a random number between 1.1 and 1.3 in line 21

For a performance boost, it is advisable to implement an octree structure, which omits distance checks between spheres which are far apart from each other. This is especially advantageous when the grain size s_{ZnS} is very small and there are many spheres to place. Care must be taken for periodic boundary conditions described below to be implemented correctly in the octree structure.

At each iteration of the placement algorithm, all overlapping pairs of spheres are examined and the displacement vectors are summed up. Then the displacement of all spheres is done simultaneously, and the next iteration is started.

When moving a sphere, it may happen that the new position lies outside the grain box. To prevent this, periodic boundary conditions are enforced. This not only means that movement of a sphere beyond a boundary results in a movement to the other side of the box as in Algorithm 3. When a sphere is placed closer to a boundary than its radius, such that it sticks out of the boundary, it should "feel" the overlap with spheres on the other side of the grain box. To facilitate this, Algorithm 1 does not simply calculate the distance between two sphere positions, but rather the distance between closest mirrors, which is calculated by Algorithm 2. This function generates all possible mirror positions of one of two spheres with respect to the grain box boundaries and returns the one which is closest to the unmirrored sphere.

Algorithm 2 Calculate which mirror point of $\vec{x}_2$ is closest to $\vec{x}_1$

```
function CLOSEST MIRROR($\vec{x}_1, \vec{x}_2, \vec{b}$)
    $mirrors$ ← list containing the tuple $\{|\vec{x}_1 - \vec{x}_2|, \vec{x}_2\}$ as single element
    for all $(s_x, s_y, s_z)$ in $\{-1,1\} \times \{-1,1\} \times \{-1,1\}$ do
        $\vec{x}_m \leftarrow \vec{x}_2 + (s_x \cdot b_x, s_y \cdot b_y, s_z \cdot b_z)^T$
        add $\{|\vec{x}_1 - \vec{x}_m|, \vec{x}_m\}$ to $mirrors$
    $\{d, \vec{x}_m\}$ ← distance-vector tuple from $mirrors$ with smallest $d$
    return $\vec{x}_m$
```

Algorithm 3 Calculate modulus of vector $\vec{x}$ w.r.t. the bounding box $\vec{b}$

```
function MODULUS($\vec{x}, \vec{b}$)
    $x_1, x_2, x_3 \leftarrow$ components of $\vec{x}$
    $b_1, b_2, b_3 \leftarrow$ components of $\vec{b}$
    for all $i$ in $\{1, 2, 3\}$ do
        while $x_i < 0$ do
            $x_i \leftarrow x_i + b_i$
        while $x_i > b_i$ do
            $x_i \leftarrow x_i - b_i$
    return $(x_1, x_2, x_3)^T$
```

After determining the positions, the spheres are added to the grain box volume. Each sphere close to a boundary is copied to the opposite side of the grain box as shown in Figure 4.5.

The periodic boundary conditions together with the prohibition of overlap ensure that the full volume of every ZnS sphere lies inside the grain box at each run. Thus, the volume ratios are not distorted by geometric effects and only vary due to the grain radii being randomly distributed.

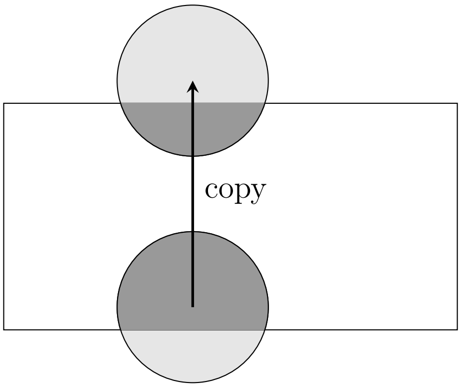

Fig. 4.5: A sphere close to a box boundary is copied to the opposite side and the copy is checked for overlaps as well. The darker area represents the active volume inside the grain box, the lighter area is not part of the simulation.

4.2 Scintillator Plate

The scintillator plate is modelled as a rectangular plate with adjustable width, height and thickness. Its material is a homogeneous mixture with the same constituents as the grain box: ZnS:Ag, LiF and the binder material with their respective mass ratios. The probability for the capture of an incoming neutron depends on the kinetic energy and the density of ^{6}Li nuclei in the scintillator plate. The energy dependence can be found in [9] (see Figure 4.6) and is included in the Geant's inelastic neutron scattering database `G4NDL4.2`. The $\propto E^{-1/2}$ dependence can be explained by the fact that neutrons with smaller energy are slower and therefore stay in the vicinity of a ^{6}Li nucleus for a longer period of time. Thus, the overlap of wave functions of neutron and nucleus integrated over time is larger, which leads to an increasing probability of the neutron tunneling into the nucleus. The time spend close to a nucleus is directly proportional to the inverse of the neutron's velocity, and for non-relativistic neutrons $v \propto \sqrt{E}$

variable name	symbol	default value	description
`/var/scint/thickness`	d	$0.4\,\mathrm{mm}$	Thickness of scintillator plate
`/var/global/width`	w	$5\,\mathrm{cm}$	Width of scintillator plate
`/var/global/height`	h	$5\,\mathrm{cm}$	Height of scintillator plate
`/var/global/scintYield`	–	1	Scintillation yield factor
`/var/scint/aluminiumMount`	–	`false`	Whether to use an aluminium plate behind scintillator
`/var/scint/doubleScint`	–	`false`	Whether to place a second scintillator behind WLSF screen
`/var/global/gapLength`	g	$2\,\mathrm{mm}$	Gap between both scintillators
`/var/global/partLiF`	ϕ_{LiF}	1	Mass fraction of LiF
`/var/global/partZnS`	ϕ_{ZnS}	2	Mass fraction of ZnS:Ag
`/var/global/partBinder`	ϕ_{binder}	1	Mass fraction of binder material
`/var/global/grainSizeLiF`	s_{LiF}	$2.5\,\mathrm{\mu m}$	Grain size of LiF grains
`/var/global/grainSizeZnS`	s_{ZnS}	$7.5\,\mathrm{\mu m}$	Grain size of ZnS grains
`/var/global/binderDensity`	ρ_{binder}	$1\,\mathrm{g\,cm^{-3}}$	Density of the binder material
`/var/scint/binderAbsorptionLength`	$\lambda_{\mathrm{binder}}/\lambda_l$	$0.4\,\mathrm{mm}$	Optical attenuation length of binder or effective attenuation length
`/var/scint/binderRindex`	n_{binder}	1.41	Refractive index of binder material
`/var/scint/surfacePolish`	–	0.1	Value for smoothness of the scintillator's surface
`/var/scint/scintYieldZnS`	C	$250\,\mathrm{keV^{-1}}$	Absolute scintillation efficiency of ZnS:Ag
`/var/scint/fastTimeScint`	τ_f	$60\,\mathrm{ns}$	Decay time for fast scintillation mode
`/var/scint/slowTimeScint`	τ_s	$1\,\mathrm{\mu s}$	Decay time for slow scintillation mode
`/var/scint/yieldRatio`	–	0.5	Ratio of photons in fast decay mode
`/var/scint/primaryParticleType`	–	0	0 = neutrons, 1 = photons
`/var/scint/numberPrimaryParticles`	N_{primary}	1	Number of particles per event
`/var/scint/neutronEnergy`	E_{kin}	$25\,\mathrm{meV}$	Neutron's kinetic energy
`/var/scint/photonWavelength`	λ_p	$402\,\mathrm{nm}$	Initial photon's wavelength
`/var/scint/photonInteractionType`	–	1	0 = random walk, 1 = effective absorption length

Table 4.2: Parameters used by the scintillator plate module with their respective default values.

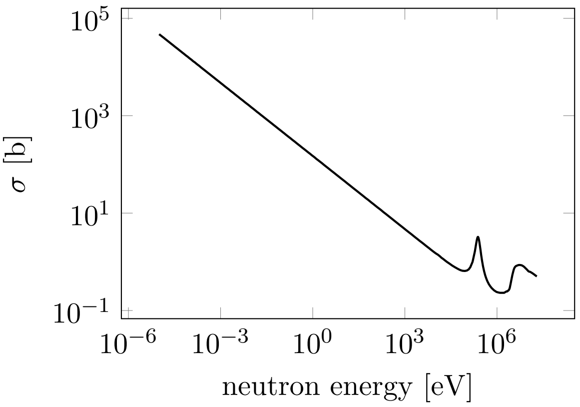

Fig. 4.6: Cross section σ for a neutron capture of a ^{6}Li nucleus depending on the neutron's kinetic energy. Source: [9]

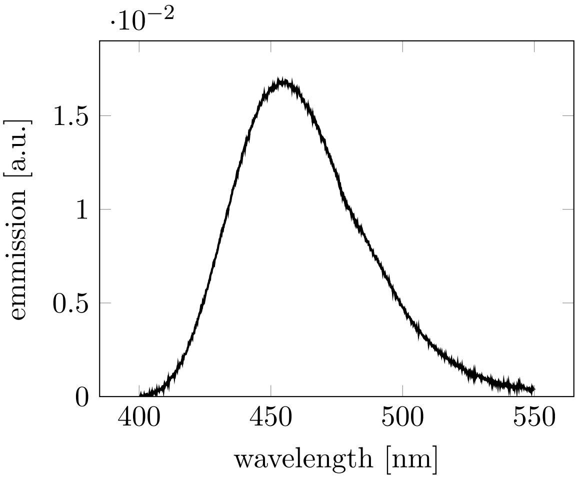

Fig. 4.7: Emission spectrum of ZnS:Ag dependent on the photon wavelength.

leads to the observed behaviour. The irregularities which occur for energies above 10 keV are resonance peaks, where the neutron energy equals an excitation energy of the nucleus.

When Geant determines that a neutron is captured by a ^{6}Li nucleus, the track is killed immediately, and in its stead an alpha and a triton are created as secondary particles. These particles traverse the scintillator plate and deposit energy along their paths. The ionization processes responsible for this are already implemented in Geant.

The whole plate is defined as a scintillator by specifying the necessary material properties described in Section 3.3. Both `FASTCOMPONENT` and `SLOWCOMPONENT` are set to the same spectrum, which is shown in Figure 4.7. The constant properties are freely adjustable to potentially enable adjustments to the decay time or scintillation efficiency of the scintillator without need to recompile.

Because the whole plate is a scintillator, the total kinetic energy of 4.78 MeV contributes to the creation of scintillation photons. In order to simulate the effect, that not all energy is deposited in ZnS grains, the grain box module (see Section 4.1) adjusts the scintillation yield to a value proportional to the energy deposited in ZnS grains of the grain box. This way the amount of photons created depends on the energy deposited in ZnS grains and varies statistically for each event. It also means that a simulation which includes the creation of scintillation photons needs to have the grain box module enabled in order to obtain correct results.

4.2.1 Effective Optical Attenuation Length

The microscopic structure of the scintillator cannot be simulated across the whole scintillator plate, because generating and randomly positioning ZnS and LiF grains would require too much time and memory space. Therefore, the propagation of photons inside the scintillator plate must be treated in a special way.

The easiest method is to define the material of the scintillator plate as an optically homogeneous material with a certain effective photon attenuation length λ_l. This method has the advantage of being very fast, because every photon will have only one tracking step to be calculated inside the plate. Either the photon is absorbed inside the plate or it reaches the surface. This method has the disadvantage, that microscopic parameters cannot influence the simulation directly. In the best case, there is a well defined dependence between parameters like mass ratio, grain sizes etc. and the effective attenuation length. In the worst case, however, the effective attenuation length has to be measured for each configuration, which would mean that the simulation cannot be extended to arbitrary parameters without a measurement of the optical parameters of a real sample. This would limit the applicability of the model. To examine the dependence of the effective attenuation length on microscopic parameters, measurements of the former have been conducted for several scintillator samples (see Section 5.2).

4.2.2 Random Walk Pseudo Process

Another possibility is to define a custom process, which emulates reflection and refraction at virtual material boundaries with random orientations. The boundaries are virtual in the sense that they are not part of the detector geometry and only arise in the context of the random walk process. Such a process can take into account microscopic parameters like grain sizes and mass ratio and does not depend on an external macroscopic parameter. The disadvantage of employing such a process is a long runtime because each photon undergoes many hits and changes of direction inside the scintillator plate, which means that many tracking steps are required for each scintillation photon.

The process needs to implement the function `GetMeanFreePath()`, which calculates the path length a photon travels on average before hitting a boundary, and `PostStepDoIt()`, which is called whenever a photon "hits" a boundary.

Calculation of the Deflection Angle

Keeping spheres as model grains, the angle under which a photon hits a grain surface can be derived from geometrical considerations. As shown in Figure 4.8, the excentricity of the photon equals the cosine of the angle between photon ray and surface normal. Since the photon's position is equally distributed over the projection circle (grey in the figure), the probability for the photon to hit at a certain excentricity r is proportional to the circumference of a circle with radius r. So, including a normalization factor, the cosine of the incident angle of the photon is distributed according to the distribution function

$$p_{\cos(\theta)} = 2\cos(\theta), \qquad \text{for } 0 \leq \cos(\theta) \leq 1. \tag{4.2.1}$$

θ does not fully determine the surface normal. One also needs to fix the lateral angle ϕ randomly. As our model grains are spheres and thus radially symmetric, each possible value for ϕ between 0 and 2π is equally probable.

As shown in Figure 4.9, a photon changes its direction by the angle θ_{refl} or θ_{refr} depending on the incident angle θ_1 and on whether it is reflected or refracted. If it is reflected, the excident angle equals the incident angle and the deflection angle is

$$\theta_{\text{refl}} = \pi - 2\theta_1. \tag{4.2.2}$$

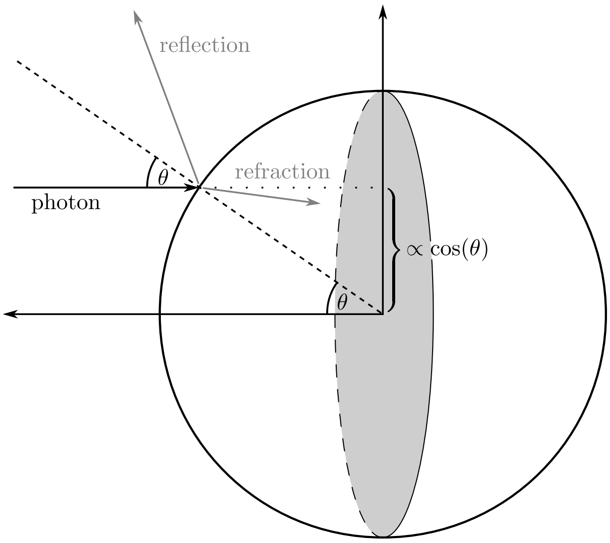

Fig. 4.8: Schematic of a photon hitting a sphere. The excentricity of the ray is the cosine of the hit angle θ. Since the ray can hit the projection of the sphere anywhere with equal probability, the cosine is distributed linearly.

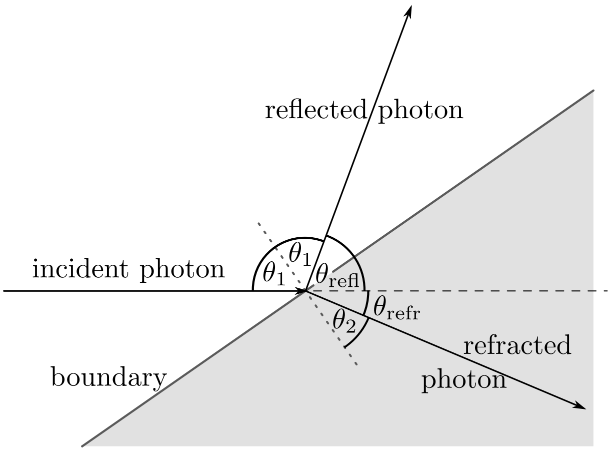

Fig. 4.9: An incident photon will change its direction by the angle of either θ_{refl} or θ_{refr} depending on whether it is reflected or refracted.

If a photon is refracted, the angle of refraction is given by Snell's law: $\sin(\theta_2) = \frac{n_1}{n_2}\sin(\theta_1)$. With this, the deflection angle is

$$\theta_{\text{refr}} = \theta_1 - \theta_2 = \theta_1 - \arcsin\left(\frac{n_1}{n_2}\sin(\theta_1)\right). \tag{4.2.3}$$

Given the lateral angle ϕ and the deflection angle $\theta_\Delta := \theta_{\text{refl/refr}}$ the photon's new direction vector in Carthesian coordinates where the z-axis coincides with the initial direction of the photon is

$$\vec{n}(\theta_\Delta, \phi) = \begin{pmatrix} \sin(\theta_\Delta)\cdot\cos(\phi) \\ \sin(\theta_\Delta)\cdot\sin(\phi) \\ \cos(\theta_\Delta) \end{pmatrix}. \tag{4.2.4}$$

The new global direction vector is then obtained by multiplying it with a rotation matrix which maps the z-axis to the initial global direction, as defined by (A.3.6).

Only the sine and cosine of θ_Δ and ϕ are needed, so it is more efficient to determine those values directly instead of invoking the trigonometrical functions. For ϕ this can be achieved by repeatedly drawing two uniformly distributed random numbers x and y from the interval $[-1, 1]$ until a pair is drawn which fulfils $x^2 + y^2 \leq 1$. For such a pair one can assign $\cos\phi = \frac{x}{\sqrt{x^2+y^2}}$ and $\sin\phi = \frac{y}{\sqrt{x^2+y^2}}$.

The sine and cosine of θ_Δ are different for reflected and refracted photons. In case of a reflected photon as in (4.2.2) the cosine is

$$\cos(\theta_\Delta) = \cos(\pi - 2\theta_1) = -\cos(2\theta_1) = \sin^2(\theta_1) - \cos^2(\theta_1) = 1 - 2\cos^2(\theta_1). \tag{4.2.5}$$

In case of refraction we get from (4.2.3)

$$\cos(\theta_\Delta) = \cos\left(\theta_1 - \arcsin\left(\frac{n_1}{n_2}\sin(\theta_1)\right)\right) = \cos(\theta_1)\sqrt{1 - \left(\frac{n_1}{n_2}\sin(\theta_1)\right)^2} + \frac{n_1}{n_2}\sin^2(\theta_1), \tag{4.2.6}$$

where the $\sin^2(\theta_1)$ can be replaced by $1 - \cos^2(\theta_1)$, so that it is sufficient to determine the cosine of the incident angle, as per (4.2.1). For that, one needs to generate random numbers which follow the given distribution.

There are many available algorithms for creating uniformally distributed random numbers between 0 and 1. Applying a function $f : [0, 1] \to \mathbb{R}$ to random numbers generated in this way, one creates random numbers with a different distribution. The cumulative distribution function is then

$$P_f(f(x) \leq \eta) = \int\limits_{f(x)\leq\eta} dx\ 1 \tag{4.2.7}$$

If we assume f to be continuous and monotonically increasing, we can invert it and write integral boundaries if $f(0) \leq \eta \leq f(1)$:

$$P_f(f(x) \leq \eta) = \int\limits_0^{f^{-1}(\eta)} dx\ 1 = f^{-1}(\eta) \tag{4.2.8}$$

The distribution function is then the derivative of this function with respect to η:

$$p_f(\eta) = \frac{d}{d\eta} f^{-1}(\eta) \tag{4.2.9}$$

So, in order to generate random numbers following the distribution function (4.2.1), where η corresponds to $\cos(\theta)$, we need a function $f(x)$ such that

$$\frac{d}{d\eta} f^{-1}(\eta) = 2\eta \qquad \Rightarrow \qquad \underbrace{f^{-1}(\eta)}_{x} = \eta^2 \qquad \Rightarrow \qquad f(x) = \sqrt{x}. \tag{4.2.10}$$

Therefore, $\cos\theta_1$ can be obtained by taking the square root of an uniformally distributed random number between 0 and 1.

Whether a photon hitting the medium boundary with change of refractive index from n_1 to n_2 will be reflected or refracted is governed by Fresnel's law [22]. The probabilities depend on the polarization of the photon with respect to the plane spanned by the boundary's normal vector and the propagation vector of the photon (see Figure 4.10). For s-polarized (perpendicular) photons, the probability for reflection is

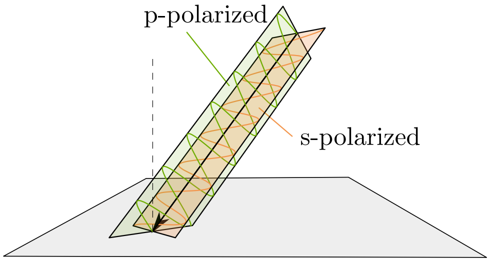

Fig. 4.10: The s-polarized and p-polarized planes for a photon hitting a planary medium boundary.

$$p^s_{\text{refl}}(\theta_1) = \left(\frac{\frac{n_1}{n_2}\cos(\theta_1) - \sqrt{1 - \left(\frac{n_1}{n_2}\sin(\theta_1)\right)^2}}{\frac{n_1}{n_2}\cos(\theta_1) + \sqrt{1 - \left(\frac{n_1}{n_2}\sin(\theta_1)\right)^2}} \right)^2, \tag{4.2.11}$$

Algorithm 4 Determine change of direction

```
function PostStepDoIt($track$, $step$)
    $m \leftarrow$ current material of $track$
    if $m$ equals binder material then
        $m^* \leftarrow$ random material, weights according to $W_X$ defined in (4.2.15)
    else
        $m^* \leftarrow$ binder material
    $E \leftarrow$ current kinetic energy of $track$
    $n_1, n_2 \leftarrow$ refractive index of $m$ and $m^*$ for energy $E$
    $\chi \leftarrow$ uniformly distributed random number in $[0, 1]$
    $cos, sin \leftarrow \sqrt{\chi}, \sqrt{1-\chi}$          ▷ $\cos(\theta_1), \sin(\theta_1)$ according to (4.2.10)
    $\chi \leftarrow$ uniformly distributed random number in $[0, 1]$
    if $\chi < \frac{1}{2}(p^s_{\text{refl}} + p^p_{\text{refl}})$ then          ▷ reflection, see (4.2.11) and (4.2.12)
        $cosd \leftarrow 1 - 2cos^2$          ▷ $\cos(\theta_\Delta)$ according to (4.2.5)
    else          ▷ refraction
        $cosd \leftarrow cos\sqrt{1 - \left(\frac{n_1}{n_2}sin\right)^2} + \frac{n_1}{n_2}sin^2$          ▷ $\cos(\theta_\Delta)$ according to (4.2.6)
    $sind \leftarrow \sqrt{1 - cosd^2}$
    repeat
        $x, y \leftarrow$ uniformly distributed random numbers in $[-1, 1]$
    until $x^2 + y^2 < 1$
    $r \leftarrow \sqrt{x^2 + y^2}$
    $sinp, cosp \leftarrow x/r, y/r$          ▷ $\sin(\phi)$ and $\cos(\phi)$
    $\vec{p} \leftarrow (sind \cdot cosp, sind \cdot sinp, cosd)^T$
    $(e_1, e_2, e_3) \leftarrow$ current photon direction
    $\mathbf{A} \leftarrow \frac{1}{\sqrt{1-e_3^2}} \begin{pmatrix} e_2 & e_1 n_3 & e_1\sqrt{1-e_3^2} \\ -e_1 & e_2 n_3 & e_2\sqrt{1-e_3^2} \\ 0 & -(1-e_3^2) & e_3\sqrt{1-e_3^2} \end{pmatrix}$          ▷ according to (A.3.6)
    return $\mathbf{A} \cdot \vec{p}$          ▷ new direction in global coordinates
```

for p-polarized (perpendicular) photons it is

$$p^p_{\text{refl}}(\theta_1) = \left(\frac{\cos(\theta_1) - \frac{n_1}{n_2}\sqrt{1 - \left(\frac{n_1}{n_2}\sin(\theta_1)\right)^2}}{\cos(\theta_1) + \frac{n_1}{n_2}\sqrt{1 - \left(\frac{n_1}{n_2}\sin(\theta_1)\right)^2}} \right)^2 . \qquad (4.2.12)$$

Unpolarized light contains s-polarized and p-polarized photons in equal parts and is reflected with the combined probability $\frac{1}{2}\left(p^s_{\text{refl}} + p^p_{\text{refl}}\right)$. In the case of scintillation light the photons are created with random polarization, which means that this is the appropriate probability of reflection.

A summary is given by Algorithm 4. The algorithm starts with determining the cosine of the lateral angle in line 10. Then an equally distributed random number between 0 and 1 is drawn and compared with $\frac{1}{2}(p^s_{\text{refl}} + p^p_{\text{refl}})$ in order to determine whether the photon is reflected or refracted. Depending on that, the cosine of the correct deflection angle is calculated according to (4.2.5) or (4.2.6) whereupon it is possible to calculate the new photon direction in line 22, which is subsequently rotated to global coordinates.

One should note that the expression $\sqrt{1 - \left(\frac{n_1}{n_2}\sin(\theta_1)\right)^2}$ is needed in (4.2.6) as well as in (4.2.11) and (4.2.12), so that it is advantageous to calculate it only once and store it for subsequent use.

Mean Free Path

The mean free path of a photon before it hits a grain boundary can be calculated as the inverse stopping probability in an infinitesimal slice of material. Consider a slice shown in Figure 4.11 with frontal area L^2 and thickness Δ_x. The number of grains of type X contained in this slice is

$$N_X = \frac{V_X}{\langle v_X \rangle} \underset{\text{(A.2.3)}}{=} \frac{L^2 \Delta_x}{\langle v_X \rangle} \cdot \frac{\frac{\phi_X}{\rho_X}}{\sum \frac{\phi_Y}{\rho_Y}}, \tag{4.2.13}$$

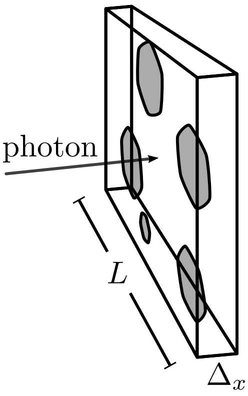

Fig. 4.11: Simple model of a material slice of a grained material

where v_X is the volume of a single grain and X can be either ZnS or LiF. The cross section σ_X of a grain is the geometrical expectation value of the projected surface of one grain, i.e. $\sigma_X = \langle a_X \rangle$.With these values it is possible to calculate the probability that a photon passing through the slice $L^2\Delta_x$ interacts with a grain of type X:

$$P(\text{interaction with } X) = \frac{\sigma_X N_X}{L^2} = \frac{\langle a_X \rangle}{\langle v_X \rangle} \cdot \frac{\frac{\phi_X}{\rho_X}}{\sum \frac{\phi_Y}{\rho_Y}} \Delta_x = W_X \cdot \Delta_x, \tag{4.2.14}$$

where in the last step we defined the interaction weight W_X of the material X. This approximation is only valid for small Δ_x (because of obstruction effects), and in this limit the interaction probablilities of ZnS and LiF can be added together:

$$P(\Delta_x) := P(\text{interaction in } L^2\Delta_x) = \Delta_x \sum_{\text{ZnS,LiF}} W_X = \frac{\Delta_x}{l}, \tag{4.2.15}$$

where in the last step we defined l, which later turns out to be the mean free path length

$$l := \left(\sum_{\text{ZnS,LiF}} W_X \right)^{-1} . \tag{4.2.16}$$

To obtain the attenuation law dependent on the path length x, we divide the path into N slices of thickness $\Delta_x = x/N$ and calculate the probability of the photon not interacting in the first $N-1$ slices and then interacting in the last slice:

$$P(x,N) = \left(1 - P\left(\frac{x}{N}\right)\right)^{N-1} \cdot P\left(\frac{x}{N}\right). \tag{4.2.17}$$

In the limit $N \to \infty$ the probability density $P(x,N)/\Delta_x$ becomes the exponential function

$$p(x) := \lim_{N\to\infty} \frac{P(x,N)}{\Delta_x} = \lim_{N\to\infty} \frac{1}{l} \left(1 - \frac{x}{Nl}\right)^{N-1} = \frac{e^{-\frac{x}{l}}}{l} \tag{4.2.18}$$

and it follows that l is the mean free path of a photon.

The quotient of mean cross section and mean volume depends on the geometry of the grain type. For instance, spherical grains with fixed grain radius of $R_X = \frac{s_X}{2}$ yield $\frac{\langle a_X \rangle}{\langle v_X \rangle} = \frac{3}{4R_X}$. Spheres with a normally distributed radius $R_X \pm \Delta R_X$ yield

$$\frac{\langle a_X \rangle}{\langle v_X \rangle} = \frac{\pi \langle r^2 \rangle}{\frac{4}{3}\pi \langle r^3 \rangle} = \frac{R_X^2 + \Delta R_X^2}{\frac{4}{3}\left(R_X^3 + 3R_X \Delta R_X^2\right)} = \frac{3}{4R_X} \cdot \frac{1 + \left(\frac{\Delta R_X}{R_X}\right)^2}{1 + 3\left(\frac{\Delta R_X}{R_X}\right)^2}. \tag{4.2.19}$$

Similarly, a Gamma distribution of radii leads to

$$\frac{\langle a_X \rangle}{\langle v_X \rangle} = \frac{3}{4R_X} \cdot \frac{1 + \left(\frac{\Delta R_X}{R_X}\right)^2}{1 + 3\left(\frac{\Delta R_X}{R_X}\right)^2 + 2\left(\frac{\Delta R_X}{R_X}\right)^4} = \frac{3}{4R_X} \cdot \frac{1}{1 + 2\left(\frac{\Delta R_X}{R_X}\right)^2}. \tag{4.2.20}$$

The extra factors for the case with varying radii are plotted in Figure 4.12. For finite variance the factor is smaller than one, which means that the mean free path length is larger than in the case with fixed grain radii. This would also translate to an increased effective attenuation length due to less scattering.

Finally, a shifted gamma distribution as defined in (4.1.3) yields

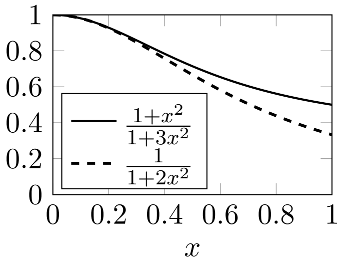

Fig. 4.12: Plot of the extra factors of (4.2.19) and (4.2.20) with respect to the case with fixed radii.

$$\frac{\langle a_X\rangle}{\langle v_X\rangle} = \frac{3}{4R_X}\cdot\frac{1+\left(\frac{\Delta R_X}{R_X}\right)^2}{1+3\left(\frac{\Delta R_X}{R_X}\right)^2+2\left(\frac{\Delta R_X}{R_X}\right)^4\left(1-\frac{r_0}{R_X}\right)^{-1}} \tag{4.2.21}$$

However, for values $r_0/R_X \sim 10^{-3}$ as in our case, this function is indistinguishable from the result of a simple gamma function. In our simulations we therefore use (4.2.20) for calculating the mean free path length for optical photons in the scintillator plate.

As a photon encounters a virtual grain boundary it is necessary to determine the grain type in order to obtain the refractive index at the boundary. The probability to hit a certain grain is distributed according to the weigths W_X introduced in (4.2.14). In the simulation a uniformally distributed random number is drawn from the interval $[0, W_{\mathrm{ZnS}} + W_{\mathrm{LiF}}]$ whenever a photon hits a virtual boundary. If this number is below W_{ZnS}, the process assumes that a ZnS grain was hit, a LiF grain otherwise.

If the photon is refracted, the random walk process considers the photon to enter the grain. This changes optical properties like refractive index and optical attenuation length, but also the mean free path of the random walk process itself, because the path length then depends on the grain size only and not on the grain density. The average section length of a line intersecting a sphere of radius r at random excentricity is

$$l_r = \frac{1}{\pi r^2}\int_0^r d\rho \int_0^{2\pi} d\phi\ \rho\cdot 2\sqrt{r^2-\rho^2} = \frac{4}{3}r, \tag{4.2.22}$$

where ρ is the excentricity as shown in Figure 4.13.

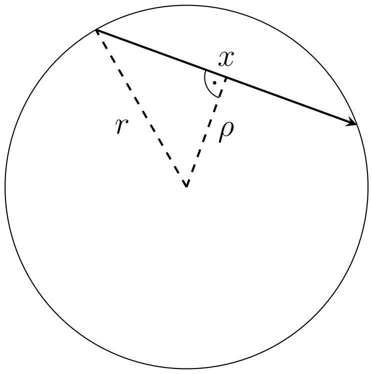

Fig. 4.13: The path travelled through a sphere of radius r at excentricity ρ. In this consideration we have $x = 2\sqrt{r^2-\rho^2}$.

Therefore, $\frac{2}{3}s_X$ is adopted as the new mean free path of the random walk process.

If a virtual boundary is encountered while the photon is inside a virtual grain, the medium beyond the boundary is always considered to be the binder material. If the photon is refracted, it enters the binder material again, if it is reflected, it stays inside the grain. This way, the attenuation lengths of different materials excert an influence proportional to the distances the photons travel inside them.

Due to the composite structure of the scintillation material, the surface of the scintillator plate is not smooth, but rough. Since Geant treats boundary surfaces as smooth and polished per default, it is necessary to define its roughness. That way, whenever an optical photon hits the scintillator surface, the normal vector used for reflection or refraction will be randomly altered.

4.2.3 Mie-Scattering

The scattering of light at perfect spheres has already been solved analytically in 1908 by Gustav Mie [23]. The solution was approximated for spheres of radius similar to the light's wavelength by Henyey and Greenstein in 1941 [24]. This approximation is implemented in the Geant process `G4OpMieHG`, and is readily available.

However, this process handles scattering processes as singular events. At no time is the photon considered to be inside a particle, and thus only the attenuation length of the binder material is considered. This attenuation length would either have to be modified like in Section 4.2.1 or an additional custom process would have to emulate the absorption in ZnS grains. Further, the approximation was done for the very diluted interstellar dust particles. It is unclear if it holds for very densely packed grains.

Geant's implementation of the Mie process is designed for one type of particles only, and since ZnS and LiF grains have different sizes and refractive indices this is not sufficient. So, in order to use the Mie process in our simulations, further extensions to the library or a custom implementation of the process would be required. Because of the approximation's shortcomings discussed earlier, this has not been done in the scope of this work.

4.3 Wavelength Shifting Fibers

The WLSFs are naturally modelled as long straight cylinders running along the scintillator plate. The bend at the edge of the plate, which leads the fibers back to the PMTs, is very sharp. This way is it possible to place several detector modules next to each other with little dead space in between them. After the sharp bend, the fiber continues on an arbitrary path to the PMT. In our model we include the sharp bend at the edge, but keep the following part straight. So, the model of a fiber consists of two to three cylinders joined by one or two quarter tori, depending on whether both fiber ends are read out or not.

The length of the straight fiber segments is as long as the scintillator plate is wide, or high respectively. The thickness of the fiber and the distance between two fibers is adjustable independently for both layers. Further adjustable geometric parameters are

variable name	symbol	default value	description
`/var/global/width`	w	5 cm	Length of horizontal fibers
`/var/global/height`	h	5 cm	Length of vertical fibers
`/var/wls/distanceToPMT`	b	30 cm	Length of fiber segments from scintillator to PMT
`/var/wls/thickness`	d_f	0.1 cm	Fiber diameter
`/var/wls/bendRadius`	r_b	6 mm	Bending radius at scintillator edges
`/var/wls/claddingRatio`	–	0.03	Quotient of cladding thickness and fiber radius
`/var/wls/dyeConcentrationPPM`	ρ_{dye}	200	Dye concentration in parts per million
`/var/wls/dyeType`	–	7	Dye type: 7, 8 or 11 (see Figure 4.14)
`/var/wls/claddingAbsLength`	λ_c	5 mm	Optical attenuation length in the outer cladding
`/var/wls/duplexReadOut`	–	`false`	Whether both fiber endings should lead to PMTs
`/var/wls/multiCladding`	–	`true`	Whether WLSF has two cladding layers
`/var/wls/gapBetweenFibersHori`	g_h	1 mm	Distance between two horizontal fibers
`/var/wls/gapBetweenFibersVert`	g_v	1 mm	Distance between two vertical fibers
`/var/wls/quantumEfficiency`	p_q	0.25	Detection efficiency of PMTs.

Table 4.3: Parameters used by the WLSF module with their respective default values.

bending radius and the segment length leading back to the PMT.

The fiber cladding is realized by a concentric hierarchy of cylinders and tori. The outermost structure represents the outermost cladding material, and contains the next layer as daughter volume and so forth. It is possible to choose single cladding and double cladding for the simulation.

Finally, the PMTs are modelled as simple cylidric slabs of glass, which detect photons entering them. There is the possiblity to specify the PMT's efficiency p_q. If such a number between zero and one is specified, a hit is only registered with probability p_q. This probability models the photo cathode's quantum efficiency as well as any further sources of loss in the signal chain. It is not strictly necessary to use this feature, since it is possible to randomly filter photon events during analysis.

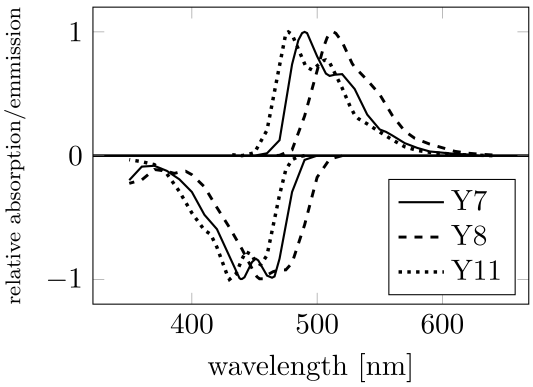

Fig. 4.14: Dye's emission (above 0) and absorption (below zero) spectra of optical light for three different dye types, provided by the manufacturer Kuraray [25].

The WLS dye is characterized by its absorption- and emission spectra, and for our simulation we adopted the spectra provided by the manufacturer Kuraray (see Figure 4.14). These spectra are read into the program from files, which contain the data in plain text, and set as material properties `WLSABSLENGTH` and `WLSCOMPONENT` (see Section 3.4) of the core material. Kuraray's Y-11 dye has a decay time of 12 ns [26], which is used as the decay time in the simulation via material property `WLSFTIMECONSTANT`. The decay times of Y-7 and Y-8 are of the same order of magnitude as Y-11 [27] and thus insignificant in comparison with the decay time of the scintillator. This is why the decay time is the same for all dye types in our simulations.

The form of absorption spectra is always the same as shown in Figure 4.14, but absolute values of attenuation lengths depend on the dye concentration, which is adjustable via `/var/wls/dyeConcentrationPPM`. The attenuation of two dyed fibers, where one fiber is twice as long, but has only half the dye concentration, is equal, because the amount of dye particles in both fibers is the same. More generally, given an arbitrary multiplicative factor χ, light traversing the length $\chi \cdot d$ of a fiber with dye concentration ρ_{dye} is attenuated by the same amount as light traversing the length d of a fiber with dye concentration $\chi \cdot \rho_{\text{dye}}$. Thus, the transmitted intensity must depend on the product of the two and can be written as

$$I(\lambda) = I_0(\lambda) \cdot e^{-k(\lambda)\rho_{\text{dye}} d}, \tag{4.3.1}$$

where λ is the wavelength and $k(\lambda)$ is a wavelength dependent proportionality factor. The wavelength dependence of $k(\lambda)$ has been measured by KURARAY for different dye types and the results are shown in the absorption part of Figure 4.14. The absorption length is defined as the inverse coefficent of the exponent:

$$\lambda_{\text{dye}} = \frac{1}{k(\lambda)\rho_{\text{dye}}} \tag{4.3.2}$$

In order to obtain absolute values for $k(\lambda)$, the transmittance I/I_0 needs to be measured with monochomatic light of wavelength λ and fixed thickness and dye concentration. Then, the absolute value of $k(\lambda)$ at this wavelength can be calculated from (4.3.1). The results of measurements conducted by KURARAY are shown in Table 4.4. Fig-

dye type	ρ_{dye}[ppm]	d[mm]	λ_p[nm]	I/I_0[%]	$k(\lambda_p)$[ppm^{-1}mm^{-1}]
Y7	24.8	10	439	3.61	0.0134
Y8	34.5	10	455	4.49	0.0090
Y11	18.2	10	430	6.89	0.0147

Table 4.4: Results of transmission measurements conducted by KURARAY. For each dye type a 10 cm cube with dye concentration ρ_{dye} was illuminated at the wavelength λ_p of maximum absorption of the dye type. The resulting value for $k(\lambda_p)$ can be used to obtain a value for the absorption length of a WLSF.

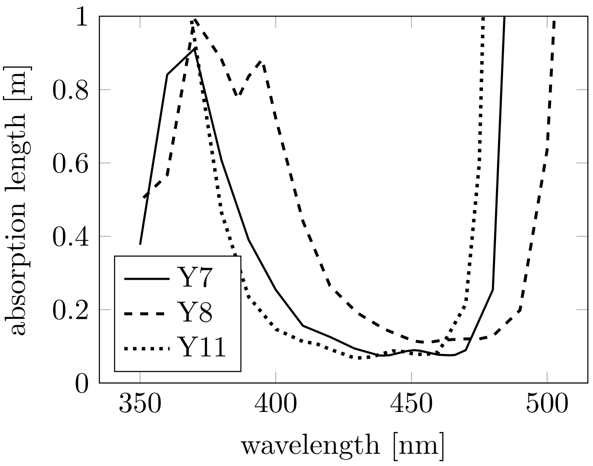

Fig. 4.15: Total optical attenuation length depending on photon wavelength for a dye concentration of 1 ppm^{-1}.

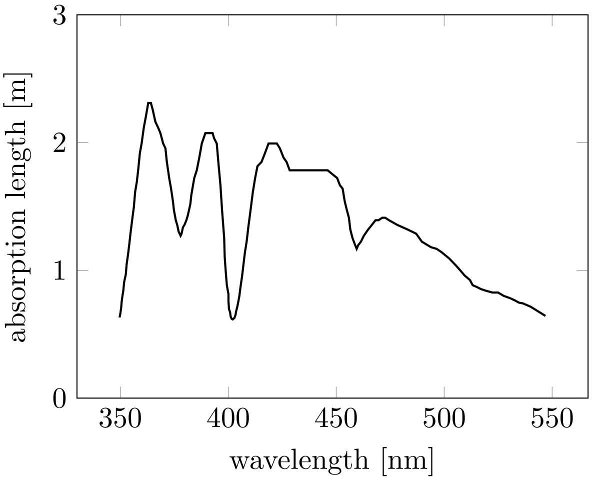

Fig. 4.16: Absorption length of a photon in a clear fiber depending on its wavelength according to [28].

ure 4.15 shows the absolute values for the attenuation length λ_{dye} for a dye concentration of $\rho_{\text{dye}} = 1\text{ppm}^{-1}$. For a different dye concentration these have to be multiplied with a factor of $(\rho_{\text{dye}}[\text{ppm}])^{-1}$ according to (4.3.2).

The absorption length for optical photons in the fiber (besides absorption by the WLS process) is defined as the absorption length of a clear fiber according to [28] as shown in Figure 4.16. This property is independent of dye concentration or any other parameter.

The outermost cladding receives a much shorter absorption length, as described in Section 2.5.1. For simplicity it is adjustable and constant for all photon energies because there is no data provided about it. A default value of about 5 mm seems appropriate, given that undesired photons travel at least 1.29 cm inside the outer cladding when guided along a 30 cm fiber (see Appendix A.1).

variable name	symbol	default value	description
`/var/photoncounter/width`	w_{pc}	30.0 mm	Width of the cylinder
`/var/photoncounter/thickness`	–	0.01 mm	Thickness of the cylinder
`/var/global/gapLength`	g	0.4 cm	Needed for correct placement
`/var/photoncounter/distance`	g_{pc}	0 mm	Distance between cylinder and scintillator plate
`/var/photoncounter/rindex`	n_{pc}	1.5	Refractive index of the cylinder's material

Table 4.5: Parameters used by the photon counter module with their respective default values.

4.4 Photon Counter

The photon counter is a small module for counting photons which exit the scintillator plate. It consists of two oblate cylinders defined as sensitive detectors in front and back of the first scintillator plate. The dimensions of the cylinder and its distance to the scintillator can be adjusted freely by setting the respective variables mentioned in Table 4.5. This way it is possible to simulate measurements of scintillator samples without WLSFs. In this case, the refractive index can be set to that of a PMT's photo cathode such that it simulates a PMT mounted behind the scintillator plate.

However, with refractive index equal to that of air, it is also possible to use the photon counter in simulations including WLSFs. The photon counter stores not only the amount of photons passing through, but also the photons' positions and whether they exited on the front or on the back of the scintillator. This way it is possible to get a picture of how the exiting photons are distributed across the surface.

Chapter 5

Validation of the Model

A validation of the model is necessary in order to be able to trust its results. Since the detector consists of several parts it would be very difficult to directly validate the model as a whole. Therefore, the different parts of the model were validated separately at first. For this, simulations of single modules have been carried out and the results compared to theoretical expectation and/or experimental measurements. Finally, the entire detector model was simulated and compared to measurements of one of the detector banks for SAPHiR.

5.1 Neutron Attenuation in the Scintillator Plate

A simple validation step is to compare the neutron absorption of the scintillator plate in simulation and measurements. This way it is checked whether the neutron cross sections and mass ratios are calculated correctly.

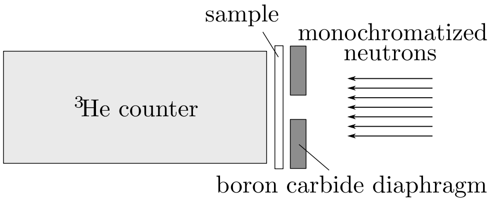

Fig. 5.1: Setup of a neutron absorption measurement.

Figure 5.1 shows the setup of the measurement. A monochromatic neutron source provides neutrons with a single wavelength. Using a ^{3}He proportional counter the neutron flux is measured with and without a scintillator sample between source and detector. The transmission rate is the quotient of the two measured neutron fluxes. In this measurement the scintillator plate only functions as an absorber and not as a detector itself. A monochromatic neutron source is necessary, because the lithium's cross section for neutron capture depends on the kinetic energy of the neutron as discussed in Section 4.2.

The measurement described here was conducted by Ralf Engels and Günter Kemmerling in February 2013 at the HEiDi instrument at the FRM-II [29]. HEiDi utilizes neutrons from a hot neutron source, monochromatized via a Germanium single crystal. During the measurement the reflexes (422) and (311) were used, which give two different neutron wavelengths (see Table 5.1). In order to get a well defined beam, a boron carbide diaphragm with hole diameter of 2 cm was placed in front of the sample. The ^{10}B inside the diaphragm (approximately 20 % of natural boron is ^{10}B) absorbs all neutrons which do not pass through the diaphragm's hole.

Table 5.1 shows most of the results mentioned in [29]. We exclude measurements of ELJ scintillators which were backed by a Mylar foil. Because the Mylar's polyethylene contains hydrogen, neutrons passing through the foil may scatter there and miss the ^{3}He detector. This way the measured absorption is too high. Here we include only ELJ samples backed by an aluminium foil, which has a very low interaction probability. The Applied Scintillation Technologies (AST) samples are without backing, so all of them are included.

In order to compare simulation and measurement it is necessary to determine the microscopic parameters mentioned in Table 4.1. The mass ratios, grain sizes, and the densities of ZnS and LiF are readily available in sample specifications. However, the density of the binder material is usually not provided by manufacturers and needs to be obtained from the measurements. This is possible by measuring the absorption coefficient of the scintillator material and calculating which binder density leads to such an absorption coefficient.

The lithium's cross section σ is defined as the quotient of the absorption coefficient $\mu = \lambda_n^{-1}$ and the particle density η_{Li} of ^{6}Li:

$$\sigma = \frac{\mu}{\eta_{\mathrm{Li}}} \tag{5.1.1}$$

σ depends on the neutron's wavelength and can be obtained from Figure 4.6. The attenuation coefficient can be obtained by absorption measurements. If the neutron beam intensity is I_0 before passing the scintillator and I afterwards, the absorption coefficent is

$$\mu = \frac{\ln(I_0/I)}{d}. \tag{5.1.2}$$

The particle density is the total number N_{Li} of ^{6}Li nuclei divided by the total volume. N_{Li} in turn is the total mass of LiF divided by the combined mass of ^{6}Li and fluorine nuclei, such that

$$\eta_{\text{Li}} = \frac{N_{\text{Li}}}{V} = \frac{1}{V} \cdot \frac{M_{\text{Li}}}{m_{\text{Li}} + m_{\text{F}}} = \frac{V_{\text{Li}}}{V} \cdot \frac{\rho_{\text{LiF}}}{m_{\text{Li}} + m_{\text{F}}} \underset{\text{(A.2.3)}}{=} \frac{\phi_{\text{LiF}}}{\sum \frac{\phi_X}{\rho_X}} \cdot \frac{1}{m_{\text{Li}} + m_{\text{F}}}. \tag{5.1.3}$$

The sum over X in the denominator contains a term for the binder, which is the single dependency on the binder density. Combining (5.1.1) and (5.1.3) yields an expression for the binder density after a few trivial transformations:

$$\rho_{\text{binder}} = \phi_{\text{binder}} \cdot \left(\frac{\phi_{\text{LiF}} \cdot d \cdot \sigma}{(m_{\text{Li}} + m_{\text{F}}) \ln (I_0/I)} - \frac{\phi_{\text{LiF}}}{\rho_{\text{LiF}}} - \frac{\phi_{\text{ZnS}}}{\rho_{\text{ZnS}}} \right)^{-1} \tag{5.1.4}$$

Mass fractions ϕ_X as well as the thickness d are provided by the manufacturers of the samples and the densities of ZnS:Ag and LiF are given in Appendix A.2. The masses of ^{6}Li and F are $m_{\text{Li}} = 9.9883 \times 10^{-24}\,\text{g}$ and $m_{\text{F}} = 3.154 \times 10^{-23}\,\text{g}$ [30, 31]. The quantity to be measured is the transmission ratio I/I_0, which determines the value for the binder density.

As Table 5.1 shows, the measured binder densities show some tendencies. For all measurements with a neutron wavelength of 1.1695 Å the binder density is lower than for the respective measurement at 0.794 Å. This might indicate a systematic difference in the measurement with the two neutron beams.

With the exception of the 4:1:1 AST scintillators, the calculated binder density decreases with increasing thickness. One might assume that this behaviour is due to the imperfect collimation of the neutron beam. If we assume a setup as shown in Figure 5.2 with an isotropic neutron beam where a neutron under the angle $0 \leq \theta \leq \delta$ travels a distance $d/\cos\theta$ through the scintillator plate, the beam intensity behind a scintillator plate of thickness d is

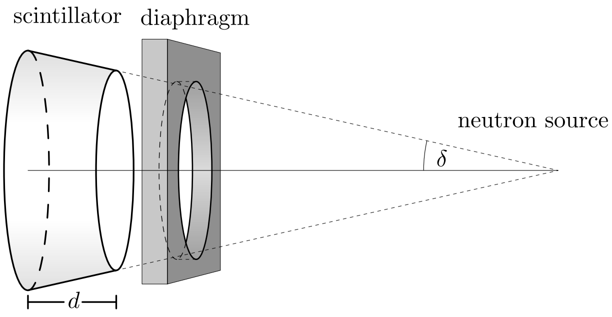

Fig. 5.2: An incoherent neutron beam passes the scintillator plate in a conic section. Almost all neutrons traverse a distance longer than d.

$$\frac{I(d)}{I_0} = \frac{\int_0^{\delta} d\theta \int_0^{2\pi} d\phi \, \sin\theta \cdot \exp\left(-\frac{d}{\lambda_n \cos\theta}\right)}{\int_0^{\delta} d\theta \int_0^{2\pi} d\phi \, \sin\theta} = \frac{1}{1-\cos\delta} \int_1^{(\cos\theta)^{-1}} dy \, \frac{e^{-\frac{d}{\lambda_n} y}}{y^2}, \tag{5.1.5}$$

where we substituted $y = 1/\cos\theta$. If we calculate the effective binder density ρ^*_{binder}

as in (5.1.4) with I/I_0 from 5.1.5, we get a value which decreases with d as can be seen in Figure 5.3 for an opening angle of $\delta = 0.3 \approx 17°$. However, this figure shows, that even for such a large opening angle the measured binder density varies by only 0.002 % over the thickness range of 0.2 mm to 0.4 mm, so the geometric effect can be ruled out. As of now it is unclear what causes the apparent decrease of binder density.

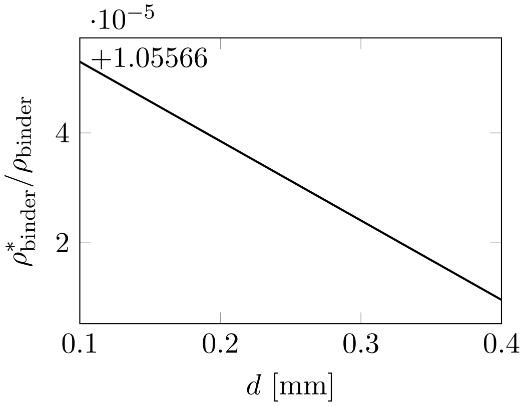

Fig. 5.3: Dependence of the effective binder density ρ^*_{binder} on the scintillator thickness d for an opening angle $\delta = 0.3 \approx 17°$, which is already a very large value. Notice that the change in binder density is in fact small, since the vertical axis is shifted by $1.583\,48\,\mathrm{g\,cm^{-3}}$.

Another interesting fact is that for AST scintillators the binder density seems to increase with increasing ZnS mass ratio, while for ELJ scintillators it seems to decrease. If LiF and binder mass ratios stay fixed while the ZnS ratio increases, a configuration will be reached, where there is not enough binder material in the mixture to fill out the whole interior space between the grains, so that air pockets can form inside the scintillator. In such a case the density of the material between the grains would decrease, as is the case with ELJ scintillators. Why the binder density increases in the case of AST scintillators is an open question.

For our simulations we chose to use different binder density values for samples of different manufacturers, because it stands to reason that different binder materials have been used. For AST scintillators we use the average of all binder densities of AST samples in Table 5.1, while for ELJ scintillators we exclude the two 3.2:1:1 samples. These two samples show a binder density which is much lower than the otherwise very similar values. The results are:

$$\rho^{\text{AST}}_{\text{binder}} = 1.58\,\mathrm{g\,cm^{-3}}, \qquad \rho^{\text{ELJ}}_{\text{binder}} = 1.98\,\mathrm{g\,cm^{-3}} \tag{5.1.6}$$

Table 5.1 also shows a comparison between measurement and simulation of the neutron absorbtion rate. The simulated values fit quite well with the measurement except for ELJEN's 3.2:1:1 scintillators, which show an abnormally low binder density as discussed earlier. In summary, the experiments described in this section are able to validate the aspect of neutron capture in the scintillator plate and also provide values for the binder densities of AST's and ELJEN's scintillators.

	serial no.	ZnS:Ag mass ratio	thickness [µm]	measured absorption [%]		binder density [g cm^{-3}]		simulated absorption [%]	
				0.794 Å	1.1695 Å	0.794 Å	1.1695 Å	0.794 Å	1.1695 Å
AST	23166	2	200	13.2	17.7	1.99	1.66	12.86	17.79
	23168	2	300	19.1	25.7	1.98	1.73	19.23	24.75
	23173	2	400	22.3	29.7	1.49	1.32	23.35	32.09
	23174	3	200	11.6	15.4	2.15	1.66	10.77	15.47
	23178	3	300	15.1	19.9	1.49	1.21	15.55	22.47
	23182	3	400	18.7	25.2	1.30	1.16	20.59	28.48
	23184	4	200	10.3	13.4	2.30	1.57	9.37	13.62
	23188	4	300	13.0	17.1	1.35	1.06	13.74	19.48
	23191	4	400	18.2	23.9	1.71	1.34	18.97	25.83
ELJ	4085-03-01	2	320	20.10	27.70	1.94	1.84	20.27	29.02
	4085-04-01	2	500	28.10	38.20	1.65	1.62	30.49	40.88
	4318-01-01	3.2	320	15.80	21.40	1.54	1.34	20.43	28.51
	4318-02-01	3.2	500	22.60	30.60	1.35	1.24	25.31	35.35
	4318-03-01	2	320	20.40	28.00	2.03	1.90	20.27	29.02
	4318-04-01	2	500	29.40	39.70	1.90	1.83	30.49	40.88
	4318-07-01	1	320	24.60	33.30	2.11	1.99	23.60	32.86
	4318-08-01	1	500	35.50	46.70	2.08	1.96	35.60	47.90

Table 5.1: Summary of measurement data from [29] and simulation results. Measurements have been conducted at two different wavelengths at the FRM-II in Munich. Mass ratios were ϕ_{ZnS}:1:1 for all samples. The absorption means the fraction of neutrons captured in the scintillator plate. The simulation used the scintillator plate module (Section 4.2) only. Binder densities were adapted to values mentioned in (5.1.6). `/var/global/scintYield` was set to zero in order to supress photon creation. Neutron energy, mass ratios and scintillator thickness were set to the values given in the table.

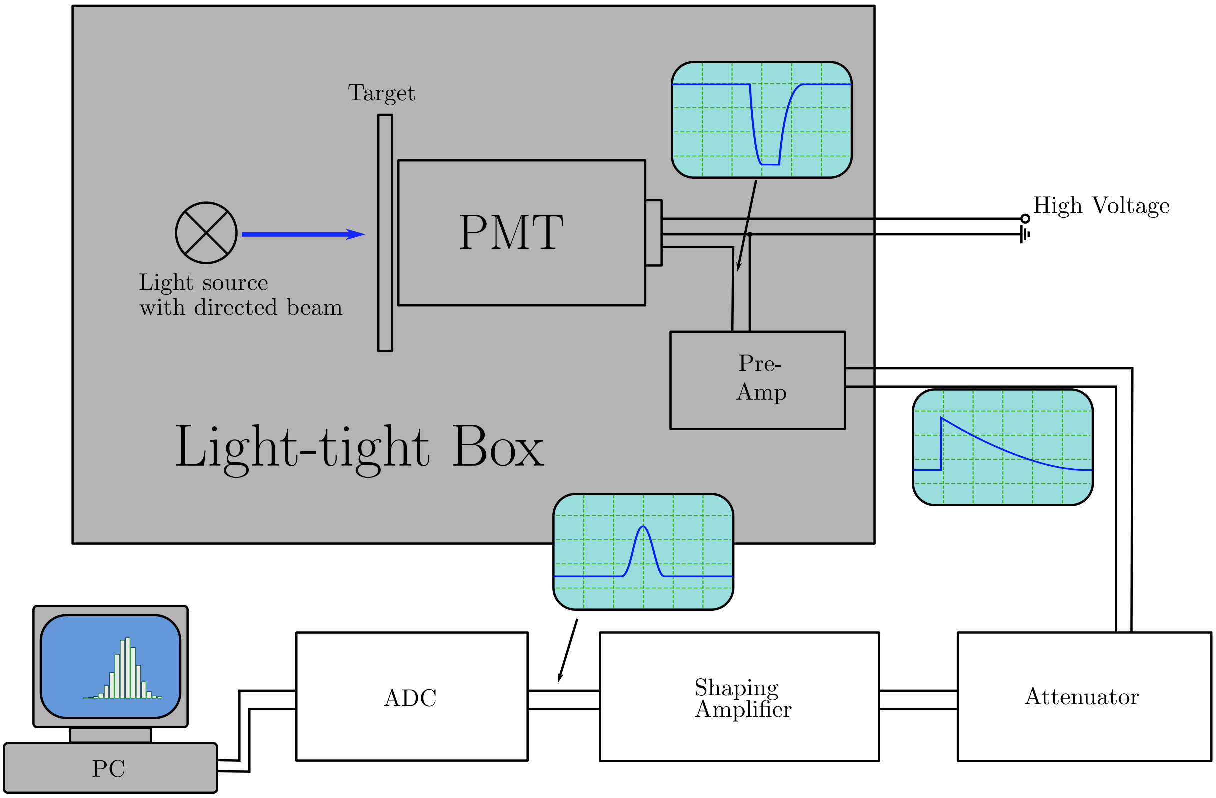

Figure 5.4: Setup for transmission measurements. The PMT signal is amplified in a pre-amplifier and then, if necessary, attenuated by some factor of 2^n. After a shaping amplifier creates pulses for the ADC to digitize, the computer records the pulse data in a histogram.

5.2 Light Attenuation Measurements

In order to examine the propagation of light inside the scintillator plate and to validate our optical processes, the transmission of light emitted by a blue Light Emitting Diode (LED)was measured for several scintillator samples.

The common setup of measurements is shown in Figure 5.4. A blue LED directs a pulsed beam at the target, of which we want to measure the optical transmission. The LED is mounted behind a very narrow diaphragm with 0.5 mm hole diameter in order to illuminate only a small region of the target. The target is mounted directly in front of a PMT, in which transmitted photons are detected.

The PMT produces signals, which closely resemble the pulse shape of the light source. Due to capacitative effects, the signal has a small intrinsic rising and falling edge. These signals are fed into a pre-amplifier, which integrates the signal by collecting charges on a capacitor, which slowly discharges through a high-Ohmic resistor. The discharging current is amplified, so that signals with sharp rising edges and long tails are produced. This way longer lasting pulses of the LED result in higher signals from the pre-amplifier.

The differential shaping amplifier creates gaussian pulses, which the Analog Digital Converter (ADC) can easily convert into digital signals. The attenuator between pre-amplifier and shaping amplifier is necessary because the possible output range of the pre-amplifier is much larger than the possible input range of the shaping amplifier before it goes into saturation. Besides the unipolar signal output which is fed into the ADC, the Shaping amplifier has a second, bipolar signal output, so that it is possible to monitor the bipolar signal on an oscilloscope and adjust the attenuation factor in case of saturation.

The ADC digitizes the pulse heights of the unipolar signals and sends that information to a PC, where the values are binned in a histogram. This way we obtain information about the pulse strength of the light reaching the PMT after passing the target.

5.2.1 Light Source

The blue LED is driven by a pulse generator and provides pulses of blue light with a spectrum in the range of the ZnS:Ag emission spectrum. Figure 5.5 shows a comparison of the optical emission spectra of LED and ZnS:Ag. The amplitude of the pulses is kept constant in order to prevent damage to the LED, so that the intensity of pulses is varied by changing the pulse width.

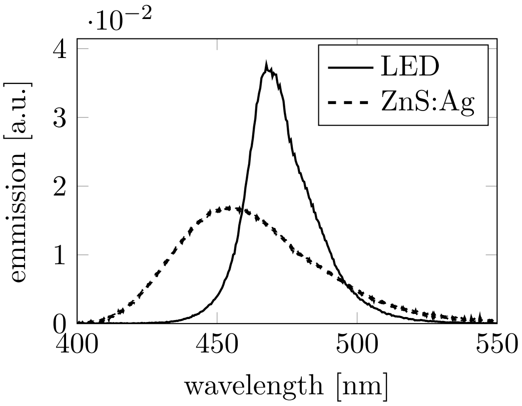

Fig. 5.5: Emmission spectra of the scintillator material and the blue LED used in the transmission measurements.

To determine the absolute absorption rates of different targets, it is necessary to calibrate the LED pulse. Therefore the PMT's response to the LED without target was measured for several pulse widths. However, the pulse widths necessary to generate measurable signals with scintillator targets lead to signal saturation in the pre-amplifier when the beam is not attenuated.

Therefore, we measured the transmissions for several pulse widths of several optical attenuators – in our case sheets of paper – while insuring that attenuators of similar strength have several pulse widths in common. The result is shown in Figure 5.6(a). To obtain the initial pulse strengths, one can now patch the intensity curves of different attenuators together by calculating the mean attenuation factor for overlapping regions and multiplying the data of stronger attenuators with this factor. The result is shown in Figure 5.6(b).

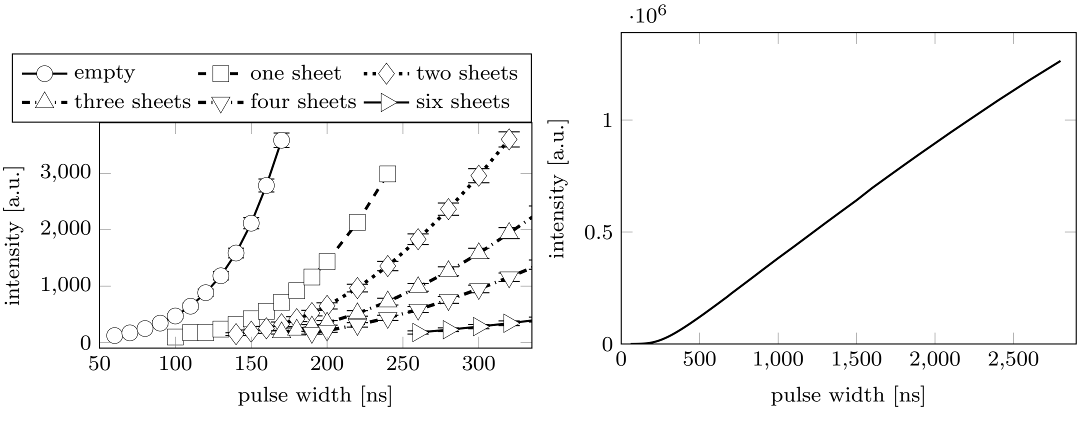

Figure 5.6: Calibration measurements for the LED. (a) shows the measured light intensity reaching the PMT with different number of absorbers plotted against the pulse width. The different measurements are patched together in (b) and show the total intensity of the non-attenuated pulse which can be used as basis for total absorption measurements.

5.2.2 Absolute Light Transmission

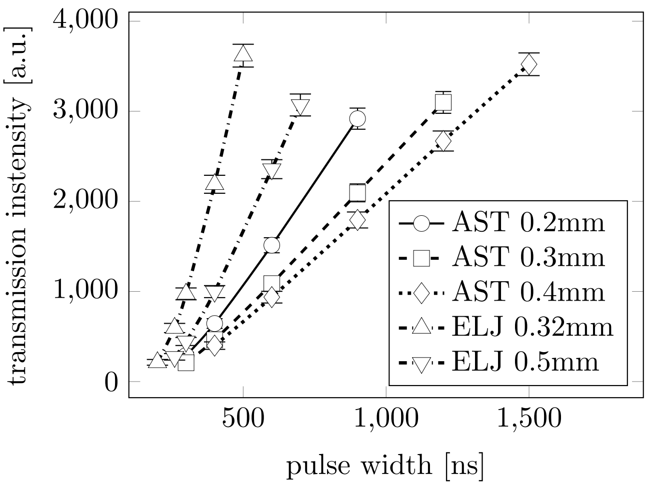

Fig. 5.7: Total transmission signal strength of certain scintillator samples at different pulse widths. The AST samples shown are the ones with 4:1 ZnS/LiF ratio.

For the absolute transmission measurements, the target in Figure 5.4 consists solely of a scintillator plate. There are samples from two manufacturers, namely AST and ELJ. The AST samples vary in thickness from 0.2 mm to 0.4 mm and have a ZnS to LiF ratio of 2:1, 3:1 and 4:1. As discussed in Section 5.1, several of the ELJ samples have an aluminium backing, which is completely opaque for visible light. Therefore only two samples with Mylar backing could be used in these measurements. The used samples had thicknesses of 0.32 mm and 0.5 mm, and a ZnS:Ag/LiF ratio of 2:1.

The transmission of each sample is measured at several pulse widths. Figure 5.7 shows the transmission signal strengths of several samples depending on five different pulse widths each. The quotient of the transmission signal strength and the initial signal strength (see Figure 5.6(b)) then yields the transmission factor, which is constant for each

	serial no.	thickness [mm]	ZnS:Ag/LiF ratio	transmission rate [%]
AST	23166	0.2	2:1	0.81(3)
	23168	0.3	2:1	0.73(2)
	23173	0.4	2:1	0.66(2)
	23174	0.2	3:1	0.69(2)
	23178	0.3	3:1	0.71(2)
	23182	0.4	3:1	0.539(18)
	23184	0.2	4:1	0.88(3)
	23188	0.3	4:1	0.63(2)
	23191	0.4	4:1	0.546(18)
ELJ	4085-05-01	0.32	2:1	2.98(9)
	4085-06-01	0.5	2:1	1.37(5)

Table 5.2: Absolute transmission values of several samples using the LED light source.

sample and is shown in Table 5.2.

Figure 5.8 visualizes the data in a semi-logarithmic plot. The transmission of AST scintillators loosely follows an exponential attenuation law with axis intercept of about one percent. The fact that it differs from 100 % (full transmission at zero thickness) can be ascribed to surface effects, such as partial reflection of the incoming beam, which are independent of the sample's thickness. How much of the light is lost at which surface cannot be discerned from the data.

Also, it is not possible to differentiate between samples of different ZnS:Ag/LiF ratios with regard to an optical attenuation length. Their values are too entangled to make significant statements about the dependence of the attenuation length on compositional parameters. It is further noteworthy that the AST 3:1 0.3 mm sample has a higher transmission rate than the thinner AST 3:1 0.2 mm sample. Although the difference is not significant (0.71(2) % vs 0.69(2) %), it hints at poor homogeneity in our samples.

Since only two ELJ samples have been measured, the number of fit parameters of the exponential attenuation law equals the number of degrees of freedom. Thus there is no possibility for error estimation, and the validity of the exponential law cannot be confirmed. However if we assume its validity, it means that ELJ scintillators have smaller surface effects, which lead to a higher total tranmission rate, but their effective attenuation length is shorter. In the WLSF detector, light will be produced in ZnS grains inside the scintillator, so the influence of surface effects will be not as significant as in the transmission measurements. This is why the AST scintillators might be a better choice than ELJ. However, in order to confirm this, measurements of additional ELJ samples

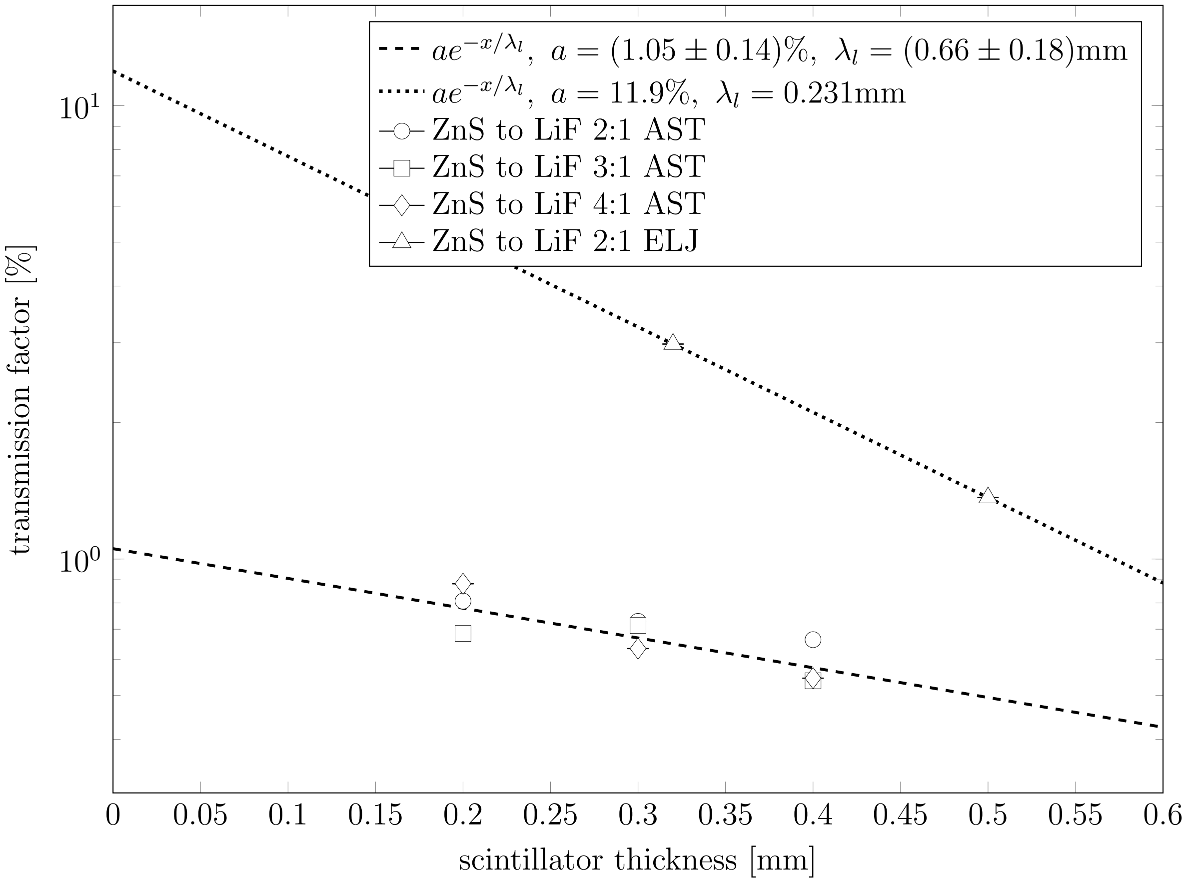

Figure 5.8: Absolute transmission values of several samples using the LED light source. The thickness dependent transmission value was fitted for different manufacturers. Since there are only two data points for ELJ, there is no error estimation. The fact that the transmission at zero thickness does not equal unity can be attributed to surface effects.

are necessary.

5.2.3 Comparison With Simulations

The two models of photon propagation described in sections 4.2.1 and 4.2.2 require different input parameters. As the model of effective attenuation length does not depend on microscopic parameters, it requires only the scintillator thickness and a value for the optical attenuation length. The latter is a result of the measurement described above.

The model of virtual grain boundaries requires scintillator thickness, mass ratios, and grain sizes, as well as density, refractive index, and absorption length of the binder material. Similar to the binder density in Section 5.1, other properties of the binder material are not easily available and have to be guessed or estimated.

Early studies of ZnS/LiF scintillator plates reported the use of Polyethylene (PE) [32],

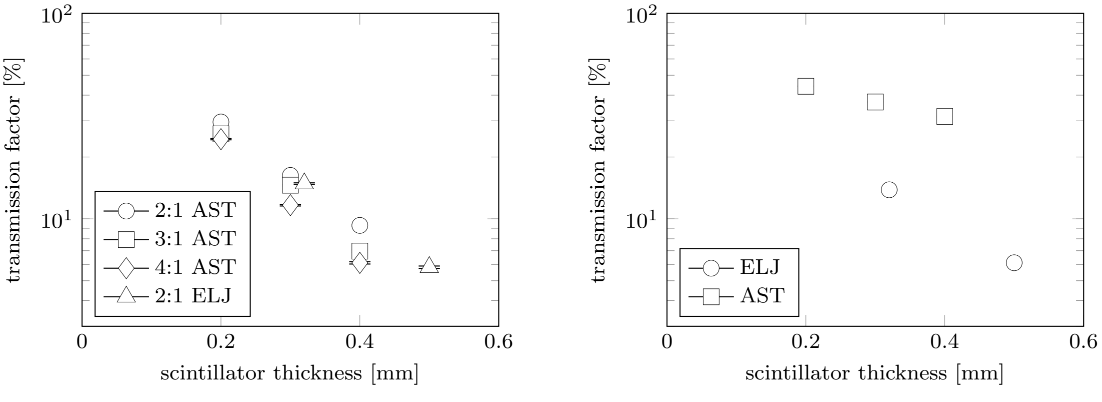

(a) **(b)**

Figure 5.9: Simulated optical transmission factor for the compositions measured in the experiment. The results were obtained by using modules of scintillator plate and photon counter and optical photons as primary particles. (a) was simulated using the random walk process described in Section4.2.2. Binder densities were chosen according to 5.1.6, the attenuation length of the binder material is $\lambda_{\text{binder}} = 20\,\text{cm}$. In (b) an effective attenuation length has been used according to values fitted in Figure 5.8. Since this value has been fitted without regard to mass ratios, the only parameter is the scintillator thickness.

process type	manufacturer	ZnS/LiF	a [%]	λ_{eff} [mm]
random walk process	AST	2:1	95	0.17
	AST	3:1	95	0.15
	AST	4:1	99	0.14
	ELJ	2:1	78	0.19
effective attenuation length	AST	—	62	0.59
	ELJ	—	59	0.22

Table 5.3: Parameters of an exponential fit of the form $a \cdot \exp(-d/\lambda_{\text{eff}})$ to the simulation results shown in Figure 5.9.

Lucite (i.e. PMMA) [33] or epoxy [34] as binder material. With an attenuation length of 0.45 mm at 404 nm [35], PE probably is not a favourable choice for a binder, because it might absorb a significant fraction of the scintillation light. With an attenuation length of the order of 1.5 m at 440 nm [36], PMMA is much better suited. Since there are many types of epoxy compounds, including some which are completely opaque when hardened, it is not possible to give an estimate for its attenuation length. Thus, manufacturers can choose from a wide set of materials and usually do not provide information about their choice. In our simulations a somewhat arbitrary value of $\lambda_{\text{binder}} = 20\,\text{cm}$ was chosen, independent on the exact wavelength. Thus the binder material is effectively transparent to the scintillation light.

The simulation results are shown in Figure 5.9 and summarized in Table 5.3, which shows fit parameters of an exponential function fitted to the results shown in the figure. The simulation using the random walk process shows a discernible dependence on the composition of the material. Simulations with a larger ZnS mass ratio show a lower transmission factor, and the table shows that the fitted effective attenuation length decreases with an increasing amount of ZnS:Ag. This is due to the increased fraction of path length spent in ZnS grains, which exhibit the strongest absorption. The trend of higher ZnS ratio leading to worse transmittance can also be guessed from the measurements in Figure 5.8 for thicknesses of 0.3 and 0.4 mm.

The strong surface effects observed in the measurements are captured by neither model. The values of y-intercept of the exponential fits to the measurements in Figure 5.8 of 1.05(14) % and 11.9 % are orders of magnitude smaller than the values obtained in simulations. A reason for this might be a high reflectance of ZnS of about 90 % [37], which are not included in the simulations.

The absolute value of the effective absorbtion length simulated with the random walk model are in the range of 0.14 mm to 0.19 mm, which is about a factor 4 too small for AST and a factor 1.4 too small for ELJ scintillators. Possible reasons for the shortcomings are discussed below.

In order to examine the influence of the ZnS mass fraction ϕ_{ZnS} on the effective attenuation length, further simulations of the random walk model have been conducted with mass ratios ranging from 0.5 to 4.5. For each value, the transmission of scintillator plates of thicknesses ranging from 0.1 mm to 0.9 mm was simulated and the results fitted by an exponential function. The result is shown in Figure 5.10. Over the whole plausible range of ZnS mass ratios from $\phi_{\mathrm{ZnS}} = 1$ to $\phi_{\mathrm{ZnS}} = 4$, the effective attenuation length varies between 0.15 mm and 0.25 mm, which is a significant difference of 40 %. However, if one is considering only $\phi_{\mathrm{ZnS}} \leq 2$ the difference is only about 20 % which might not be resolvable in measurements due to inhomogenities in the scintillators, as was the case with our samples.

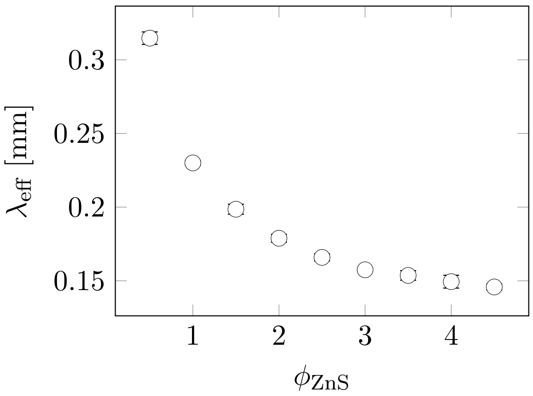

Fig. 5.10: Effective attenuation length obtained from exponential fit to simulations with different scintillator thicknesses for each ZnS mass fraction ϕ_{ZnS}. The simulations use the photon counter module and the scintillator plate, in which the random walk process is used for photon propagation.

The reason for the shorter effective absorption lengths in the simulations might be that

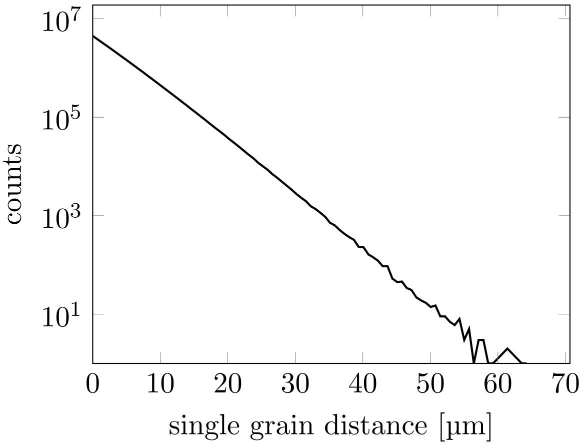

Fig. 5.11: Distribution of distance which a photon travels inside a single virtual grain until it exits again into the binder material.

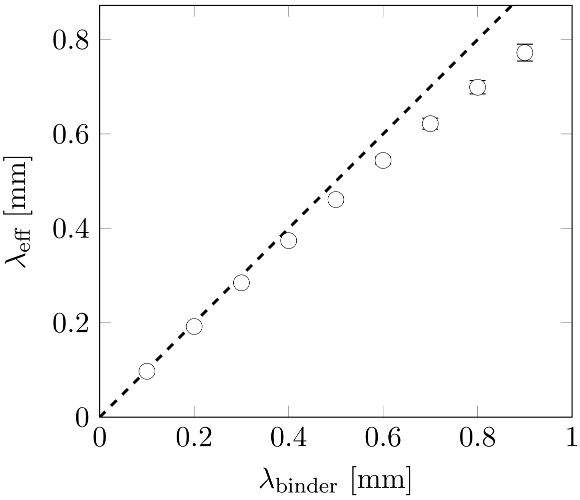

Fig. 5.12: Simulation of the simulated effective optical attenuation length λ_{eff} in dependence on the simulation parameter λ_{binder}. The dashed line is the identity $\lambda_{\text{eff}} = \lambda_{\text{binder}}$.

it happens that photons travel a large distance inside one single grain as Figure 5.11 shows. It happens that a photon travels more than 20 or even 40 µm inside a single grain which is a much longer distance than the mean ZnS grain size of 7.5 µm. This is due to the fact, that the step length proposed by a Geant process is distributed exponentially by default, which means that there is no upper limit to the possible step length. A possibility to improve this behaviour might be to override the `PostStepGetPhysicalInteractionLength()` method with a custom bounded distribution.

The model of an effective attenuation length λ_{binder} for the whole plate material has also been examined in further simulations. Figure 5.12 shows the simulated effective optical attenuation length dependening on the input parameter λ_{binder}. Again, it has been obtained by simulating the transmittance of several different thicknesses for each input and fitting an exponential attenuation function to the result. For small λ_{binder} it closely follows the identity as expected, but for larger values it begins to visibly deviate from the identity. This deviation can be explained by geometric effects. Since the surface is rough, photons are refracted in a random direction upon entry and have a longer travel distance through the material.

In conclusion, this validation measurement revealed some discrepancies between measured effective attenuation length and the one simulated with the random walk process. This might be addressed by further measurements and by improvements of the algorithm. Using an effective attenuation length in the first place gives results as expected, except for a small geometric effect. However, care must be taken when generalizing to unknown compositions, because microscopic parameters probably excert an influence on the effective attenuation length.

Both processes do not show the huge attenuation due to surface effects, which are apparent in the measurements. Because neutron events happen inside the scintillator plate, only effects at the exit surface play a role for the neutron detector. Unfortunately, our measurements do not allow differentiation between contributions from both sides. The effect of the surface where the light enters the plate might be examined by measuring the amount of light backscattered from the scintillator sample in a future measurement.

5.3 Light Intensity Measurements

Experiments conducted in 2010 by Ralf Engels and Jakob Schelten examine the brightness of light flashes of ZnS/LiF scintillators in order to evaluate the usability of different scintillator types in large scale position sensitive neutron detectors [38]. During the measurements pulse heights of different scintillator samples under neutron irradiation were recorded. These measurements can be compared to simulations of the grain box model in order to validate the model of the microscopic structure.

The simulation of the grain box model gives an estimate of the distribution of energy deposition inside ZnS grains. This distribution cannot be compared directly to measured results, because the pulse height spectrum also depends on light attenuation inside the scintillator plate. For the comparison, the propagation of photons was not simulated, but rather calculated analytically by assuming an effective absorption length as described in Section 4.2.1.

The neutron source for the measurements was the Kleinwinkel-Streuanlage at the FRM-II in Munich. The thermal neutrons from the reactor were monochromatized to a wavelength of 4 Å. A PE sample in the beam scattered neutrons isotropically and the targets were mounted behind a boron carbide diaphragm positioned at an angle of 90° of the PE sample. The diaphragm was used to ensure a well-defined neutron flux by absorbing all neutrons not passing through a circular hole, so that the samples are irradiated equally.

For these measurements scintillator samples of AST were used. They were mounted directly between diaphragm and a PMT, which measured the brightness of scintillation pulses. After passing a similar signal processing chain as the signals in the absorption measurements (see Section 5.2), the signal height was digitized in an ADC and binned in a histogram.

The intensity spectrum of scintillation flashes is very broad and overlaps with signals from undesired sources like gamma radiation or thermal fluctuations in the PMT. Because of this it is necessary to filter out most of these background signals via the ADC's threshold, which means that the pulse height spectrum is not recorded entirely and low intensity pulses are cut off.

5.3.1 Expectation

The PMT was not calibrated, so there is no possiblity to obtain the number of photons per event. However, the signal pulse height is proportional to the brightness of the scintillation flash, so there is a proportional connection between the number of photons exiting the scintillator and the PMT's signal strength. Thus, we can expect the spectrum to be like (A.4.5) with an additional proportionality factor for the argument and the overall amplitude. The ADC digitizes the signal strength with a certain accuracy, and counts data in a histogram with discrete channel number $\chi \in \{0, 1, \ldots, \chi_{\max}\}$. To obtain the expectation for the histogram, one therefore needs to integrate the continuous intensity spectrum (A.4.5) over each bin, which means an integration from $\gamma\chi$ to $\gamma(\chi + 1)$, where γ is the proportionality constant between channel number and number of detectable scintillation photons:

$$I(\chi) = k \int\limits_{\gamma\chi}^{\gamma(\chi+1)} dN \; p_N(N) \tag{5.3.1}$$

Here, k is the number of neutron events inside the scintillator plate and $p_N(N)$ is the probability density of N photons exiting the scintillator plate on one side after a neutron event, as calculated in Appendix A.4. Under the assumption that $p_N(N)$ does not change significantly over the bin width, one can approximate the integral with the product of bin width and function value:

$$I(\chi) \approx k \cdot \gamma \cdot p_N(\gamma\chi) \overset{\text{(A.4.5)}}{=} k \cdot \gamma \cdot \int\limits_0^d dx \; \frac{h(x)}{\alpha_l(x) \cdot C} \cdot p_E\left(\frac{\gamma\chi}{\alpha_l(x) \cdot C}\right). \tag{5.3.2}$$

Here, $h(x)$ is the probability distribution of an event happening in depth x given in (A.4.6). $\alpha_l(x)$ is the extinction factor of scintillation light, which describes the fraction of the photons that exit the scintillator after a neutron event at depth x. It is derived in (A.4.3) by geometrical considerations. Since neutron energy, mass ratios and binder density ($1.58\,\mathrm{g\,cm^{-3}}$, see (5.1.6)) are known, it is possible to calculate the neutron's attenuation length λ_n, which is needed in $h(x)$, by combining (5.1.1) and (5.1.3):

$$\lambda_n = \frac{(m_{\mathrm{Li}} + m_{\mathrm{F}}) \cdot \sum \frac{\phi_X}{\rho_X}}{\sigma \cdot \phi_{\mathrm{LiF}}}, \tag{5.3.3}$$

where σ can be obtained from Figure 4.6 and the atomic masses m_{Li} and m_{F} are given in Section 5.1. In this case, it is also possible to calculate k as a fraction of the total number of neutrons K which pass through the scintillator during the measurement:

$$k = \left(1 - e^{-\frac{d}{\lambda_n}}\right) K \tag{5.3.4}$$

K depends on the experimental setup and can be measured. A measurement with a lithium-glass scintillator yielded a rate of 729 000 neutrons in 10 min. All further pulse spectra were obtained in 10 min measurements as well, so we have $K = 729\,000$. The unknown values λ_l and C/γ must be fitted to the data.

5.3.2 Results

ZnS/LiF	d[µm]	λ_l[mm]	C/γ[MeV^{-1}]	χ^2	χ^2_{exp}
2:1	450	0.438(2)	130.5(3)	2460	820
4:1	450	0.328(3)	108.2(4)	1250	1530
4:1	225	0.205(3)	104.4(7)	1600	2280

Tab. 5.4: Fit values for samples shown in Figure 5.13 according to (5.3.2) with the χ^2 values for this fit and the fitted exponential function.

Figure 5.13 shows three measured pulse height spectra of different samples, as well as a fit of (5.3.2), with fit parameters given in Table 5.4. The expectation fits the data very well, and the fit parameter for C/γ seems stable. Even though the fit parameter for λ_l varies by a factor of 2, which seems very large, the tendency that a larger ZnS mass ratio leads to a smaller effective optical attenuation length is consistent with results described in Section 5.2.

The fit parameters for different fits show some inconsistencies. While the value for λ_l shows the expected trend of increasing for decreasing ZnS mass ratio, it should be similar for the two samples where the ZnS mass ratio is identical. The different sample thickness should not have an influence on the optical attenuation length. Further, the value for C/γ should be equal for all three samples. The deviation of 20 % for the 2:1 sample cannot be explained.

Unfortunately the spectra have been cut off just above the point where the fit shows a change in slope. This was probably intentional at the time of the experiment, as the

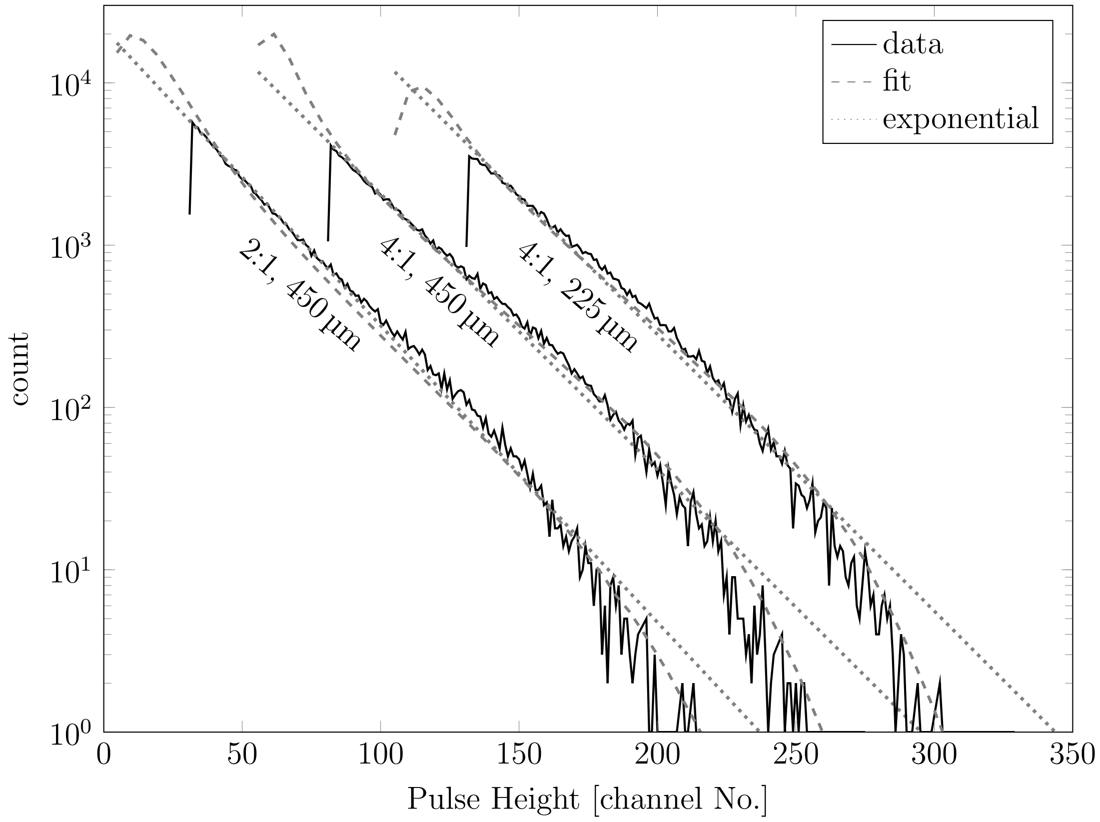

Figure 5.13: Results of light intensity measurements of different scintillator samples irradiated by 4 Å neutrons, with fits according to the expectation in (5.3.2) and an exponential function. The single spectra are offset by 50 channels for better visibility.

increasing slope might be mistaken for the onset of background radiation. The additional information of the slope onset might have improved the fits significantly and yet increased the trust in the validation of the grain box module.

However, in comparison with the exponential fit, the result of our model is a clear improvement at higher channels, where the measured signal starts to decrease faster than exponentially. Our model captures this feature well for the 4:1 samples and to some extent also for the 2:1 sample. The χ^2 values of the model fits are better for the 4:1 samples as well. This shows that the model of the grain structure is able to simulate the distribution of energy in ZnS grains realistically.

5.4 Prototype Measurements

In order to validate the model of the detector system as a whole, measurements of a single detector bank for the SAPHiR instrument as described in Section 2.6 have been compared with simulations of the model in its entirety. The measurements were conducted in 2013 by Ralf Engels at the TREFF reflectometer at FRM-2 reactor in Munich.

As a reflectometer, TREFF is designed to examine larger structures on the nm-scale, like thin films. For this task neutrons with longer wavelengths are better suited. The TREFF instrument uses neutrons with a wavelength of 4.73 Å in order to resolve these larger structures. At this wavelength, the two detector plates of the detector have a combined conversion efficiency of about 98 %.

This value can be obtained by extrapolation of the absorption coefficient of 39.7 % from Table 5.1 for the 2:1 500 µm ELJEN sample at 1.17 Å. Here we have two 500 µm plates instead of one, which translates to an exponential factor of 2 in the transmittance. Since $\mu \overset{(5.1.1)}{\propto} \sigma \propto E^{-1/2} \propto \lambda$, there is an additional exponential factor of 4 because the wavelength of the neutrons at TREFF is 4 times longer than at HEiDi. Thus the conversion efficiency must be $1 - (1 - 0.397)^8 \approx 0.98$.

In order to examine the scintillation detector, several different measurements were conducted, including a reference measurement without neutron irradiation. The spatial resolution of the detector was examined in several measurements with different boron carbide diaphragms. Here we restrict ourselves to the reference measurement as well as one measurement with a 1 mm slit diaphragm at a distance of 10 cm from the detector. This measurement was arbitrarily chosen, since we are mainly interested in the comparability of photon counts and duration of neutron events in this context.

5.4.1 Event Reconstruction Algorithm

The data provided by the PMTs consists of single photon events with timestamp and channel information. Besides signals resulting from neutron events, there are contributions due to gamma radiation and thermal noise in single PMTs. Recognizing single events is only possible, if the time difference between two noise photons is much longer than the time difference between two photons which belong to the same neutron event. In this case neutron events cause several photons to arrive in rapid succession on neighbouring fibers. Thus, events can be recognized by finding clusters of photons close to each other in both layers and by checking for coincidence of two clusters between the layers.

Algorithm 5 describes how clusters can be found in a stream of photon data, where each photon event consists of timestamp, channel and layer information. For each photon it is checked, if this photon fits into any existing cluster in line 5. If it fits to exactly one cluster, it is simply added to this cluster. If it fits to multiple clusters, then those clusters are merged and the photon is added to the resulting single cluster. If none of the existing clusters are fitting, a new cluster is created with the photon as single constituent.

Algorithm 5 Clustering of photons

```
 1: $clusters \leftarrow$ empty list
 2: while there are more photons do
 3:     $p \leftarrow$ next photon
 4:     for all $c$ in $clusters$ do
 5:         if $p$ FITS TO $c$ then                          ▷ algorithm 6
 6:             if $p$ has no cluster yet then
 7:                 put $p$ in $c$
 8:             else
 9:                 remove $c$ from $clusters$
10:                 merge $c$ with cluster of $p$
11:     if $p$ has no cluster yet then
12:         $c \leftarrow$ new cluster containing $p$
13:         add $c$ to $clusters$
```

The question whether or not a photon fits to a cluster is addressed in Algorithm 6. The basic idea is to define the distance between two photons p and q as

$$d(p,q) = \left(\frac{t_p - t_q}{\tau}\right)^2 + \left(\frac{n_p - n_q}{n_c}\right)^2, \tag{5.4.1}$$

where $t_{p/q}$ is the timestamp and $n_{p/q}$ is the channel number of p and q respectively. The constants τ and n_c are parameters of the algorithm. A photon fits to a cluster, if and only if it is from the same layer as other photons of the cluster and its distance to at least one of those photons does not exceed 1. Two photons from the same channel can have a time difference of at most τ in order for them to be part of the same cluster, and photons detected at the same time can be at most n_c channels apart. As a reasonable value for τ, the decay time of the scintillator of about 1 µs [12] should not be exceeded. For n_c a value of 2.5 has been chosen for the following analysis. This way photons separated by two channels can form a cluster, larger differences are forbidden.

As a performance boost, it is possible to define a bounding box for large clusters, which contains the smallest and largest timestamp and channel number of the cluster's photons. A new photon can be compared to these bounds and if it does not fit, it can be rejected before comparing it to every photon already in the cluster.

Algorithm 6 Check if photon fits to cluster

```
Require: $\tau$: maximum duration between clustered photons
Require: $n_c$: maximum channel distance between clustered photons
function $p$ FITS TO $c$ ($p$ is a photon event, $c$ is a cluster)
    $t_p, n_p, l_p \leftarrow$ timestamp, channel and layer of $p$
    for all $q$ in $c$ do
        $t_q, n_q, l_q \leftarrow$ timestamp, channel and layer of $q$
        if $((t_p - t_q)/\tau)^2 + ((n_p - n_q)/n_c)^2 \leq 1$ and $l_p = l_q$ then
            return True
    return False
```

If the photon stream is ordered with respect to photon timestamp, it is possible to rule out very old clusters for new photons. If the newest photon of a cluster is older than $t_p - \tau$ at line 3 in Algorithm 5, no further photon will fit to it and thus it can be removed from *clusters* and stored in a list of finished clusters. Thus, the number of active clusters remains low and the execution time of the for-loop in line 4 does not increase over time. This can always be done offline with sorted data.

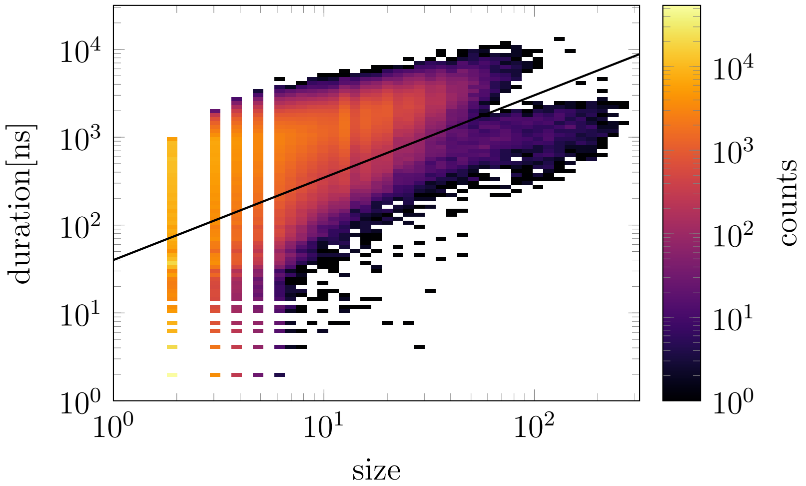

Fig. 5.14: Two dimensional histogram of photon clusters found by Algorithm 5 in the data of a neutron measurement. The histogram plots the duration of a cluster versus its size logarithmically. The black line indicates a possibility to differentiate between fast clusters and slow clusters.

In a scenario where such an algorithm is employed *in situ* during the measurement for data reduction, multiple ADC units collect data parallely, so there might be a delay in the data transfer of one ADC module which leads inversions with respect to time ordering. In that case the condition should be relaxed to finishing clusters if their newest photon is older than $t_p - \alpha\tau$ with $\alpha > 1$ in order to increase the robustness. The finished clusters are not stored, but passed to the coincidence finding algorithm described below.

Figure 5.14 shows the result of the cluster finding algorithm on the data of one measurement. The data was comprised of 8 164 472 sets of timestamp, channel, and layer information for single photons, of which around 34 % were discarded as single-photon clusters. The remaining 66 % were organized into 1 054 285 clusters with an average size of 5 photons per cluster.

The black demarcation line visualizes the differentiation of two distinct types of clusters. Clusters above the line are somewhat smaller and slower. Figure 5.15(a) shows clusters found in the data of the reference measurement with the neutron beam turned off. Both measurements had the same duration, so that it is possible to subtract the reference measurement from the measurement in Figure 5.14. The result is shown in Figure 5.15(b) and clearly shows that neutrons cause the slower kind of clusters, above the demarcation line, and the clusters below it belong to the background.

After the photons have been ordered into clusters, it is possible to match clusters from different layers to form neutron events. To this end, Algorithm 7 first sorts the clusters found by Algorithm 5 in two lists according to their layer and evaluates how well any pair of clusters from different layers scores. This is done using the SCORE-function defined in Algorithm 8, which first checks if the timestamps $t_{1/2}$ of the first photons fall within a coincidence window of $2t_c$. If so, the score is the product of the cluster sizes with the gaussian factor $\exp\left((t_1 - t_2)^2/t_c^2\right)$, otherwise the score is zero. Thus, big clusters close to each other get large scores. t_c should be significantly smaller than the decay time of the scintillator, but not too small since only few photons reach the PMTs, and thus the difference in time stamps may vary significantly due to statistical effects. For the following analysis, a value of $t_c = 200\,\text{ns}$ has been chosen.

Each cluster might be part of multiple pairs. However, one cluster can be counted for only one event, so it is necessary to assign at most one partner to each cluster. In

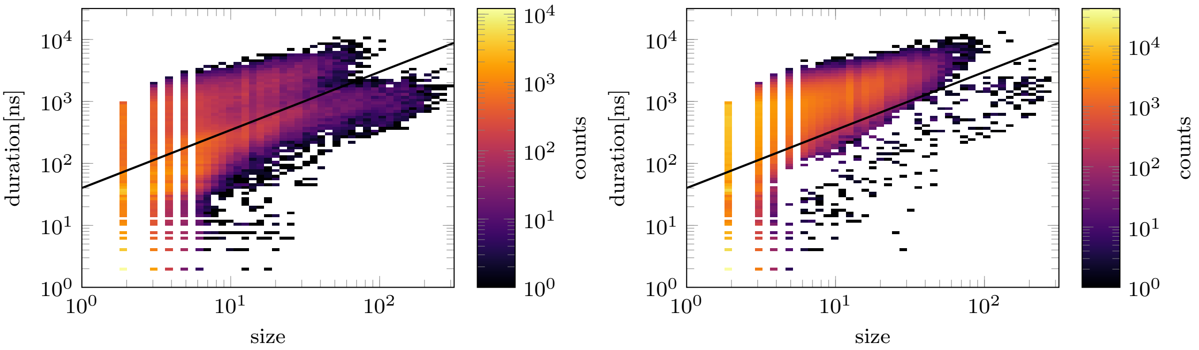

(a) **(b)**

Figure 5.15: Correction of background signals. (a) shows the cluster finding algorithm applied to a measurement without neutron irradiation. In (b) this background has been subtracted from the histogram in figure 5.14.

Algorithm 7 coincidence matching

```
Require: $clusters$ from algorithm 5
Require: $s_m$: minimum score for a pair of cluster
$a_1, a_2 \leftarrow$ clusters from $clusters$ with photons from layer 1/2
$pairs$, $events \leftarrow$ empty lists
for all $c_1$ in $a_1$ do
    for all $c_2$ in $a_2$ do
        $s \leftarrow$ SCORE($c_1, c_2$)                                ▷ algorithm 8
        if $s > s_m$ then
            add $\{s, c_1, c_2\}$ to $pairs$
while $pairs$ is not empty do
    $\{s, c_1, c_2\} \leftarrow$ triple in $pairs$ with largest score $s$
    remove $\{s, c_1, c_2\}$ from $pairs$
    if $c_1$ in $a_1$ and $c_2$ in $a_2$ then    ▷ If one cluster has been removed already, skip the pair
        remove $c_1$ from $a_1$ and $c_2$ from $a_2$
        $x_{1/2} \leftarrow$ average photon channel of cluster $c_{1/2}$
        $t \leftarrow$ earliest timestamp of $c_1$ and $c_2$ combined
        add $\{t, x_1, x_2\}$ to events
```

our algorithm this is done by picking pairs in succession, sorted by their score, with the highest score getting picked first. Thus, large clusters are paired with other large clusters. The idea behind this is that neutron events have varying brightness, and if two events happen at the same time at different positions, they will cause two clusters on each layer. If one neutron event was brighter than the other, it is possible to reconstruct both events correctly by matching the larger clusters and the smaller clusters respectively.

In order to be stored, the score of a pair of clusters needs to be larger than a certain threshold s_m, which prevents the detection of events with too few photons. In the following analysis a value of $s_m = 4$ has been chosen, which requires about 2 photons per cluster with perfect coincidence. If the coincidence is worse, more photons are necessary for the

Algorithm 8 scoring for pairs of clusters

```
Require: $t_c$: coincidence time
function SCORE(cluster $c_1$, cluster $c_2$)
    $t_1, t_2 \leftarrow$ time of earliest photon of $c_1$ and $c_2$
    if $|t_1 - t_2| > 2t_c$ then
        return 0
    $n_1, n_2 \leftarrow$ size of clusters $c_1$ and $c_2$
    return $n_1 n_2 \exp\left(-\frac{(t_1 - t_2)^2}{t_c^2}\right)$
```

score to be registered.

The position of a neutron event can be reconstructed via the channel distribution of its two clusters. The easiest method, which is also used in this work, is to take the average channel number of all photon events of a cluster. Knowledge of the fiber thickness and distance can then be used to estimate the vertical and horizontal position on the scintillator screen. A more elaborate approach might be a gaussian fit to the channel distribution. This way the position of neutrons at the border would be estimated more accurately.

The performance of Algorithm 7 can be increased by sorting clusters by starting time and checking the score only for those clusters which are not further apart than $2t_c$. In order to be applicable in *in situ* analysis, this algorithm needs to be modified as well. As the *in situ* cluster finding algorithm described earlier returns a finished cluster, it needs to be buffered and its score with already buffered clusters needs to be calculated. Then, if the clusters with the currently highest score date back more than $2t_c$ before the oldest unfinished cluster, they can be removed from the buffer and given to the laboratory computer as detected neutron event.

The result of matching clusters from Figure 5.14 is shown in Figure 5.16. The algorithm

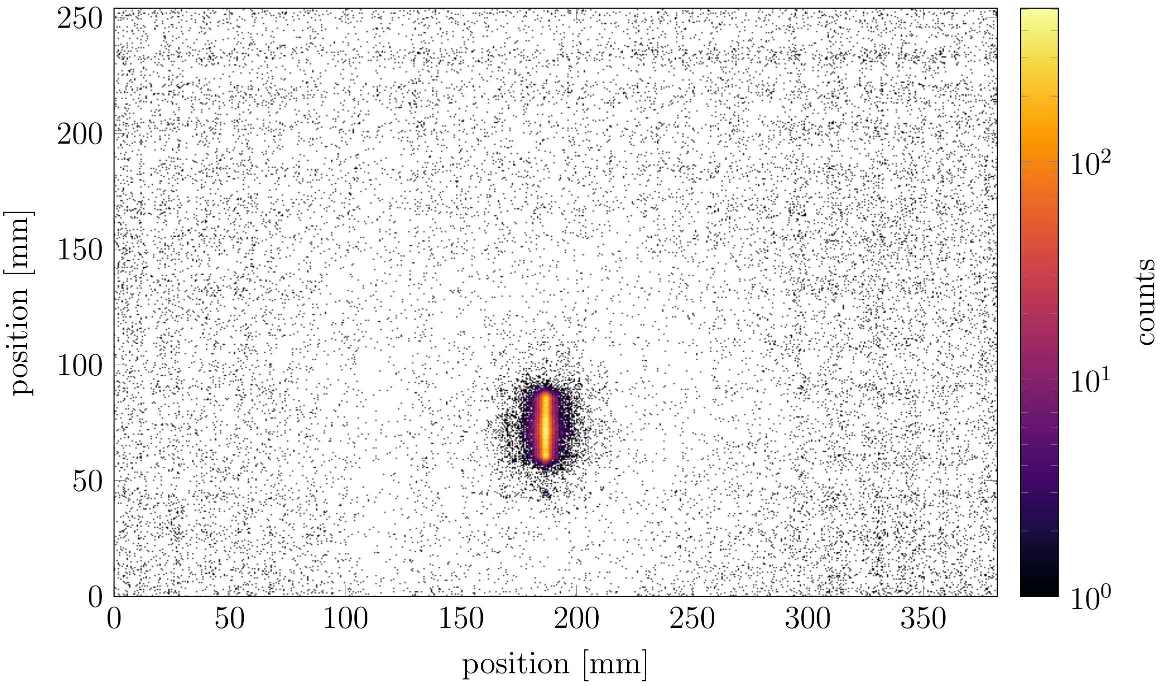

Figure 5.16: Position reconstruction via coincidence matching of clusters as described in Algorithm 7. The underlying data is the same as in Figure 5.14. As the distribution of neutron events suggests, this measurement was conducted with a 1 mm wide slit diaphragm in front of the scintillator plate at a distance of 10 cm.

matched only 129 699 neutron events, leaving 75 % of clusters unmatched. This large rate stems from the fact, that most of the small clusters are not matched, as the analysis of the size of unmatched clusters in Figure 5.17 shows. This rejection mechanism is by design a part of the algorithm. The score function penalizes small clusters and thus it is less probable for them to exceed the score threshold.

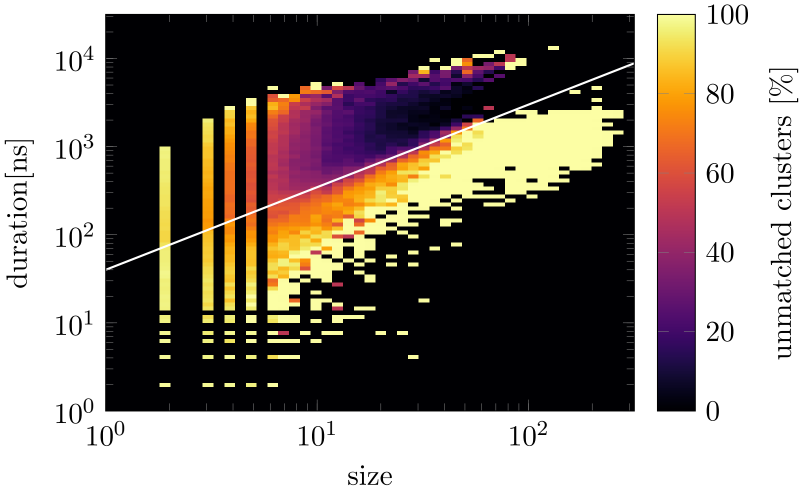

Fig. 5.17: Rate of unmatched clusters depending on cluster size.

The figure reveals another important fact. None of the large clusters below the demarcation line (white in this figure) are matched. Large clusters cannot be rejected due to their size, because a cluster containing 30 or more photons will get a minimum score of $30 \cdot e^{-2} \approx 4.1$, so it will always exceed the threshold if there is a coincident cluster. It follows, that the clusters are unmatched solely because there is no coincidence cluster accompanying them, which means that they did not originate on the scintillator plate. Rather, it may be possible, that they are caused by gamma particles passing through the WLSF bundles directly in front of the MaPMT.

The algorithm described above is capable of finding neutron events reliably when the counting rates are sufficiently small. In particular, it is not capable of differentiating between overlapping events at the same position, i.e. the second neutron arrives before the scintillation flash of the first one fully subsided. A problem arises when the counting rate increases to a point where almost all events overlap. In this case the clustering would fail because all photons would be collected in one single cluster. These difficulties could be addressed by a more intelligent algorithm for fitting photons to clusters. Such an algorithm might reject photons which arrive after a maximum duration for a cluster, or split a cluster when the photon density suddenly increases.

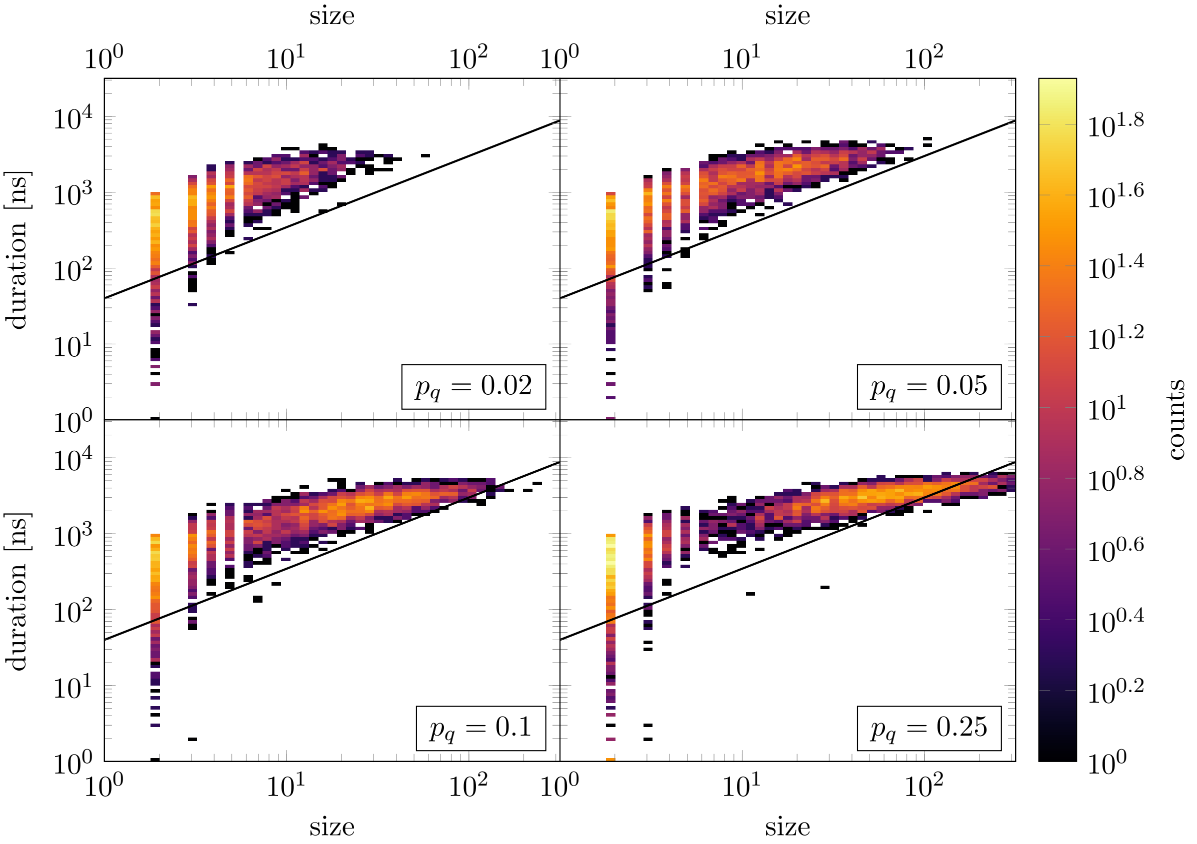

Figure 5.18: Cluster finding Algorithm 5 applied to full simulations of the SAPHiR prototype. Photon events were rejected with probability p_q, which emulates quantum efficiency of the PMTs and further possible losses. The axis ranges and demarcation line are identical to Figure 5.14.

5.4.2 Simulation Results

Figure 5.18 shows simulation results analysed by the same cluster finding algorithm as the measured data in Figure 5.14. The simulation was carried out with parameters resembling the SAPHiR prototype: two ELJEN $392 \times 256 \times 0.5\,\mathrm{mm}^3$ scintillator plates with ZnS/LiF ratio 2:1 sandwiching the multicladded 1 mm WLSFs. A gap of 1 mm between two fibers leads to 128 channels in one direction and 196 in the other. Within the scope of this work, this validation is the first one including the creation of scintillation photons. The default scintillation efficiency was obtained by comparison of grain box simulations to literature, as described in Section 7.4. Also, the matching effective optical attenuation length of $\lambda_{\mathrm{binder}} = 0.4\,\mathrm{mm}$ was used.

The PMT efficiency p_q was set to one during the simulation and only reduced during analysis via rejection of photon events with probability $p_q < 1$. The four panels of Figure 5.18 show results for $p_q = 0.02$, 0.05, 0.1 and 0.25. The photo cathodes of the

PMTs usually have a quantum efficiency of about 25 %, but the resulting histogram for $p_q = 0.25$ shows significant deviation from the measured result in Figure 5.15(b). It shows an accumulation of photon clusters around a size of 70 photons and a duration of 3 µs. These clusters are detached from an accumulation of clusters of two or three photons on the left of the panel, which occur when some photons arrive later than τ after a previous photon in the same event.

For smaller efficiencies the separation is reduced and eventually vanishes for $p_q = 0.05$. The reason for this is simply that less photon events are accepeted and thus the clusters get smaller. However, the number of small clusters also decreases, because the probability that two or more late photons arrive together within a time of τ decreases when there are fewer photons.

The panel with $p_q = 0.05$ already shows a good conformity with the measurements. Except for very small ones, all clusters lie above the demarcation line and the distributions are similarly shaped. However, in Figure 5.15(b) the counting rate per bin decreases from about 1000 for clusters of size 10 to 10 for clusters of size 100, which is three orders of magnitude. In the $p_q = 0.05$ simulation the difference is only one order of magnitude, which is why a still smaller efficiency might better fit the data.

This means that the simulation registers many more photons than the measurement. A potential reason for this might be that the scintillation efficiency was chosen too high (which is a concern, see Section 7.4), or that there is another source of attenuation not regarded so far. One source might be surface effects discussed in Section 5.2.2, where some photons are scattered, absorbed or reflected at the surface of the scintillator plate. Photons guided along the fiber might also be scattered at defects created when bending the fiber. This degradation is reduced by bending the fibers in a warm water bath, but it cannot be prevented completely. These effects are not captured by the simulation and might be examined by comparing measurements of the whole detector with different scintillator compositions.

5.4.3 Optical Attenuation in Outermost Cladding

A further source for photon loss might be the optical attenuation in the outermost fiber cladding. If it is very strong, scintillation photons may be absorbed in the cladding before reaching the core. Then they would be lost for the wavelength shifting and thus less photons would arrive at the PMTs. The default attenuation length $\lambda_c = 5\,\text{mm}$ used in the simulation is a maximum value for which a fiber of about 30 cm length is still well defined. It may be shorter in the fibers used for the prototype.

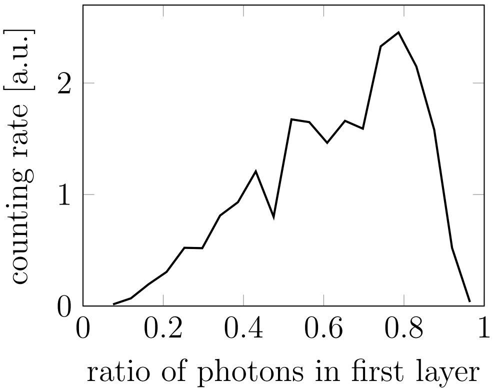

Fig. 5.19: Normalized distribution of the fraction of photons counted in the WLSF layer closer to the neutron source. The histogram uses the data of the slit diaphragm measurement and bins the quotient of the size of the photon cluster from the first layer and the sum of both clusters.

λ_c not only influences the total amount of photons, but also the ratio between photons in both layers. If λ_c is short, more photons will be absorbed in the cladding of the nearer layer and thus less photons are available to be shifted in the second layer. Although the prototype contains two scintillator plates sandwiching the WLSFs, 87 % of the 4 Å neutrons are converted in the first plate. So, for most events the WLSF layer closer to the neutron source is the near layer.

To examine the distribution of the ratio of photons, event data of the slit diaphragm measurement is analysed again. For each neutron event found by Algorithm 7 the size of the cluster from the first layer divided by the overall size of the event was determined and the result binned in a histogram. The result is shown in Figure 5.19. The distribution shows a strong bias towards the first layer, with a peak at a ratio of about 80 %. There is a small dip for a ratio of 50 %, however, this may be due to statistical fluctuations.

The same analysis with simulated data with different values for λ_c is shown in Figure 5.20. For these simulations an efficiency factor of $p_c = 25\,\%$ was chosen, otherwise the parameters are identical to the simulation presented in Figure 5.18.

Longer attenuation lengths show a very high peak at smaller ratios of about 60 %. At this attenuation length the cladding absorbs almost none of the perpendicularly incident scintillation photons. With a fiber thickness of $d_f = 1\,\text{mm}$, the cladding has a thickness of 15 µm. Travelling such a distance, an attenuation length of 1 mm or even 10 mm does not lead to absorption of more than two percents. This is why the absorption in the first layer is only due to absorption in the dyed core of the WLSF. Because of the good transparency of the outer cladding, many photons reach the core, and statistical fluctuations are minimal. This explains the narrowness of the peak for large λ_c. There is even a second peak visible at a ratio of about 40 %, which indicates neutron events in the second scintillator plate.

For smaller attenuation lengths, the photon absorption in the cladding increases. $\lambda_c = 0.1\,\text{mm}$ leads to 14 % absorption of perpendicular photons, for $\lambda_c = 0.01\,\text{mm}$ it is 78 %. The higher absorption leads to a smaller ratio of photons reaching the second layer, because the probability that a photon passes a fiber without interaction decreases.

Thus, only photon paths through the gap between two fibers of the first layer remain unobstructed. This leads to an increase of the peak ratio for shorter λ_c. Since more photons are absorbed in the cladding, less photons can contribute to the shifting process, such that statistical fluctuations become stronger. This leads to a broadening of the peak.

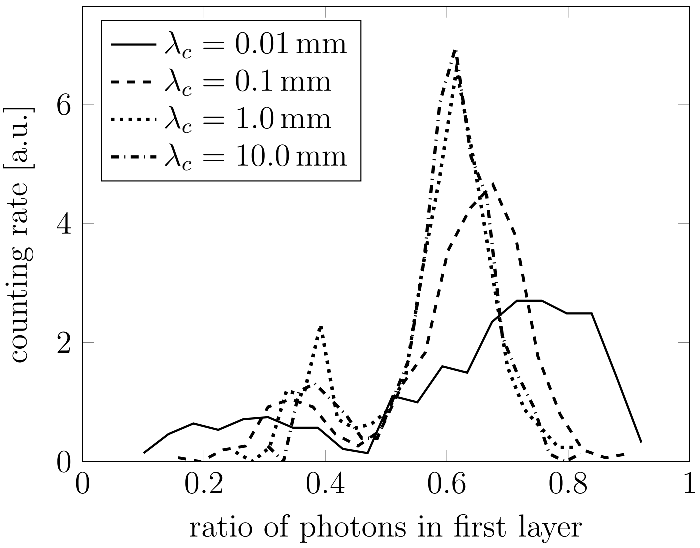

Fig. 5.20: Normalized distribution of the fraction of photons in the first WLSF layer according to simulations with different optical attenuation lengths λ_c in the outer cladding.

Comparing the simulation results with the measurement, an attenuation length of $\lambda_c = 0.01\,\mathrm{mm}$ shows the closest resemblance. Since both figures are normalized to an integral of one, the peak height can be compared and is of the same order of magnitude. The peak position at 80 % matches as well. The absorption factor of 78 % reduces the photon detection efficiency by a factor of 22 %. In combination with a quantum efficiency of 25 %, this results in a total efficiency of 5.5 %, a value similar to $p_q = 0.05$, which shows good agreement between simulations and measurement in Figure 5.18. However, as discussed earlier, this value might still be too high, so the other sources of attenuation already mentioned must be considered as well.

In conclusion, the validation of the model has been mostly successful. With a clustering event reconstruction algorithm, the distribution of cluster size and cluster duration could be reproduced using a fairly small photon detection efficiency. This small efficiency could be explained by a short attenuation length in the outer fiber cladding of the WLSFs.

Chapter 6

Optimization

One aim of this work is the development of an optimization algorithm for the parameters of the model. The parameters should be optimized with respect to detection efficiency and/or position resolution. These detector characteristics can be obtained by the simulation of several neutron events in the full detector model. For the detection of a neutron event, for instance, a certain number of photons need to be detected in each WLSF layer. Thus, the value to be optimized would be the fraction of simulated events in which enough photons reach the PMTs. Naturally, the number of photons required depends on the detection algorithm employed for the detector.

Because possible optimization functions depend on simulation results, it is not possible to calculate the gradient analytically in order to use it for steepest decent methods. Calculating the gradient numerically would require a huge effort, because the change of the function value under a very small change of the parameters is dominated by statistical fluctuations. Therefore, a numerical gradient obtained with insufficient data is meaningless.

In cases where the gradient is unavailable and properties of the optimization function are not known, commonly employed optimization algorithms are genetic or evolutionary algorithms [39]. These imitate the biological process of evolution in that a population of random solutions creates offspring via reproduction, mutation and recombination of parameters. Better solutions, i.e. solutions where the optimization function has a higher yield, exert a larger influence on the new offspring, so that bad solutions fade out. This way the population of solutions converges towards an optimum.

However, a population of such an algorithm should be of substantial size in order for the recombination of the fittest to yield enough diversity. To determine the fitness of each solution, several hundred events have to be simulated. This adds up to a very long simulation time for only one generation.

Another popular optimization algortithm for such problems is called simulated annealing [40]. This algorithm simulates a random walk of a particle in the parameter space with an optimization function as potential. A random step is always accepted if it improves the optimization function. Otherwise it is accepted with the probability $\exp\left(-\Delta f/T_t\right)$, where Δf is the change of the function value between steps and T_t is called the system temperature at the time of the step. If the temperature is high, the probability of acceptance is high even for steps which lower the function value. Thus, the algorithm avoids getting stuck in local optima. The temperature is lowered slowly as the random walk proceeds, which results in unfavourable regions being avoided. When the temperature eventually reaches zero, the algorithm only accepts steps which improve the function value, and therefore finds the current local optimum which usually is also the global optimum if the parameters of the algorithm are suitable.

This algorithm also requires many function evaluations, because it should be possible for the random walk to reach the whole parameter space at each temperature setting. Otherwise, if the temperature is decreased too rapidly, there is a probability of finding a local optimum only. Also, this algorithm compares function values between small steps of parameters, which is heavily influenced by statistical fluctuations as discussed earlier. This is why this algorithm is also ill suited to our problem.

6.1 Multi Dimensional Golden Section Search

The algorithm chosen for our task is a multi dimensional generalization of the Golden Section Search (GSS). The one dimensional variant is one of the fastest optimization algorithms which do not use a derivative (like e.g. the Newton method). As counterpart to the bisection method for finding roots, the GSS divides a search interval and excludes part of it in each iteration.

In order to find the maximum of a function $f(x)$ on the interval $x \in [a, b] \subset \mathbb{R}$ with GSS, f needs to be *unimodal* on this interval, i.e. it is monotonically increasing between a and the maximum and monotonically decreasing between the maximum and b. If this is the case, we can choose any two points x_1, x_2 such that $a < x_1 < x_2 < b$ and compare the function values at these points. If $f(x_1) < f(x_2)$, then f must be monotonically increasing up to at least x_1, so the optimum surely lies between x_1 and b. Otherwise, if $f(x_1) > f(x_2)$, the optimum must lie between a and x_2. This way it is possible to narrow the interval by successive function evaluations.

In order to minimize the number of iterations, the choice of x_1 and x_2 should be symmetrical, so that the length of the interval which can be excluded is the same regardless of which function value is greater. If we choose

$$x_{1/2} = \frac{a+b}{2} \pm \xi \cdot \frac{a-b}{2}, \qquad 0 < \xi < 1 \tag{6.1.1}$$

the interval is reduced by a factor of $\frac{1}{2}(1+\xi)$. In order to minimize this factor one needs to choose an ξ close to zero. However, if the function evaluation is costly, this is not the fastest solution, because during every iteration two function values have to be calculated. Since the point with larger function value lies inside the new interval, it is possible to choose ξ such that this point is used again, so that only one new function evaluation has to be made per iteration. Without loss of generality, let us assume, that $f(x_1) > f(x_2)$ so that the new interval is $[a, x_2]$. Then we want x_1 to be equal to the greater of the new evaluation points:

$$x_1 = \frac{a+x_2}{2} - \xi \cdot \frac{a-x_2}{2} \qquad \Rightarrow \qquad \xi^2 + 4\xi - 1 = 0 \qquad \Rightarrow \qquad \xi_{1/2} = -2 \pm \sqrt{5} \tag{6.1.2}$$

The negative solution is discarded, since (6.1.1) requires ξ to be positive, so we have $\xi = \sqrt{5} - 2 \approx 0.236$. The reduction factor per iteration is then $\frac{1}{2}(\sqrt{5}-1) \approx 0.618$, which is the golden ratio ϕ and the namesake for this algorithm. Since one of the function values can be reused, the golden ratio is also the reduction factor per function evaluation. In the case of a very small ξ two function evaluations are necessary per iteration, so the reduction factor per function evaluation is always greater than $\sqrt{0.5} \approx 0.707$.

To show the unimodality of a function is often a difficult task. However, if the function is differentiable and the derivative has finitely many roots, the algorithm still converges towards some local maximum or towards the boundary of the initial interval, even if the function is not unimodal.

A multi dimensional generalization is given in [41] and is summarized in Algorithm 9. The parameter space is generalized to a hyper-cuboid defined by the product of allowed parameter intervals which are successively narrowed during iterations. In the algorithm two vectors $\vec{p}$ and $\vec{q}$ are used to keep track of upper and lower bounds of each parameter. There are 2^n points of function evaluations, where n is the number of parameters or the dimensionality of the optimization problem. The points are determined by starting from the center of the hyper-cuboid and moving towards its corners by a fraction of ξ. In line 6 of the algorithm the displacements from the center are calculated component-wise from binary direction vectors $\vec{s} \in \{-1, 1\}^n$.

Algorithm 9 Multi dimensional GSS

```
Require: $n$: number of parameters (dimensionality of optimization problem)
Require: $\vec{b}_{\max} \in \mathbb{R}^n$: upper bounds of parameters
Require: $\vec{b}_{\min} \in \mathbb{R}^n$: lower bounds of parameters
Require: $\varepsilon$: relative required accuracy
Require: $\xi$: excentricity of function evaluation points
$\vec{p} \leftarrow \vec{b}^{\max}$
$\vec{q} \leftarrow \vec{b}^{\min}$
while $|\vec{p} - \vec{q}|^2 < \varepsilon^2 \left|\vec{b}_{\max} - \vec{b}_{\min}\right|^2$ do
    $max \leftarrow -\infty$
    for all $\vec{s} \in \{-1, 1\}^n$ do
        $u_i \leftarrow s_i \frac{\xi}{2}(p_i - q_i)$, for $i \in \{1, \dots, n\}$
        $\vec{r} \leftarrow \frac{1}{2}(\vec{p} + \vec{q}) + \vec{u}$
        $f \leftarrow$ FUNCTION_VALUE($\vec{r}$)                    ▷ see 10
        if $f > max$ then
            $max \leftarrow f$
            $\vec{u}^{\max} \leftarrow \vec{u}$
    for all $i \in \{1, \dots, n\}$ do
        if $u_i^{\max} > 0$ then
            $q_i \leftarrow \frac{1}{2}(p_i + q_i) - u_i^{\max}$
        else
            $p_i \leftarrow \frac{1}{2}(p_i + q_i) - u_i^{\max}$
Result: value and error of $i$th parameter: $\frac{1}{2}(p_i + q_i) \pm \frac{1}{2}(p_i - q_i)$ for $i \in \{1, \dots, n\}$
```

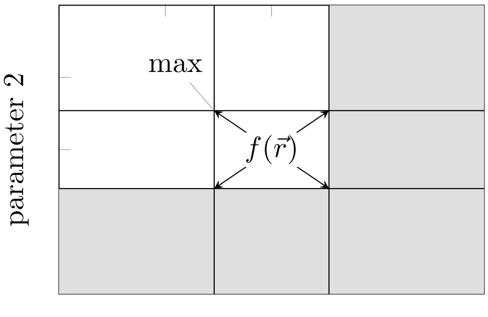

Fig. 6.1: Schema of multi dimensional GSS in two dimensions. The function is evaluated at the four crossing points. If the maximum is for example found at the upper left point, the gray area is excluded for the next iteration.

After evaluating the function, the parameter space needs to be restricted depending on the point with the maximal function value. As shown schematically in Figure 6.1, each parameter interval $[q_i, p_i]$ is cut off beyond the ith component of the evaluation point opposite to the maximum. Thus, the parameter volume is reduced by a factor of $(\frac{1}{2}(1 + \xi))^n$ at each iteration. If ξ is chosen as in the one dimensional golden section search, it is again possible to reuse the function evaluation result of the maximum in the next iteration and one evaluation is saved. It follows, that for this special case the volume reduction per function evaluation is $\phi^{\frac{n}{2^n - 1}}$ instead of $(\frac{1}{2}(1 + \xi))^{\frac{n}{2^n}}$ in any other case. While this is an advantage in the one dimensional

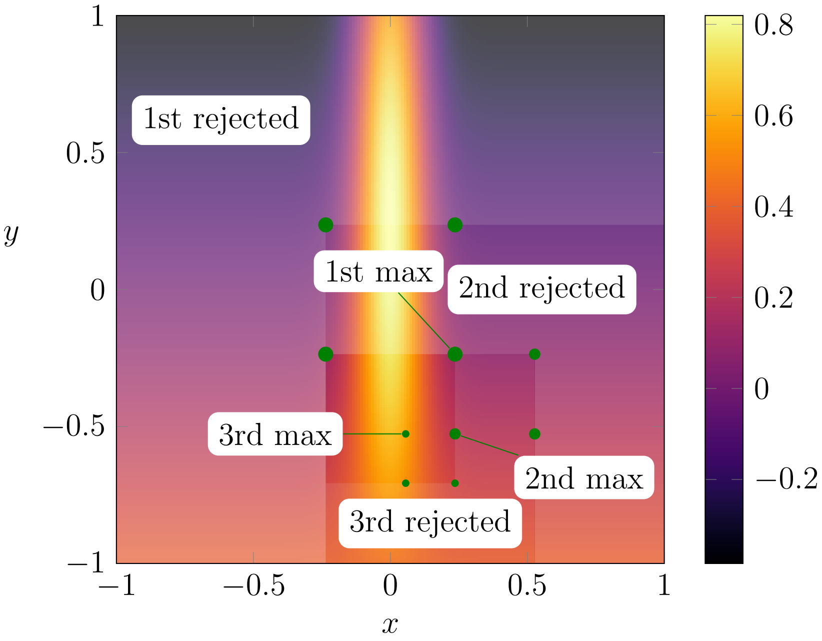

Figure 6.2: Example of a non-unimodal function, where the two dimensional GSS cannot find the maximum of (6.1.3) and does not converge towards the border.

GSS, for $n \geq 2$ the reduction factor for the golden section is larger than the one for very small ξ. However, with very small ξ the distances between function evaluations are very small, which is a problem as described above. For larger values of ξ, the advantage of the resuable function value persits, which is why the GSS was chosen despite not being the optimal method in general.

The requirement of unimodality is more strict in the multi dimensional case, because it is possible to construct non-unimodal functions for which the multi dimensional GSS does not terminate at a local maximum or at the initial boundary. An example of such a function is shown in Figure 6.2, where the first three GSS iterations on the function

$$f(x, y) = \exp\left(-(7x)^2 - \left(y - \frac{2}{3}\right)^2\right) - \frac{5}{13}y \tag{6.1.3}$$

for x and y between -1 and 1 is shown. The maximum is excluded in the second iteration, and the algorithm converges on $(0.2 - \sqrt{5})^T$, which is neither a local maximum nor a point on the initial boundary.

However, this kind of behaviour does not only depend on the function itself, but also on the starting parameters. Note that the function parameters had to be tuned with respect to the points of initial function evaluation in order to fool the algorithm. An initial parameter space only slightly smaller would have led to the maximum being found.

An indication for such an error is, when the final result of the algorithm lies on the boundary of an early iteration. If unimodality of the function is not certain, the validity of the result needs to be checked by performing a further GSS around the alleged maximum. If the second GSS gives some other, better result, the first solution was probably not a local maximum. Of course, if the second GSS also shows convergence to an early boundary, its result needs to be checked again.

6.2 Calculation of Function Values

One of the challenges of the optimization is the dependence of the function value on costly simulations, which entails statistical fluctuations. In order to hold the number of simulation runs as low as possible, a measure has to be developed by which an algorithm can decide if further simulations for a certain set of parameters is necessary.

As a precursor to a more complete detection efficiency function, consider Figure 6.3 showing the distribution of energy deposited in ZnS grains obtained via simulations of the grain box. Since the reconstruction algorithm needs a certain amount of photons in order to detect an event, there is a threshold below which an event is undetectable. This threshold can be translated to a threshold of minimal energy to be deposited in ZnS grains. Thus, a rough estimate for the detection efficiency can be given by integrating the number of events in which the deposited energy is sufficient and multiplying it with the neutron conversion efficiency of the scintillator plate.

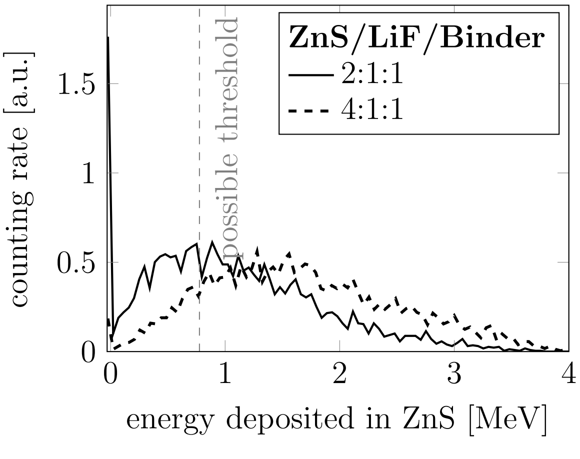

Fig. 6.3: Distribution of energy deposited in ZnS grains. If one assumes a threshold of energy needed to produce enough photons for the neutron to be detected, the efficiency is the area under the curves to the right of the threshold.

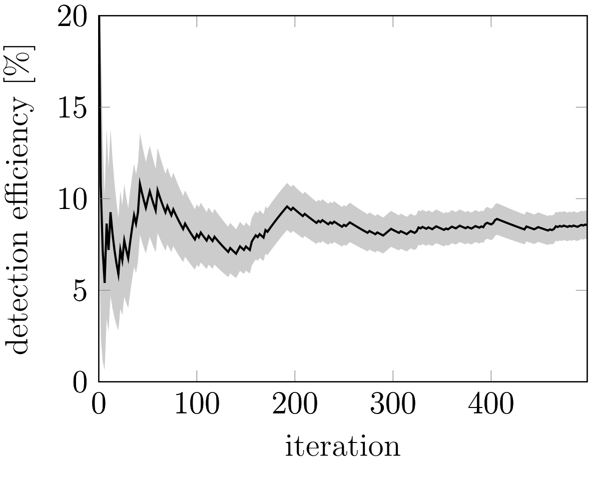

Fig. 6.4: Development of value and error of mock-detection efficiency with the number of iterations.

Algorithm 10 Calculation of function value at $\vec{r}$

```
Require: $m$: number of events per simulation run
Require: $L$: integral length
Require: $f(\vec{r}, \Sigma)$: function to be optimized, where $\Sigma$ is simulation data
Require: $e(\vec{r}, \Sigma)$: error of $f(\vec{r}, \Sigma)$
Require: $\alpha$: error factor
function FUNCTION_VALUE($\vec{r}$)
    $\Sigma \leftarrow$ initial state without simulation data
    $C \leftarrow$ empty list
    $n, k \leftarrow 0$
    repeat
        simulate $m$ events and add results to $\Sigma$
        add $f(\vec{r}, \Sigma)$ to $C$
        $k \leftarrow k + 1$                                ▷ Number of iterations
        if $k > L$ then
            $s \leftarrow \frac{1}{L} \sum_{i=k-L}^{L} (C[i] - C[i-1])^2$
            if $s > (\alpha \cdot e(\vec{r}, \Sigma))^2$ then
                $n \leftarrow 0$
            else
                $n \leftarrow n + 1$          ▷ Number of consecutive iterations below threshold
    until $n > L$
    return $f(\vec{r}, \Sigma)$
```

Given an arbitrary threshold of 1 MeV, Figure 6.4 shows the development of efficiency value and its statistical error with the accumulation of simulation data. The value seems to be leveled out after about 300 simulation runs, but it is actually steadily increasing until there is a noticable kink after the 400th iteration. Thus, it is advisable to continue the simulation to collect more data. During the optimization process the decision whether or not to continue needs to be made automatically by a suited algorithm.

The final function value is reached when there is little change if more data is taken into account. This can be checked by comparing the function value before and after a simulation run. However, statistical fluctuations allow for those function evaluations to be similar by chance. To have a robust check, the differences induced by many consecutive runs should be taken into account. Since a change can be positive or negative, the average of squares of the changes can be used as a measure for the evenness of the function. The error of the function can serve as a value to compare against. However, the average change should be much smaller than the error.

Algorithm 10 shows how a function value is calculated during our optimization process.

It requires the definition of the integral length L, which is the number of change values that are summed up after a new simulation run finished. In order to be able to sum them up, function values are stored in a list C in line 7. For each parameter set $\vec{r}$ at least $L+1$ runs with m events are simulated, so that there are at least L function differences available for the sum. Starting from the $(L+1)$th run, the average square change s is computed in line 10 and compared to the square of the function error multiplied by a factor $\alpha \ll 1$.

If s is smaller, the algorithm does not directly terminate. It rather requires L consecutive checks to succeed in that manner. Only if that happens, the function terminates and returns the function value containing all simulation data.

6.3 Example Optimization Function

The precursor function introduced in the previous section can be extended to take into account the thickness of the scintillator by choosing a threshold dependent on it. Assuming that the WLSFs need a certain amount of light and that the transmittance of light inside

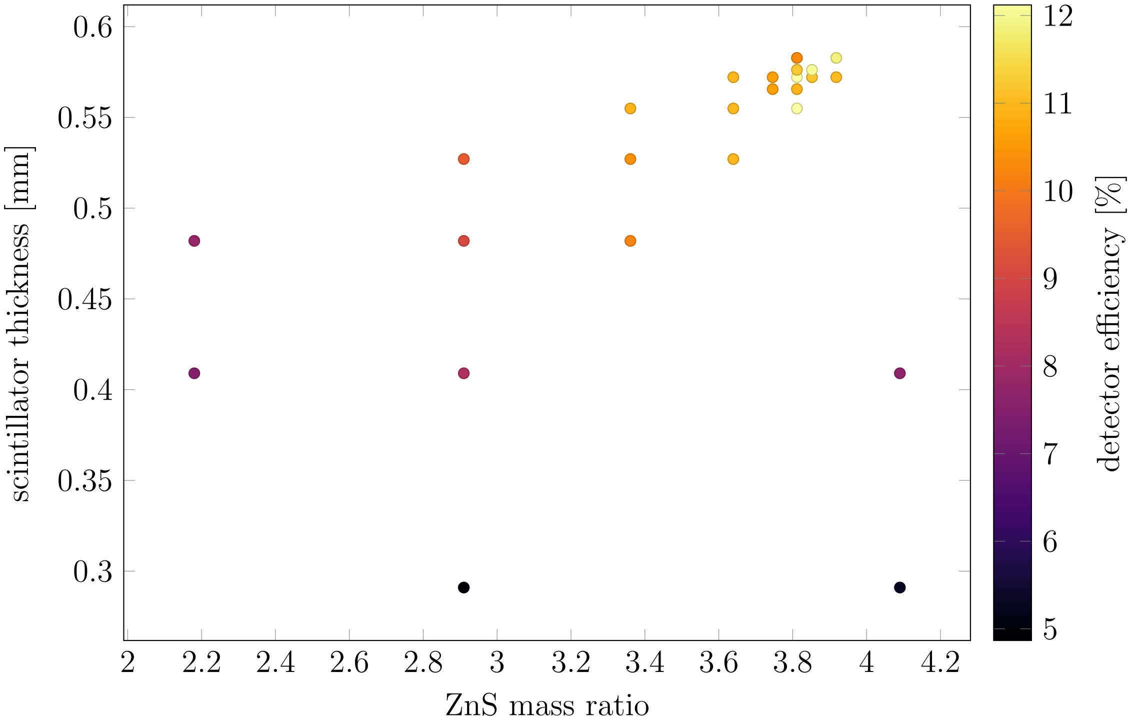

Figure 6.5: Function evaluations during a GSS of the precursor function defined in this section with color coded function values. The mass ratio ϕ_{ZnS} was restricted to $1-6$ and the thickness d to $0.1-0.6$ mm. GSS-result: $\phi_{\mathrm{ZnS}} = 3.83(9), d = 0.574(9)$ mm with a detection efficiency of 12 %.

the scintillator plate is governed by $\alpha_l(x)$ defined in (A.4.3), one can define the threshold as

$$E_c(d) = E_c^0 \, \frac{\int_0^d dx \; h(x)}{\int_0^d dx \; h(x) \cdot \alpha_l(x)}, \tag{6.3.1}$$

where d is the scintillator thickness, E_c^0 the energy required to create the amount of light needed by the WLSFs, and $h(x)$ the probability for a neutron event happening at depth x defined by (A.4.6). The neutron attenuation length λ_n, which is needed for the definition of $h(x)$ and the neutron conversion efficiency of the scintillator plate, can be calculated as $(\sigma\eta_{\mathrm{Li}})^{-1}$, where σ is the neutron capture cross section of ^{6}Li and η_{Li} is its nucleus density defined by (5.1.3). η_{Li} depends on the mass ratios, so the composition will not only influence the function through the simulation of energy deposition, but also through a change in $h(x)$.

The function is defined by counting all grain box events, in which more than $E_c(d)$ is deposited in ZnS grains, dividing it by the total number of events and multiplying it by the neutron conversion efficiency $1 - \exp(-d/\lambda_n)$. An estimate for the error is the square root of the count multiplied by the same factors.

Figure 6.5 shows a GSS of the maximum of this function with scintillator thickness $0.1\,\mathrm{mm} < d < 0.6\,\mathrm{mm}$ and ZnS mass ratio $1 < \phi_{\mathrm{ZnS}} < 6$ as parameters, and the arbitrary choice $E_c^0 = 0.2\,\mathrm{MeV}$. The GSS finds the maximum at $\phi_{\mathrm{ZnS}} = 3.83(9)$ and $d = 0.574(9)\,\mathrm{mm}$.

The algorithm shows a reliable increase in the function value for consecutive GSS iterations until the point where the difference in mass ratio becomes about 0.1. At these parameter distances the statistical fluctuations mentioned earlier in this chapter begin to dominate the variation of function values. It would require much more data in order to reliably compare function values that close to each other. However, this is not necessary for optimizing the detector. Scintillator plates are usually not manufactured with several digits of precision in their parameters. Thus, a rough estimate of the maximum is sufficient.

The error returned by the algorithm depends entirely on the required accuracy ε. This may lead to unreasonable error estimations for very small ε because the algorithm does not yet detect the strength of statistical fluctuations. As an improvement, the algorithm could check for function values which strongly deviate from an interpolation estimate of already calculated values and in such a case either terminate or increase the statistical requirements for function values.

In this example it might be advisable to check the validity of the result by performing a further GSS around the maximum found in the first iteration. However, since this is only a proof of concept, it has not been done.

Chapter 7

Further Simulation Results

7.1 Refractive Index of Binder Material in Random Walk Process

The refractive index n_{binder} of the binder material is an unknown parameter of the random walk model for photon propagation and had to be guessed in Section 5.2. Since it is unknown it might possibly be used as a fit parameter for the model. To test this, optical simulations with different values for n_{binder} have been carried out. For each value of n_{binder} several scintillator thicknesses d were simulated in order to determine the effective absorption length of the model via exponential fit.

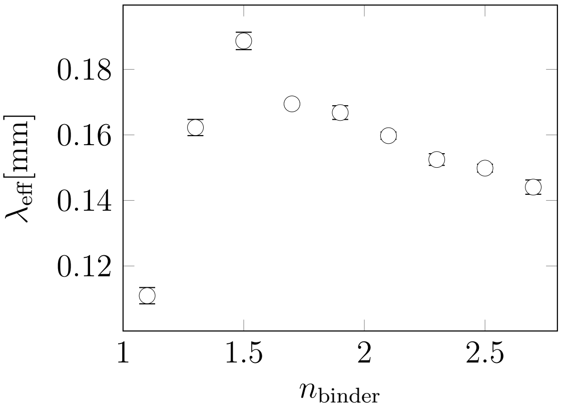

Fig. 7.1: Effective optical absorption length λ_{eff} of the scintillator plate depending on the binder refractive index n_{binder}. For each value of n_{binder}, the optical transmission was simulated for several scintillator thicknesses, and an exponential attenuation law was fitted to the results. The error bars indicate the confidence of the fit.

These simulations used only the scintillator and photon counter modules. Primary particles were 10 000 optical photons with wavelengths sampled according to the LED spectrum shown in Figure 5.5. The binder material was chosen to have an optical attenuation length of $\lambda_{\text{binder}} = 20\,\text{cm}$ and a density of $\rho_{\text{binder}} = 1.58\,\text{g}\,\text{cm}^{-3}$, which is the AST binder density determined in Section 5.1.

Figure 7.1 shows the fit results to our simulations. While the fitted effective attenuation length does depend on n_{binder}, the range of plausible values is $1.3 \lesssim n_{\text{binder}} \lesssim 2.2$

in which the effective attenuation length varies between 0.11 mm and 0.19 mm. Furthermore, the attenuation length seems to have a maximum of about 0.19 mm for $n_{\mathrm{binder}} \approx 1.4$, which is the default value used in the other simulations. This maximum is close to the measured value for ELJ scintillators, but there were not enough statistics in the measurements of ELJ samples for it to give a reliable value. The much more reliable value for AST scintillators, $\lambda_l = 0.66(18)\,\mathrm{mm}$ (see Section 5.2), is outside this range. Therefore, variation of the refractive index of the binder material cannot explain the deviation between measurements and simulations of the random walk model.

A reason for the maximum might be the optical similarity between binder material and LiF grains ($n_{\mathrm{LiF}} = 1.4$ at 450 nm [14]). If $n_{\mathrm{binder}} = n_{\mathrm{LiF}}$, the probability for reflection at a binder/LiF boundary vanishes and the deflection angle upon "refraction" is zero. Thus, the only light scattering component remaining is ZnS. With less scattering events, average path lengths are shorter, and the effective attenuation length increases. This suggests that a binder material should be chosen with a refractive index as close as possible to the refractive index of LiF.

7.2 Variation of Grain Sizes

As mentioned in Chapter 4, the variation of the grain size of ZnS has already been examined in [4]. However, the placement of LiF grains was not included in that model. Therefore, starting points for alpha and triton pairs close to ZnS grains were more likely than when considering the placement of a LiF grain first and placing alpha and triton anywhere in it. For LiF grain sizes much smaller than the alpha particle's range this effect is not significant. However, typical grain sizes of LiF are of the order of 2 µm to 3 µm, which is about half of the alpha's range of about 5 µm [16].

Figure 7.2 shows the dependence of the average energy deposited in ZnS grains per neutron event on the grain size of both grain types. While there exists a clear dependence on both grain sizes, the influence is rather small. Varying one of the grain sizes between 3 and 9 µm while keeping the other one constant results in changes of about 10 % to 20 %. Lower ZnS grain sizes were not examined due to the cubic dependence of the number of grains on the inverse grain size and finding a valid placement for a large number of grains is computationally expensive. The number of grains can be reduced by decreasing the width and height of the grain box, but alpha and triton particles might get deflected laterally and leave the grain box if it is too small.

Since the grain size of LiF is taken into account only for one sphere around the origin, it is no problem to examine the behaviour for small LiF grain sizes. Figure 7.3 shows

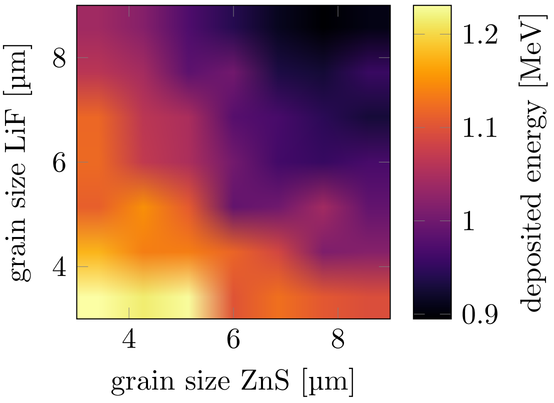

Fig. 7.2: Average amount of energy deposited in ZnS grains for different grain sizes of ZnS and LiF grains. Results were obtained from simulations of the grain box module with ZnS/LiF ratio 2:1. For each point on a 1 µm × 1 µm grid 1000 events were simulated and the average energy calculated. The space in between grid points was interpolated bilinearly.

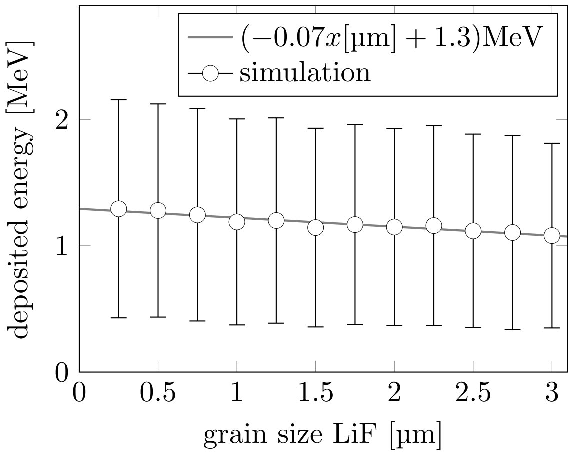

Fig. 7.3: Average amount of energy deposited in ZnS grains for LiF grain sizes smaller than 3 µm and default ZnS grain size of 7.5 µm. The bars indicate the root mean square deviation of the distribution, the error is a factor 45 smaller since each data point represents 2000 simulated events. The linear fit shows that the average deposited energy is decreasing for increasing LiF grain size.

the average deposited energy for small LiF grains at the default ZnS grain size of 7.5 µm. The bars in the figure show the root mean square deviation of the distribution, not the error of the average. Since each data point is backed by 2000 simulated events, the error is smaller than the root mean square by a factor of $\sqrt{1999} \approx 45$.

A linear fit shows a very gentle slope of 0.07 MeV µm^{-1}, which does not continue beyond $s_{\text{LiF}} > 4\,\mu\text{m}$, as Figure 7.2 shows. For LiF of such a grain size, the alpha particle leaves much of its energy inside its origin grain. Thus the probability that it reaches a nearby ZnS grain to deposit energy there diminishes rapidly. Then the main contribution comes from the triton particle, which is not heavily influenced by the size of the LiF grain due to its longer range.

In conclusion, if the grain size of LiF is known to be about 2.5 µm, neglection of this grain size in simulations can result in errors of the order of 10 % to 15 %. For detectors based on a ZnS/LiF scintillator this is usually the case and thus the finite grain size should be taken into account in all simulations.

7.3 Influence of Variance in Grain Radii

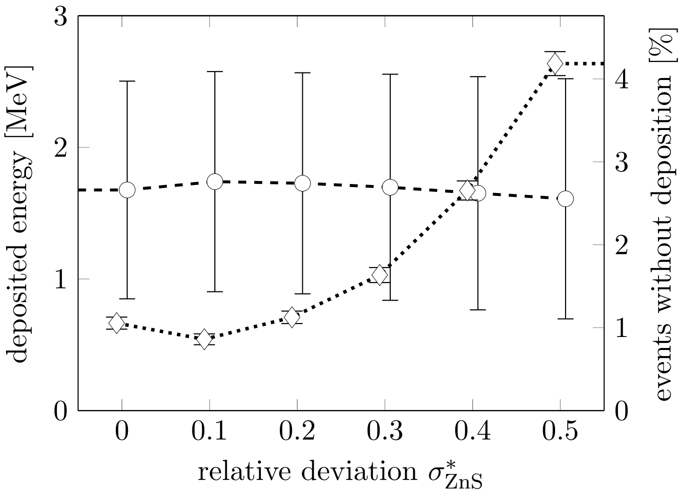

Fig. 7.4: Influence of the relative deviation of ZnS grain size on the amount of energy deposited in ZnS grains in a 4:1 scintillator. The left axis denotes the energy for circles, the right axis denotes the fraction of events in which no energy is deposited in ZnS:Ag for diamonds. Bars for the amount of energy represent the root mean square. With 20 000 events per data point, the error is smaller by a factor of 140. Data points have been slightly offset horizontally in order to increase readability. σ^*_{ZnS} was varied between 0 and 0.5 in steps of 0.1, s_{ZnS} was 10 µm.

Another novelty in our model is the variability of radii of individual grains. The radii are randomly distributed according to a gamma distribution with freely adjustable expectation value and variance (see Section 4.1.1). This enables us to examine the influence of the variance of grain sizes on the energy deposition in ZnS grains.

Figure 7.4 shows the results of simulations where the relative ZnS grain size deviation σ^*_{ZnS} was varied between 0 and 0.5 with a grain size of $s_{\mathrm{ZnS}} = 10\,\mu\mathrm{m}$. The influence on the average amount of energy deposited in ZnS grains does not seem very high. However, the energy changes from the maximum 1.73 MeV at $\sigma^*_{\mathrm{ZnS}} = 0.1$ to 1.61 MeV at $\sigma^*_{\mathrm{ZnS}} = 0.5$, which is a difference of 7 %.

The influence is mainly due to the increased number of events without energy deposition, as the diamonds in the figure show. That number increases from 1 % to more than 4 %. A reason for this effect might be that according to (4.1.7) the expectation value for the volume of a sphere increases with increasing σ^*_{ZnS}, so less spheres are placed in the grain box such that the space between spheres gets larger.

It is peculiar that the maximum energy deposition does not occur at $\sigma^*_{\mathrm{ZnS}} = 0$. It may be worth further investigation in order to verify the non-zero minimum. If it persists, it would mean that a small variance in grain sizes is beneficial to the detection efficiency.

7.4 Scintillation Efficiency of ZnS:Ag

One of the necessary input parameters of the `G4VScintillation` process is not known: the absolute scintillation efficiency C of ZnS:Ag. In the measurements described in Section 5.3 a value for C/γ was obtained, but since the PMT was not calibrated, it is not possible to determine γ and thus C.

Fortunately, measurements which determined the number of emitted photons have been carried out for several scintillator samples in 1969 by Spowart [42]. However, during these measurements single neutron events were not resolved. Instead, the photo current resulting from the neutron flux was measured. Thus, only the average number of photons per neutron event was determined. The results are shown in Table 7.1.

The value for $\langle N_{\text{exit}}\rangle$ given in [42] is directly proportional to the amount $\langle N\rangle$ of photons passing through the photo cathode of the PMT. According to calculations in that report, 45 % of the light exiting the scintillator is bound to the photo cathode, so $\langle N\rangle = 0.45\langle N_{\text{exit}}\rangle$. Using the probability distribution $p_N(N)$ from (A.4.5), the theoretical expectation for $\langle N\rangle$ can be calculated in a similar manner as in Section 5.3:

$$\begin{aligned}
\langle N\rangle &= \int_0^\infty dN\; N\, p_N(N) \\
&= \int_0^d dx\; h(x) \int_0^\infty dN\; \frac{N}{\alpha_l(x)\cdot C}\; p_E\!\left(\frac{N}{\alpha_l(x)\cdot C}\right) \\
&= \int_0^d dx\; h(x) \int_0^\infty dE\; C\alpha_l(x)\cdot E\, p_E(E) \\
&= C\int_0^\infty dE\; E\cdot p_E(E) \int_0^d dx\; h(x)\;\alpha_l(x) \\
&= C\langle E\rangle\langle\alpha_l\rangle_h
\end{aligned} \tag{7.4.1}$$

with $\alpha_l(x)$ and $h(x)$ defined as in (A.4.3) and (A.4.6), and $p_E(E)$ being the distribution of energy deposited in ZnS grains approximated by simulations of the grain box module. In the third step we substituted the integration over N by integration over $E = N/\alpha_l(x)C$, which is the energy deposited in ZnS:Ag. The two integrals factor out and can be performed independently of each other. The last step is a definition of two expectation values $\langle E\rangle$ and $\langle\alpha_l\rangle_h$.

mass ratio ZnS/LiF/binder	scintillator thickness d[µm]	neutron attenuation factor $1 - I/I_0$[%]	number of photons emitted per neutron hit $\langle N_{\mathrm{exit}} \rangle$
2:1:1	730	48	59 000
2:1:1	250	16	157 000
3:1:1	220	15	174 000
6:1:1	210	8	157 000
1:3:1	230	37	47 000
1:6:1	230	41	27 000

Table 7.1: Scintillation efficiency of some samples as reported in [42]. The neutron attenuation coefficient was measured using a manganese foil, and the number of photons emitted were obtained by measuring the photo current of a calibrated PMT mounted behind the scintillators in a defined neutron flux. The light output differs across samples due to differences in mass ratios and thicknesses.

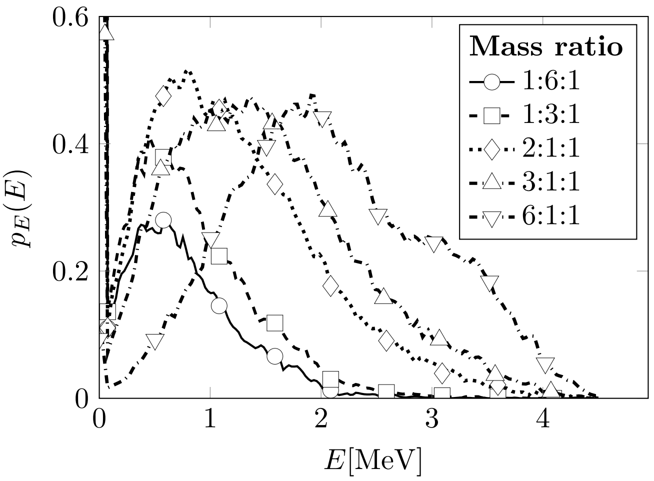

Fig. 7.5: Simulated probability distribution of the amount of energy deposited in ZnS grains after a neutron event for all different mass ratios mentioned in Table 7.1.

$\langle E \rangle$ can be obtained from simulations of the grain box module with the same mass ratios as in Table 7.1. The ZnS grain size is set to 10 µm which is mentioned in [42] to be the optimal grain size. The other parameters are left at the default values shown in Table 4.1.

Even though the neutron attenuation factor is given, we cannot reliably determine the binder density in this case. The formula for the binder density (5.1.4) requires the cross section of a single ^{6}Li nucleus, which depends on the neutron energy. Since a thermal neutron source without monochromator was used in [42] and the energy spectrum of the source is not provided, the average neutron energy is unknown. The assumption of monochromatic thermal neutrons (25 meV) yields binder densities in the range of $0.3\,\mathrm{g\,cm^{-3}}$ to $0.6\,\mathrm{g\,cm^{-3}}$. This value is much lower than that of common binder materials which is why the more conservative default value of $1\,\mathrm{g\,cm^{-3}}$ was chosen. Simulation results are shown in Figure 7.5.

For the calculation of $\langle \alpha_l \rangle_h$ the knowledge of attenuation lengths for neutrons λ_n and

mass ratio ZnS/LiF/binder	scintillator thickness d[µm]	energy deposited in ZnS $\langle E\rangle$[MeV]	photon transmission coefficient $\langle\alpha_l\rangle$	scintillation efficiency at $\lambda_l = 0.41\,\mathrm{mm}$ $C_s[\mathrm{keV}^{-1}]$
2:1:1	730	1.09	0.23	246
2:1:1	250	1.09	0.42	338
3:1:1	220	1.43	0.45	267
6:1:1	210	2.10	0.45	168
1:3:1	230	0.39	0.48	249
1:6:1	230	0.23	0.49	238

Table 7.2: Deposited Energy, photon transmission and scintillation efficiency for the configurations mentioned in Table 7.1. The latter two values were calculated at $\lambda_l = 0.41\,\mathrm{mm}$. This gives a mean scintillation efficiency of $C = 249\,\mathrm{keV}^{-1}$ and a root mean square deviation of $\Delta C = 55\,\mathrm{keV}^{-1}$.

photons λ_l is necessary. The former can be obtained from the attenuation factor $1 - I/I_0$ and the sample's thickness d:

$$I = I_0 e^{-\frac{d}{\lambda_n}} \qquad \Leftrightarrow \qquad \lambda_n = \frac{d}{\ln(I_0/I)} \tag{7.4.2}$$

Under the assumption that all samples have the same optical attenuation length, one can calculate the scintillation efficiency C_s for each sample s and calculate the mean C as well as the root of the mean square deviation ΔC:

$$\begin{aligned} C &= \frac{1}{6}\sum_s C_s \\ \Delta C &= \sqrt{\frac{1}{5}\sum_s (C_s - C)^2} \end{aligned} \tag{7.4.3}$$

Figure 7.6 shows the relative standard deviation $\Delta C/C$ depending on λ_l in the range of 0 mm to 1 mm, which shows a minimum at $\lambda_l = 0.41\,\mathrm{mm}$. This means that this value for the effective photon attenuation length is the best fit for our data. At this optical attenuation length the mean scintillation efficiency becomes $C = 249\,\mathrm{keV}^{-1}$ and the root mean square deviation $\Delta C = 55\,\mathrm{keV}^{-1}$.

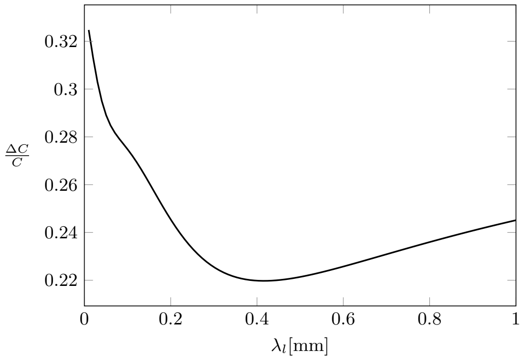

Fig. 7.6: Relative standard deviation of the absolute scintillation efficiency C of ZnS:Ag depending on the effective optical attenuation length λ_l.

This value seems very high, especially when compared to the value of $100\,\mathrm{keV}^{-1}$ for gammas [43], and it is necessary to critically reflect on some of its aspects. One assumption that has been made is, that the effective optical attenuation length is the same for all samples. However, as simulations in Section 5.2.3 suggest, increasing the fraction of ZnS of a scintillator probably leads to a shorter optical attenuation length.

Another point to mention is the inconsistency of neutron attenuation length in Spowart's measurements for samples of equal mass ratios but different thicknesses. Using (7.4.2), the attenuation lengths of the 2:1:1 samples in table 7.1 are 1.1 mm and 1.4 mm respectively. Such a discrepancy of about 30 % also shows up for the values of the scintillation efficiency C_s, as can be seen in table 7.2. So the relatively large variation in C_s may in fact originate from these inconsistencies.

Further, since the photodetector was operated in current mode during the measurements, single events could not be resolved. That is why only information about the mean value and no information about the distribution of the number of photons per neutron event were obtained.

However, our result is a first estimate of the scintillation efficiency of ZnS:Ag. In conjunction with the effective optical attenuation length, it is suitable for simulations of photons in a detector system using a ZnS/LiF scintillator.

A new measurement including a larger variety of sample configurations with well known binder density, a monochromatic neutron source, and event based data collection could address all problems discussed and combined with further simulations yield a much more precise value for the scintillation efficiency of ZnS:Ag.

Chapter 8

Conclusion and Outlook

This work addressed the numerical simulation of a ZnS/LiF scintillation neutron detector with WLSF readout. A model of the physical front end of this detector system was developed and compared to experimental results and earlier models regarding such a detector. The model was implemented in Geant4 and includes the description of the scintillator's microscopic grain structure and the propagation of photons in scintillator plate and WLSFs.

Contrary to earlier models, the LiF grain size was included in this model in form of a region around the starting point of alpha and triton particles, where placing ZnS grains is not possible. It was shown that the variation of LiF grain sizes between 0 µm and 3 µm leads to energy depositions in ZnS differing by 10 % to 15 %. This means that addressing the LiF grain size in the model gives an advantage over models which treat the LiF/binder surrounding as homogeneous.

Another enhancement of earlier models was allowing individual, random grain sizes. Simulations with different variances of grain radii revealed that this parameter excerts an influence on the average energy deposition of about 7 %. This is mainly due to an increased average grain volume and consequently a reduction of the number of spheres, which results in larger spaces in between the grains and leads to slightly more events without energy deposition in ZnS:Ag.

Different parts of the model were validated independently against real measurements. Measurements of neutron attenuation in several scintillator samples with different compositions and thicknesses were in good agreement with simulated values and showed an average deviation of about 5 %. They also provided estimations for the binder densities of scintillator samples of the manufacturers ELJ and AST.

The propagation of photons inside the scintillator plate was modelled by random virtual grain boundaries, at which optical processes occur, or interchangeably by an exponential attenuation law governed by an effective attenuation length. Simulations using the random walk model indicate that the optical absorption of the scintillator plate depends on the refractive index of the binder material and has a minimum when refractive indices of binder and LiF are equal. In this case photons do not scatter at the very small LiF grains and have straighter paths, which leads to a longer effective attenuation length for photons, thus increasing the light yield of the scintillator.

Optical transmission measurements revealed that surface effects play an important role for the photon propagation. Currently neither the random walk model nor the effective model capture this effect. Further measurements of the scintillator's reflectance might reveal to what extent surface effects contribute to the attenuation of scintillator light.

The effective model reproduces the attenuation length for photons in the scintillator up to a geometric effect. Simulations using the random walk model produce attenuation lengths which roughly match the ELJ measurements with a deviation of 17 %, but are too small to fit AST data. Results for varying the ZnS mass ratio indicate that the attenuation length in fact depends on microscopic parameters and thus the results from the measurements are not necessarily generalizable. An improvement of the random walk process might be to override the default exponential step length distribution of Geant with some finite distribution.

The validity of the grain box model could be shown by comparing neutron pulse height statistics between measurements and simulations. Since the pulse height of an event does not only depend on the amount of energy deposited in ZnS, but also on the attenuation of light in the scintillator, the simulated distribution of deposited energy had to be convoluted with the fraction of light exiting the scintillator after an event at a certain depth. This analytically calculated function depends on the effective optical attenuation length and the proportionality constant between ADC channel number and energy as fit parameters. The latter value, which should be equal for all measurements, shows a deviation of 20 % in the fit of one sample. The attenuation length varies by a factor of 2 between measurements, which is more than simulations of the random walk model indicates, but its absolute value is of the same order of magnitude as the values obtained in the light transmission measurements. However, although the fit values show these discrepancies, the form of the pulse height spectra could be reproduced very well and have better χ^2 test values than an exponential fit.

For the comparison of the full detector system including the WLSFs a position reconstruction algorithm for offline data based on cluster analysis was developed. In order to form a cluster, Photons must be from the same WLSF layer and cannot have their timestamps differ by more than the maximum allowed time difference τ and their channels by more than the maximum channel difference n_c. Two clusters from different layers can form a neutron event, if they have enough photons and if the difference in starting time does not exceed the coincidence time t_c. The reconstruction algorithm was applied to data from measurements with a prototype detector for SAPHiR, where neutron events could clearly be distinguished from events probably caused by gamma radiation in fiber bundles.

The algorithm is easily adaptable for online analysis of photon event data. In order to increase the detection efficiency there is the potential for optimization of algorithm parameters like τ, n_c and t_c. If very high counting rates are expected, the cluster finding algorithm needs to be improved by introducing a maximum cluster length, or by splitting up clusters when the amount of photons per time suddenly increases.

The application of the reconstruction algorithm to simulation results of the full detector system showed a distribution of cluster sizes and durations similar to those obtained in the measurement.The previously unknown attenuation length of the outermost WLSF cladding could be estimated by comparing the ratio of the number of photons in the first WLSF layer in measurement and simulation. A value of 0.01 mm shows a good agreement of the peak ratio of 80 % and explains a light loss factor of 78 %. With the photo cathodes' quantum efficiency of 25 %, this results in a total efficiency of 5.5 %. However, the best agreement between simulation and measurement is reached for an efficiency factor of less than 0.05. This means, that there are still some photon losses unaccounted for, which might be explained by surface effects in the scintillator or by a wrong estimation of the scintillation efficiency. Determining these factors requires additional measurements.

Furthermore, an algorithm able to optmize multiple parameters of the model simultaneously has been developed. As a proof of concept, the scintillator thickness d and ZnS mass ratio ϕ_{ZnS} were optimized using an estimation of detector efficiency as optimization function. Since the chosen function depends on an arbitrary assumption of detection efficiency of the WLSF readout, the result $d = 0.574(9)\,\mathrm{mm}$, $\phi_{\mathrm{ZnS}} = 3.83(9)$ is not yet a recommendation for the detector design.

The challenge of very long simulation times was met by choosing the GSS algortithm for optimization, which requires only few function evaluations. How much simulation data is required is determined by a function evaluation algorithm, which stops the simulation as soon as it detects that further data only marginally influences the function value.

The scintillation efficiency of ZnS:Ag used in the full simulation was obtained by comparison to a measurement of the average number of photons per event exiting different sample scintillators. A value of $C = 249(55)\,\mathrm{keV}^{-1}$ was found, which is very high compared to the gamma response of $100\,\mathrm{keV}^{-1}$ of ZnS:Ag given in the literature. The large uncertainty might be caused by poor consistency of the neutron absorbtion rates presented in the measurement. The neutron attenuation lengths of samples with the same ZnS/LiF/binder composition should be equal, but the measurements show a difference of more than 30 % in two samples differing only in thickness. In order to improve the reliability on our value for C, additional measurements are needed, which resolve the distribution of the number of photons of single events.

Based on this work it will be possible to support the analysis of measurement data of ZnS/LiF detectors with WLSF readout. By simulating detector systems of this kind, the response to neutrons of different wavelengths can be estimated and used to correct counting rates in the analysis. Also the dependence on the neutron's position can be examined, which is of special interest for detectors with loosely spaced WLSFs. However, neutrons at the edge of the scintillator plate of any detector system might cause a different channel-distribution of photons than neutrons at the detector's center.

The model will also help new developments of scintillation detectors by optimizing parameters of the model and of the reconstruction algorithm with regard to the application's needs. And, due to the modular structure of the model, it can easily be extended to incorporate future designs.

Appendices

Appendix A

Calculations

A.1 Minimum Path Ratio in Outermost Fiber Cladding

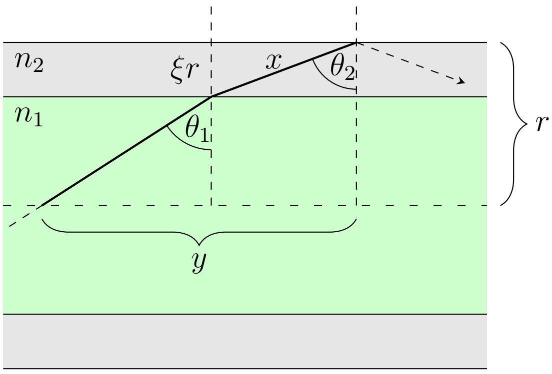

Fig. A.1: Undesired photon being reflected at the outermost fiber boundary

In order to calculate the path length traversed inside the outermost cladding of a fiber, it is sufficient to consider a half period of the path. A period in this context means the time between two internal reflections at the fiber boundary. Figure A.1 shows a half period of an undesired photon for a single cladded fiber. We are interested in the travel distance x inside the outer cladding with respect to the total fiber length y traversed. Simple geometric consideration gives

$$x = \frac{\xi r}{\cos\theta_2} = \frac{\xi r}{\sqrt{1-\left(\frac{n_1}{n_2}\sin(\theta_1)\right)^2}},$$
$$y = (1-\xi) r\tan\theta_1 + \xi r\tan\theta_2 = r\sin\theta_1\left(\frac{1-\xi}{\sqrt{1-\sin^2\theta_1}} + \frac{\frac{n_1}{n_2}\xi}{\sqrt{1-\left(\frac{n_1}{n_2}\sin\theta_1\right)^2}}\right), \tag{A.1.1}$$

where we used Snell's law and the trigonometric relation $\cos(\arcsin x) = \sqrt{1-x^2}$.

Then the quotient is simply

$$\eta := \frac{x}{y} = \frac{(\sin\theta_1)^{-1}}{\frac{n_1}{n_2} + \frac{1-\xi}{\xi}\sqrt{\frac{1-\left(\frac{n_1}{n_2}\sin\theta_1\right)^2}{1-\sin^2\theta_1}}}. \tag{A.1.2}$$

The minimum of η is easier calculated numerically than analytically. A plot of this function can be seen in Figure A.2. The minimal path ratio clearly depends on the refractive indices. In our case, the core has a refractive index of $n_1 = 1.59$ and the outermost cladding has a refractive index of $n_2 = 1.49$ or $n_2 = 1.42$. The minimum value for $n_2 = 1.49$ is

$$\eta_{\min} \approx 0.0429. \tag{A.1.3}$$

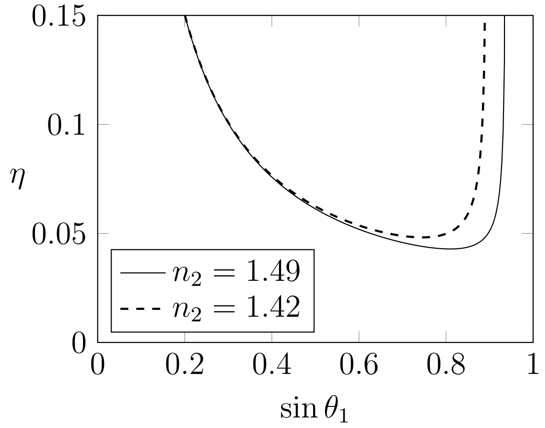

Fig. A.2: Distance travelled in outer cladding per fiber length as calculated in (A.1.2) for $n_1 = 1.59$ and $\xi = 0.03$. For n_2 the two possible refractive indices of outer cladding, PMMA and FP have been chosen.

Thus, if we assume the length of fiber leading back to the PMTs being 30 cm, there will be photons which travel through the outermost cladding for a total length of only 1.29 cm.

Helical paths do not need to be considered here, because a helical path would have an increased x, while y stays the same. Thus, $\eta_{\min}$ is the lower bound for the path ratio.

A.2 Volume and Mass Fractions in Heterogeneous Materials

In a heterogeneous mixture of several materials, let V_X, M_X, ϕ_X and ρ_X denote the total volume, total mass, mass ratio and density of material X. In the case of a ZnS/LiF scintillator, the different materials would be ZnS, LiF and the binder material. With the definition of the mass ratios $\left(M_X = \frac{\phi_X}{\sum \phi_Y} \cdot M\right)$ we can express the volume as

$$V_X = \frac{M_X}{\rho_X} = \frac{\frac{\phi_X}{\rho_X}}{\sum \phi_Y} \cdot M. \tag{A.2.1}$$

The total density is then

$$\rho = \frac{M}{V} = \frac{M}{\sum V_X} = \frac{\sum \phi_X}{\sum \frac{\phi_X}{\rho_X}}, \tag{A.2.2}$$

so that the volume fraction of each material is

$$\frac{V_X}{V} = \frac{\rho \cdot V_X}{M} = \frac{\frac{\phi_X}{\rho_X}}{\sum \frac{\phi_Y}{\rho_Y}}. \tag{A.2.3}$$

The mass ratios ϕ_X are usually provided by the manufacturer of a scintillator plate. At room tempertature the density of ZnS:Ag is $\rho_{\mathrm{ZnS}} = 4.09\,\mathrm{g\,cm^{-3}}$, that of unaltered LiF $2.635\,\mathrm{g\,cm^{-3}}$. If the LiF is enriched in ^{6}Li, the density is lowered due to the missing neutron. The molecular mass of natural LiF is 25.94 [44], so the molecular mass of enriched LiF is 24.94. This leads to a density of enriched LiF of $\rho_{\mathrm{LiF}} = 24.94/25.94 \cdot 2.635\,\mathrm{g\,cm^{-3}} = 2.533\,\mathrm{g\,cm^{-3}}$. Different manufacturers use different binder materials, which may result in different binder densities. This quantity is usually not mentioned in the scintillator specifications, so it has to be determined experimentally.

A.3 Rotation of Basis Vector to Arbitrary Vector

Let $\hat{n}$ be an arbitrary vector in $\mathbb{R}^3$ with Cartesian coordinates $(n_1, n_2, n_3)^T$ and length $\sqrt{\sum n_i^2} = 1$. We seek a matrix $A^c(\hat{n})$, $c \in \{x, y, z\}$, which maps the basis vector $\hat{e}_c$ to $\vec{n}$. Without loss of generality we choose $c = z$ and drop this index, since it is trivial to obtain solutions for the other axes by rotation of matrix columns.

To keep lengths and angles unchanged, the columns of A need to form an orthogonal system of basis vectors:

$$\sum_i A_{il} \cdot A_{ik} = \begin{cases} 1, & \text{if } l = k \\ 0 & \text{otherwise} \end{cases} \tag{A.3.1}$$

Three of the coefficients are easily determined by $A \cdot \hat{e}_z = \hat{n}$:

$$A_{i3} = n_i, \text{ for } i \in \{1, 2, 3\} \tag{A.3.2}$$

For the remaining 6 entries there are 5 independent equations of the form (A.3.1). This means we are free to choose one of the entries and arbitrarily choose $A_{13} = 0$. Now we name the coefficents of A:

$$A = \begin{pmatrix} a & c & n_1 \\ b & d & n_2 \\ 0 & f & n_3 \end{pmatrix} \tag{A.3.3}$$

From $a^2 + b^2 = 1$ and $a \cdot n_1 + b \cdot n_2 = 0$ follows

$$\begin{aligned} a &= \textcircled{$\pm$}\frac{n_2}{\sqrt{n_1^2 + n_2^2}} = \textcircled{$\pm$}\frac{n_2}{\sqrt{1 - n_3^2}}, \\ b &= \textcircled{$\mp$}\frac{n_1}{\sqrt{n_1^2 + n_2^2}} = \textcircled{$\mp$}\frac{n_1}{\sqrt{1 - n_3^2}}, \end{aligned} \tag{A.3.4}$$

where the circles around the plus/minus sign indicate that those two unary operators depend on each other. This notation is necessary, because there will be further choices for quadratic equations later on and it is necessary to keep track which ± signs are connected to each other.

$ac + bd = 0$ simplifies to $cn_2 - dn_1 = 0$ which can be plugged into $cn_1 + dn_2 + fn_3 = 0$ and $c^2 + d^2 + f^2 = 1$:

$$\begin{aligned} (n_1^2 + n_2^2)\frac{c}{n_1} + fn_3 &= 0 \\ (n_1^2 + n_2^2)\frac{c^2}{n_1^2} + f^2 &= 1 \\ \Rightarrow \qquad f &= \boxed{\pm}\sqrt{1 - n_3^2} \\ \Rightarrow \qquad c &= \boxed{\mp}\frac{n_1 n_3}{\sqrt{1 - n_3^2}} \\ \Rightarrow \qquad d &= \boxed{\mp}\frac{n_2 n_3}{\sqrt{1 - n_3^2}} \end{aligned} \tag{A.3.5}$$

It remains to make the two choices regarding the ± signs. We want a pure rotation, which means we want the determinant of A to be positive. A simple calculation shows that $\det A = \big(\textcircled{$\pm$}1\big) \cdot (\boxed{\mp}1) \overset{!}{=} 1$, which means that if we choose plus (the upper choice) from $\textcircled{$\pm$}$, we also need to choose plus (the lower choice) from $\boxed{\mp}$. The matrix then is

$$A^z(\hat{n}) = \frac{1}{\sqrt{1 - n_3^2}} \begin{pmatrix} n_2 & n_1 n_3 & n_1\sqrt{1 - n_3^2} \\ -n_1 & n_2 n_3 & n_2\sqrt{1 - n_3^2} \\ 0 & -(1 - n_3^2) & n_3\sqrt{1 - n_3^2} \end{pmatrix}. \tag{A.3.6}$$

A.4 Expectation of Light Intensity After a Neutron Event

If a certain amount of energy is deposited in ZnS grains after a neutron event, it will cause a flash of scintillation light with brightness proportional to the energy. So, the number of created photons due to scintillation can be estimated by an equation like

$$N_{\text{scint}} = C \cdot E_{\text{dep}}, \tag{A.4.1}$$

where C is the absolute scintillation efficiency of ZnS:Ag. How many of these photons reach the surface and are then detectable depends on the depth of the event because of self absorption inside the scintillator plate. So the cause for a flash of certain brightness could be either an event close to the surface, where little energy is deposited in ZnS grains (i.e. few photons are created in the first place), or an event further inside, where more energy is deposited. So the distribution of energy deposited in ZnS grains is not necessarily of the same shape as the pulse height spectrum observed outside the scintillator.

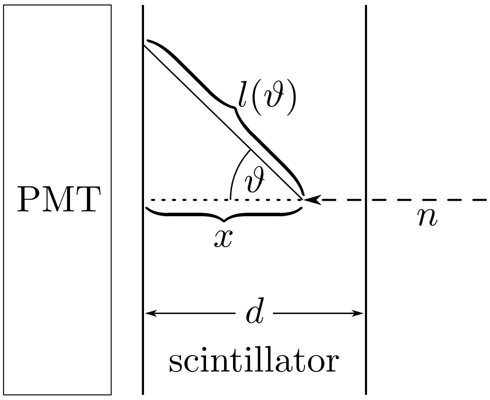

Fig. A.3: Schema of the calculation: A leftbound neutron is captured at distance x to the PMT-boundary. The light ray emitted at angle ϑ is exponentially attenuated along the distance of $l(\vartheta) = \frac{x}{\cos(\vartheta)}$.

Photons will take random paths through the material in general, but we can model their propagation as straight paths with exponential attenuation (see Section 4.2.1). Assuming a schema as depicted in Figure A.3 one can calculate the fraction $\alpha_l(x)$ of light, which reaches the surface on the PMT-side after a neutron event at depth x. For a given angle θ the light reaching the surface after exponential attenuation along $l(\theta)$ is $\exp\left(-l(\theta)/\lambda_l\right)$, where λ_l is the effective attenuation length for light. $\alpha_l(x)$ is obtained by integration over the half solid angle:

$$\alpha_l(x) = \frac{1}{4\pi} \int\limits_0^{2\pi} d\varphi \int\limits_0^{\frac{\pi}{2}} d\vartheta \; \sin(\vartheta) \cdot \exp\left(-\frac{l(\vartheta)}{\lambda_l}\right) \tag{A.4.2}$$

Using $l(\theta) = x/\cos(\theta)$ and the substitution $y = x/\lambda_l \cos(\theta)$, the integral can be simplified:

$$\begin{aligned}\alpha_l(x) &= \frac{1}{2}\int\limits_{\frac{x}{\lambda_l}}^{\infty} dy\ \frac{x}{\lambda_l} y^{-2} e^{-y} \\ &= \frac{1}{2}\left(e^{-\frac{x}{\lambda_l}} - \frac{x}{\lambda_l}\int\limits_{\frac{x}{\lambda_l}}^{\infty} dy\ \frac{e^{-y}}{y}\right),\end{aligned} \tag{A.4.3}$$

where in the last step we employed integration by parts. $e^{-\frac{x}{\lambda_l}}$ is the usual exponential attenuation and the remaining part is a geometric correction term. There is no analytical expression for the integral, but it can be approximated via numerical methods. The number of photons exiting the scintillator plate on the PMT-side is then

$$N_{\text{exit}} = \alpha_l(x) \cdot C \cdot E_{\text{dep}}. \tag{A.4.4}$$

There are two statistical processes. The first determines the probability $h(x)dx$ of an event happening at depth x and the second determines the probability $p_E(E)$ that the energy E is deposited in ZnS grains. To find the distribution of the number of exiting photons, one needs to integrate probability contributions over the whole depth of the scintillator. (A.4.4) must be fulfilled for $p_E(E)$ and $h(x)$ to contribute to the distribution of exiting light $p_N(N)$, so the weight function must be a Dirac-delta function:

$$\begin{aligned}p_N(N)dN &= \left(\int\limits_0^d dx\ h(x) \int\limits_0^{E_{\max}} dE\ p_E(E) \cdot \delta\left(N - \alpha_l(x) \cdot C \cdot E\right)\right) dN \\ &= \left(\int\limits_0^d dx\ \frac{h(x)}{\alpha_l(x) \cdot C} \cdot p_E\left(\frac{N}{\alpha_l(x) \cdot C}\right)\right) dN\end{aligned} \tag{A.4.5}$$

We performed the integral over the energy because E occurs linearly in the delta function, whereas x is included as a parameter to the not easily invertible function α_l. Therefore it would require some numerical effort to find the root with respect to x. Since $p_N(N)$ describes the probability distribution for N photons exiting the scintillator and scintillation photons have a similar wavelength, it is also a measure for the light intensity spectrum.

It remains to determine the probability distributions $h(x)$ and $p_E(E)$. The latter can be obtained by simulations of the grain box module described in Section 4.1 and the former is calculated as follows. In Figure A.3 the neutron beam enters the scintillator plate from the right at $x = d$. From there on the beam undergoes exponential attenuation and its intensity reduces to $\exp(-d/\lambda_n)$ on the left, where λ_n is the neutron attenuation length. Since the amount of events happening in a certain depth is proportional to the beam intensity at that point, $h(x)$ must be proportional to $\exp(-(d-x)/\lambda_n)$. The proportionality factor follows from normalization:

$$h(x) = \frac{1}{\lambda_n} \frac{e^{-\frac{d-x}{\lambda_n}}}{1 - e^{-\frac{d}{\lambda_n}}} \tag{A.4.6}$$

Bibliography

[1] Dana A. Shea and Daniel Morgan. The helium-3 shortage: Supply, demand, and options for congress. Congressional Research Service, 2010. R41419.

[2] Adrian Cho. Helium-3 Shortage Could Put Freeze On Low-Temperature Research. Science, 326(5954):778–779, November 2009.

[3] R.H. Bossi and A.H. Robinson. Monte carlo computer model to optimize light yield from lif–zns scintillators. Trans. Am. Nucl. Soc., 22:153, Nov 1975.

[4] Andrew C. Stephan, Sheng Dai, Steven A. Wallace, and Laurence F. Miller. Modelling of composite neutron scintillators. Radiation Protection Dosimetry, 116(1-4):165–169, 2005.

[5] Y. Yehuda-Zada et al. Monte carlo simulation for optimizing 6lif:zns(ag) based neutron detector configuration. Conference of the Nuclear Societies in Israel, Feb 2014.

[6] Chong Wu, Bin Tang, ZhiJia Sun, Qiang Zhang, Zhen Yang, Wei Luo, and Tuo Wang. The monte-carlo simulation on a scintillator neutron detector. Science China Physics, Mechanics and Astronomy, 56(10):1892–1896, 2013.

[7] S. Agostinelli et al. GEANT4: A Simulation toolkit. Nuclear Instruments and Methods, 506:250–303, 2003.

[8] N. J. Carron. An Introduction to the Passage of Energetic Particles through Matter. Taylor & Francis, Boca Raton, 2007.

[9] Glenn Knoll. Radiation detection and measurement. Wiley, New York, 2000.

[10] R. Allemand, J. Bourdel, E. Roudaut, P. Convert, K. Ibel, J. Jacobe, J. P. Cotton, and B. Farnoux. Position-sensitive detectors (p.s.d.) for neutron diffraction. Nuclear Instruments and Methods, 126(1):29–42, May 1975.

[11] Jeffrey L. Lacy, Athanasios Athanasiades, Liang Sun, Christopher S. Martin, Tom D. Lyons, Michael A. Foss, and Hal B. Haygood. Boron-coated straws as a replacement for 3he-based neutron detectors. Nuclear Instruments and Methods in Physics Research Section A: Accelerators, Spectrometers, Detectors and Associated Equipment, 652(1):359 – 363, 2011. Symposium on Radiation Measurements and Applications (SORMA) {XII} 2010.

[12] C.W.E van Eijk, A Bessière, and P Dorenbos. Inorganic thermal-neutron scintillators. Nuclear Instruments and Methods in Physics Research Section A: Accelerators, Spectrometers, Detectors and Associated Equipment, 529(1–3):260 – 267, 2004. Proceedings of the Joint Meeting of the International Conference on Neutron Optics (NOP2004) and the Third International Workshop on Position-Sensitive Neutron Detectors (PSND2004).

[13] John P. Walter and Marvin L. Cohen. Calculation of the reflectivity, modulated reflectivity, and band structure of gaas, gap, znse, and zns. Phys. Rev., 183(3):763–772, Jul 1969.

[14] H. H. Li. Refractive index of alkali halides and its wavelength and temperature derivatives. Journal of Physical and Chemical Reference Data, 5(2):329–528, 1976.

[15] Claude A. Klein. Room-temperature dispersion equations for cubic zinc sulfide. Appl. Opt., 25(12):1873–1875, Jun 1986.

[16] McKnight. An improved flexible neutron detector for powder diffraction experiments. Master's thesis, Brigham Young University, USA, 2005.

[17] KURARAY CO. Plastic scintillating fibers (materials and structures). `http://kuraraypsf.jp/psf/index.html`. Accessed: 2016-02-10.

[18] John W. Hicks. Doubly clad light-conducting fibers with the outer cladding being partially light absorbing, May 31 1966. US Patent 3,253,500.

[19] Carel W.E. van Eijk. Inorganic-scintillator development. Nuclear Instruments and Methods in Physics Research Section A: Accelerators, Spectrometers, Detectors and Associated Equipment, 460(1):1 – 14, 2001. Proc. 1st Int. Workshop on Radiation Imaging Detectors.

[20] Luc Devroye. Non-uniform random variate generation. Springer-Verlag, New York, 1986.

[21] B. Widom. Random sequential addition of hard spheres to a volume. The Journal of Chemical Physics, 44(10):3888–3894, 1966.

[22] E. Hecht. Optics. Addison-Wesley, 2002.

[23] Gustav Mie. Beiträge zur optik trüber medien, speziell kolloidaler metallösungen. Annalen der Physik, 330(3):377–445, 1908.

[24] L. G. Henyey and J. L. Greenstein. Diffuse radiation in the Galaxy. Astrophysical Journal, 93:70–83, January 1941.

[25] KURARAY CO. Wavelength shifting fibers. `http://kuraraypsf.jp/psf/ws.html`. Accessed: 2016-02-10.

[26] O. Mineev, Yu Kudenko, Yu Musienko, I. Polyansky, and N Yershov. Scintillator detectors with long wls fibers and multi-pixel photodiodes. Journal of Instrumentation, 6(12):P12004, 2011.

[27] E. Bartosz, B. Bertoldi, D. Davis, V. Hagopian, K. Hu, C. Immer, K. F. Johnson, J. Thomaston, and H. Whitaker. Decay Times of Wavelength Shifting Fibers and Scintillator Plates. 1992. SDC-93-421.

[28] KURARAY CO. Clear fibers. `http://kuraraypsf.jp/psf/cf.html`. Accessed: 2016-02-10.

[29] Ralf Engels and Günter Kemmerling. Abschlussbericht – POWTEX WLSF-Detektortyp. ZEA-2 Forschungszentrum Jülich Germany, internal report, March 2013.

[30] G. Audi, Kondev F.G., M. Wang, B. Pfeiffer, X. Sun, J. Blachot, and M. MacCormick. The nubase2012 evaluation of nuclear properties. Chinese Physics C, 36(12):1157–1286, 2012.

[31] Ian Mills. Quantities, units, and symbols in physical chemistry. Blackwell Scientific Publications CRC Press distributor, Oxford Boston Boca Raton, Fla, 1993.

[32] T. Tojo and T. Nakajima. Preparation of thermal neutron scintillators based on a mixture of ZnS(Ag), ^{6}LiF and polyethylene. Nuclear Instruments and Methods, 53:163–166, July 1967.

[33] R Stedman. Scintillator for thermal neutrons using li^{6}f and zns(ag). Rev. Sci. Instr., 31, 1960.

[34] D. P. Hutchinson, V. C. Miller, and J. A. Ramsey. Neutron scintillators using wavelength shifting fibers. Journal of Neutron Research, 4(1-4):123–127, 1996.

[35] F. Caridi, L. Torrisi, and A.M. Visco. Light transmission through polyethylene samples. Optics Communications, 285(6):1199 – 1205, 2012.

[36] M Bodmer, N Phan, M Gold, D Loomba, J A J Matthews, and K Rielage. Measurement of optical attenuation in acrylic light guides for a dark matter detector. Journal of Instrumentation, 9(02):P02002, 2014.

[37] Y. Uehara. Electronic structure of luminescence center of ZnS:Ag phosphors. The Journal of Chemical Physics, 62(8):2982–2994, 1975.

[38] Ralf Engels and Jakob Schelten. Kritische Untersuchungen von Li-Glas und LiF-ZnS Neutronenszintillatoren. ZEA-2 Forschungszentrum Jülich Germany, internal report, November 2010.

[39] Franz Rothlauf. Representations for genetic and evolutionary algorithms. Springer, Heidelberg, 2006.

[40] S. Kirkpatrick, C. D. Gelatt, and M. P. Vecchi. Optimization by simulated annealing. Science, 220(4598):671–680, 1983.

[41] Y.C. Chang. N-dimension golden section search: Its variants and limitations. In Proceedings of the 2009 2nd International Conference on Biomedical Engineering and Informatics, pages 1–6, 2009. DOI:10.1109/BMEI.2009.5304779.

[42] A.R. Spowart. Measurement of the absolute scintillation efficiency of granular and glass neutron scintillators. Nuclear Instruments and Methods, 75(1):35 – 42, 1969.

[43] Radiation effects in solids proceedings of the NATO advanced study institute on radiation, effects in solids, held in Erice, Sicily, Italy, 17-29 July 2004. Springer, Dordrecht, 2006.

[44] Ullmann's encyclopedia of industrial chemistry. Wiley-VCH, Weinheim, Germany, 2003.

Acknowledgements

The work described in this thesis was conducted at the ZEA-2 of the Forschungszentrum Jülich GmbH (FZJ) and financially supported by the post-graduate scholarship programme of the FZJ. Several people have aided in the completion of the work and deserve special thanks:

- Dr. Günter Kemmerling, a great advisor who not only supported me with research ideas but also in rehearsals for conference talks and proofreadings.
- Professor Dr. Thomas Brückel, my supervisor who guided me along the way, helped with administrative tasks and reviewed the thesis in the end.
- Professor Dr. Achim Stahl, my secondary supervisor with whom I had insightful discussions about neutron detectors and who authored the secondary review.
- Professor Dr. Uwe Klemradt and Professor Dr. David Di Vincenzo, the head and fourth member of my examination committee, respectively.
- Dr. Michael Schiek and Ulrich Herzkamp, who helped proofreading the thesis.
- Dr. Ralf Engels and Christian Wesolek, who rendered valuable help in setting up and performing the light attenuation measurements.
- Professor Dr. Stefan van Waasen and my coworkers at the ZEA-2, who supported and encouraged my work in numerous ways.
- All doctoral researchers of the Jülich Centre for Neutron Science and ZEA-2, with whom I had interesting and long discussions about the topic during respective seminars.
- My family and friends, who cheered me up when I needed it.